

Direct Imaging and Spectroscopy of Extrasolar Planets

Thayne Currie

Subaru Telescope, National Astronomical Observatory of Japan, 650 North A‘ohōkū Place, Hilo, HI 96720, USA
Department of Physics and Astronomy, University of Texas-San Antonio, One UTSA Circle, San Antonio, TX, USA

Beth Biller

SUPA, Institute for Astronomy, University of Edinburgh, Blackford Hill, Edinburgh EH9 3HJ, UK

Anne-Marie Lagrange

LESIA, Observatoire de Paris, Université PSL, CNRS, Sorbonne Université, Université Paris Cité, 5 place Jules Janssen, 92195 Meudon, France

Christian Marois

National Research Council of Canada, Herzberg Astronomy & Astrophysics, Victoria, BC, Canada

Olivier Guyon

Subaru Telescope, National Astronomical Observatory of Japan, 650 North A‘ohōkū Place, Hilo, HI 96720, USA

Eric L. Nielsen

Department of Astronomy, New Mexico State University, Las Cruces, NM, USA

Mickael Bonnefoy

IPAG, Univ. Grenoble Alpes, CNRS, IPAG, 38000, Grenoble, France

Robert J. De Rosa

European Southern Observatory, Alonso de Córdova 3107, Vitacura, Santiago, Chile

Abstract– Direct imaging and spectroscopy is the likely means by which we will someday identify, confirm, and characterize an Earth-like planet around a nearby Sun-like star. This Chapter summarizes the current state of knowledge regarding discovering and characterizing exoplanets by direct imaging and spectroscopy. We detail instruments and software needed for direct imaging detections and summarize the current inventory of confirmed and candidate directly-imaged exoplanets. Direct imaging and spectroscopy in the past decade has provided key insights into jovian planet atmospheres, probed the demographics of the outskirts of planetary systems, and shed light on gas giant planet formation. We forecast the new tools and future facilities on the ground and in space that will enhance our capabilities for exoplanet imaging and will likely image habitable zone rocky planets around the nearest stars.

1. Introduction

Identifying, confirming, and characterizing an Earth-like planet around a nearby Sun-like star is a key goal of exoplanet science. In the coming decades, direct imaging and spectroscopy are the likely means by which this goal will be achieved.

Over 5000 extrasolar planets and candidates have been detected through indirect means. In contrast, 20–25 exoplanets have been directly imaged (e.g. [Marois et al. 2008b](#); [Lagrange et al. 2010](#), see Fig. 1). Despite this relatively low yield of discoveries, direct imaging comprises a large fraction of the known exoplanet population amenable to atmo-

spheric characterization, since the method provides photons from the planets themselves instead of just inferring their presence (e.g. [Currie et al. 2011](#); [Konopacky et al. 2013](#)).

Almost all of the directly imaged planets known thus far are young, self-luminous gas giants detected in thermal emission. They represent the extremes of planet formation ([Nielsen et al. 2019](#); [Vigan et al. 2021](#)): planets with masses of $2 M_J$ or more orbiting at moderate to wide separations (~ 10 – 250 au). A subset of directly detected planets appear to be in or just finished with the final stages of assembly (“protoplanets”) ([Keppler et al. 2018](#)). The direct imaging field currently also provides key insights into jovian planet formation and the demographics of the outskirts of plane-

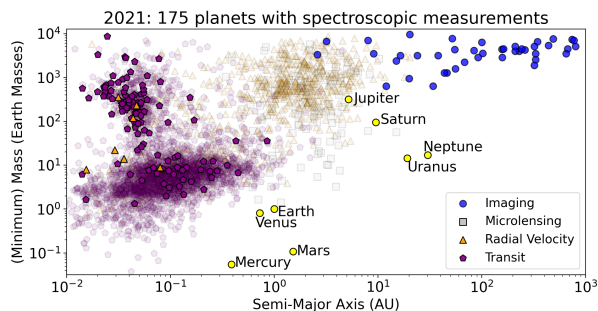


Fig. 1.— Demographics of planetary-mass companions detected with various methods. Bold symbols denote the 175 companions with spectroscopic measurements constraining planet atmospheres: directly imaged companions comprise a substantial fraction of this population. Figure courtesy of Dmitry Savransky, using data from the NASA Exoplanet Archive.

tary systems.

Remarkably, the direct imaging method enables the acquisition of hundreds to thousands of spectroscopic data points on exoplanets in a few hours of telescope time. This wealth of information can critically constrain individual planet atmospheric properties – e.g. temperature, clouds, chemistry, and gravity – as well as the atmospheric evolution of gas giants as a population.

The first direct images and spectra of planet candidates relied on facility, general-use adaptive optics (AO) systems to deblur starlight or space telescopes (i.e. the *Hubble Space Telescope*) coupled with simple coronagraphs (e.g. [Chauvin et al. 2004](#); [Kalas et al. 2008](#)). The past decade has seen the development, demonstration, and honing of dedicated extreme AO systems coupled with advanced coronagraphs and sophisticated post-processing methods, allowing the detection of planets that are fainter and less massive and/or located at smaller angular separations that probe tighter orbits (e.g. [Macintosh et al. 2014](#); [Soummer et al. 2012](#); [Mawet et al. 2012](#)). In-development extreme AO systems and upgrades to first-generation extreme AO systems will provide images of many exoplanets near the ice line ([Guyon et al. 2020](#); [Males et al. 2020](#)). The Coronagraphic Instrument on NASA’s *Roman Space Telescope* (Roman-CGI) could provide the first detections of mature planets in reflected light ([Spergel et al. 2013](#)) (Figure 2).

Planned ground-based extremely large telescopes and proposed space missions promise to make the discovery and confirmation of a habitable, Earth-like exoplanet around a Sun-like star a reality within the next 25 years (e.g. [Lopez-Morales et al. 2019](#); [Gaudi et al. 2020](#); [The LUVUOIR Team 2019](#); [Quanz et al. 2021](#)). These facilities will endeavor to reveal biomarkers – e.g. water, oxygen, ozone – in individual systems. Their surveys will provide the first assessment of potential habitability around stars of different masses and thus the true context for life on Earth. Technological innovation, atmospheric characterization, and demographic studies of young jovian planets over the past decade provide first, key steps towards this goal.

In this Chapter, we provide an updated description of

the state of our knowledge about detecting and characterizing exoplanets by direct imaging. The last dedicated direct imaging review chapter in *Protostars and Planets* was written in 2007 ([Beuzit et al. 2007](#)), before the first incontrovertible exoplanet imaging detections: superjovian planets around HR 8799 and β Pic ([Marois et al. 2008b, 2010b](#); [Lagrange et al. 2010](#)). Previous reviews from [Traub and Oppenheimer \(2010\)](#) and [Bowler \(2016\)](#) bracket the start and end of the era of direct imaging surveys with facility, conventional AO systems. Now, >5 years later, the first generation of extreme AO surveys have ended, bringing new discoveries, fundamentally new insights into atmospheric properties of individual systems and imaged planet demographics, motivating substantially more powerful instrumentation and tangible plans for directly detecting true solar system analogues, including Earths.

This Chapter is pedagogical in nature and is organized as follows. In Section 2, we outline key direct imaging instrumentation and methods, describing the challenges in achieving planet detections by direct imaging, and detailing critical, novel hardware and software needed to image planets. Section 3 summarizes our current inventory of directly imaged exoplanets, discusses challenges with interpreting direct imaging detections, and outlines synergies with other detection techniques. Section 4 focuses on atmospheric characterization of exoplanets by direct imaging and spectroscopy, using other substellar objects (i.e. brown dwarfs) as anchors to provide empirical constraints on exoplanet atmospheres and employing atmospheric models to infer intrinsic properties, including clouds, chemistry, and gravity. Next we overview the architecture of directly imaged planetary systems gleaned from astrometric monitoring, dynamical models, and planet-disk interactions (Section 5). Section 6 summarizes recent direct imaging surveys, the occurrence rates and demographics derived from them, and what these results mean for models of jovian planet formation. Finally, in Section 7 we forecast the future of direct imaging, describing how technological innovations and new, vastly more powerful facilities may provide humanity with a glimpse of a habitable world for the first time.

2. Direct Imaging Instrumentation and Methods

Direct imaging detections require separating the halo of bright, highly structured scattered starlight from faint exoplanet light. The key metric used to determine the detectability of extrasolar planets is the planet-to-star contrast ratio at a given off-axis angular separation: the contrast ratio needed for a detection varies with planet properties (Sect 2.1). Critical hardware like AO – or (more generally) wavefront control systems consisting of sensors and deformable mirrors – and coronagraphs sharpen and then suppress scattered starlight (Sect 2.2) to achieve deep raw contrasts. Novel observing techniques allow post-processing algorithms to further remove residual starlight, increasing achievable contrast ratios and thus improving planet detection capabilities (2.3).

2.1. Detectability of Planets by Direct Imaging

Even in the absence of an atmosphere to blur starlight, an astronomical image of a point source (e.g. a distant star) will not be a single point: its intensity distribution follows from the Fourier transform of the telescope pupil function. For a simple unobscured circular aperture, the image intensity follows an Airy pattern whose values compared to the peak intensity (I_o) at angular separation ρ , effective telescope aperture diameter D_{tel} , and wavenumber $k = 2\pi/\lambda$ is $I = I_o \left[\frac{4J_1(0.5kD_{\text{tel}}\sin\rho)}{D_{\text{tel}}\sin\rho} \right]^2$, where J_1 is the Bessel function of the first kind of order one. The first null of the Airy function occurs at $\sim 1.22 \lambda/D_{\text{tel}}$. The *full-width at half-maximum* (FWHM) of this point source on the sky, defining the telescope diffraction limit, is given by

$$\theta(\")_{\text{FWHM}} \sim 0.21 \left(\frac{\lambda(\mu\text{m})}{D_{\text{tel}}(\text{m})} \right). \quad (1)$$

Even current telescopes in principal have the angular resolution needed to image planets on solar system-like scales orbiting nearby stars. An Earth twin orbiting at a projected separation of 1 au from a Sun-like star at 10 pc subtends an angle of $0''.1$. Diffraction limited imaging with the *Hubble Space Telescope* at optical wavelengths or with 8-10m class telescopes like VLT, Subaru, and Keck at near-infrared (IR) wavelengths is sufficient to resolve objects at Earth-Sun projected physical separations out to a distance of 10–20 pc. However, the star’s halo light must be reduced through hardware and software to a level sufficient to make the planet’s light detectable. The starlight suppression level required to detect a planet by direct imaging depends on whether the detection is in reflected light or thermal emission and varies with the planet angular separation, age, size, temperature, and other properties (see Figure 2).

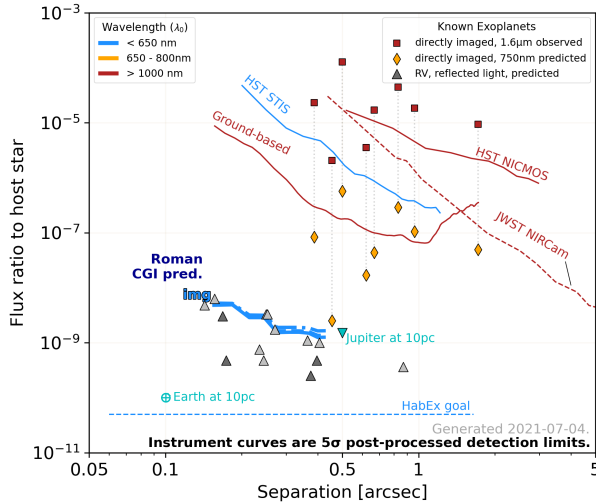


Fig. 2.— Contrast vs. angular separation for current and future ground and space-based high-contrast imaging platforms vs. measured and predicted contrasts for selected directly imaged planets, radial-velocity (RV) detected planets, and Earth and Jupiter analogues. Generated using tools developed by Vanessa Bailey, which are available at: <https://github.com/nasavbailey/DI-flux-ratio-plot>.

2.1.1. Reflected Light

Planets reflect the light of the stars they orbit. At optical wavelengths, the contrast ratio for a planet in reflected light can be approximated as

$$C_{\text{optical},\lambda} \sim A_g(\lambda) \phi(\lambda, \alpha) \left(\frac{r_p}{a_p} \right)^2, \quad (2)$$

where r_p is the planet radius, a_p is the planet-to-star physical separation, A_g is the visible geometric albedo spectrum, ϕ is the phase function as a function of α , the phase angle, which is the angle between the star, planet, and observer (Greco and Burrows 2015; Traub and Oppenheimer 2010). A_g and ϕ depend on the planet’s atmospheric properties. For a Lambertian phase function, valid for high albedo atmospheres, the phase function follows a simple relation of $\phi(\alpha) = [\sin(\alpha) + (\pi - \alpha)\cos(\alpha)]/\pi$, where $\phi = 1/\pi$ at maximum elongation ($\alpha = \pi/2$). Other potential scattering phase functions include isotropic scattering and Rayleigh scattering. The value of ϕ is considerably lower for Rayleigh scattering appropriate for jovian atmospheres at angles of 60–90° (Madhusudhan and Burrows 2012).

For an exo-Jupiter and exo-Earth emitting as Lambertian spheres with measured geometric albedos of 0.52 and 0.367, these contrasts at maximum elongation reduce to:

$$C_{\text{optical},J} \sim 1.4 \times 10^{-9} \left(\frac{r_p}{r_J} \right)^2 \left(\frac{5.2 \text{ au}}{a_p} \right)^2 \quad (3)$$

and

$$C_{\text{optical},\oplus} \sim 2.1 \times 10^{-10} \left(\frac{r_p}{r_{\oplus}} \right)^2 \left(\frac{1 \text{ au}}{a_p} \right)^2, \quad (4)$$

where r_J and r_{\oplus} are the radii of Jupiter and Earth respectively. At V band, a Jupiter and Earth at 10 pc will then have apparent magnitudes of slightly greater than 27 and 29, respectively, and require starlight removal at angular separations of $0''.5$ and $0''.1$ better than one part in 10^{-9} and 10^{-10} , respectively. These required contrasts are well beyond the capabilities of current ground and space-based high-contrast imaging instruments. Thus far, exoplanet direct imaging has therefore focused on the detection of thermal emission from self-luminous jovian planets.

2.1.2. Thermal Emission

Like brown dwarfs, jovian planets cool and contract with time, releasing gravitational potential energy as thermal emission (e.g. Burrows et al. 2001). At ages of 1–10 Myr, models for the luminosity evolution of 1–10 M_J exoplanets predict temperatures of ≈ 500 –3000 K and radii up of $r_p \sim 2.5$ –3 R_J . By 1 Gyr, these models predict that these planets cool to temperatures $T \lesssim 500$ K and contract to Jupiter-like radii ($r_p \sim 1$ –1.2 R_J) (e.g. Fig. 5 in Spiegel and Burrows 2012). Thus, thermal emission from young jovian exoplanets peaks at near-to-mid IR wavelengths at the youngest ages, moving to well into the mid-IR at older ages (Figure 3). The contrast ratio for planets in thermal

emission depends on the radius and effective temperature of the planet and star and other properties:

$$C_{\text{IR},\lambda} \sim \frac{F_{\lambda,p}(T, X) r_p^2}{F_{\lambda,s}(T) r_s^2}, \quad (5)$$

where $F_{\lambda,p}(T, X)$ is the thermal flux from the planet as a function of wavelength, $F_{\lambda,s}(T)$ is the thermal flux from the star as a function of wavelength, and X depends on the planet’s atmospheric characteristics, such as clouds, chemistry, and gravity.

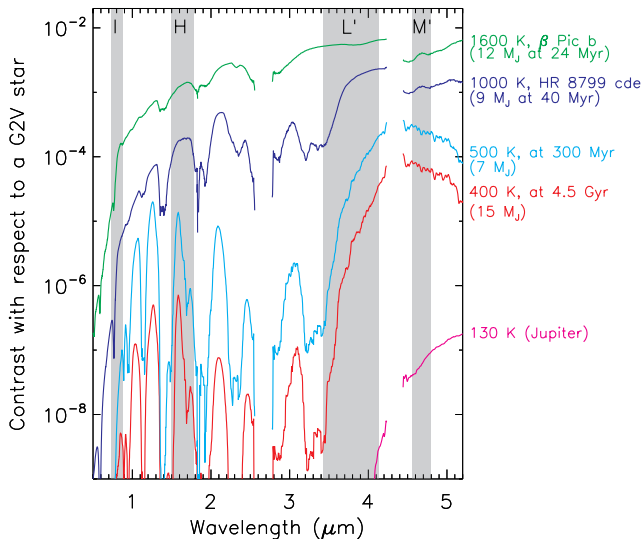


Fig. 3.— Contrast ratio vs. selected optical, near IR, and mid-IR passbands for models for known directly imaged planets (β Pic b and HR 8799 cde), models for older cooler exoplanets, and Jupiter assuming a G2V primary in all cases. The actual planet-to-star contrast ratios for β Pic b and HR 8799 cde are 5–10 times higher as they orbit intrinsically brighter, hotter stars. Plot adapted and modified from *Skemer et al. (2014a)*. Models drawn from *Currie et al. (2011)*; *Madhusudhan et al. (2011)*; *Burrows et al. (2003)*.

Fig. 3 shows how the contrast ratios vary for various types of exoplanets orbiting a G2V star. In the near-IR, young superjovian ($\sim 10 M_J$) exoplanets similar to β Pic b and HR 8799 cde are roughly a factor of 10^{-3} to 10^{-5} fainter than a Sun-like star. In the red optical, predicted contrasts from these planets are 100 times larger; however, mid-IR contrasts are a factor of 10 smaller. Jovian exoplanets of similar masses around much older stars are far cooler – another factor of 100–1000 fainter in the red optical and near-IR – but remain bright in the mid IR. A true Jupiter analogue emits negligible thermal emission shortward of $\lambda \sim 4\text{--}5 \mu\text{m}$. Rocky terrestrial planets also emit thermally. An exo-Earth analogue with $T_{\text{eff}} \approx 260 \text{ K}$ has blackbody emission peaking at $10 \mu\text{m}$: its contrast ratio is $\approx 10^{-7}$, a factor of ≈ 1000 shallower than its reflected light contrast.

2.2. Wavefront Control and Coronagraphy

2.2.1. Atmospheric Wavefront Control for Direct Imaging

Wavefront errors, whether induced by atmospheric turbulence on the ground or intrinsic to an optical imaging

system on the ground or in space, substantially limit an image system’s achievable contrast. Left unmitigated, these errors preclude the direct detection of exoplanets. In the past decade, the direct imaging field has made key strides in wavefront control hardware and software to drastically reduce wavefront errors and has developed sophisticated coronagraph designs to further suppress diffracted starlight.

For ground-based imaging systems, turbulence arising from many atmospheric layers along the path from the star to the telescope induces changes in the optical path length difference of starlight (*Guyon 2005*), blurring images. These aberrations must be corrected by an AO system consisting of wavefront sensors and deformable mirrors (DMs). An AO system splits incoming light from a guide star between the science detector and a wavefront sensor to measure and then correct – with a DM(s) – atmospheric turbulence distorting the incoming wavefront, sharpening starlight at the image plane.

Key terms driving the wavefront error budget for an AO system include 1) measurement error (σ_m) which depends on the noise properties of a wavefront sensor and the guide star brightness, 2) temporal bandwidth error (σ_t) which depends on the AO system time lag τ compared to the atmospheric coherence time τ_o , and 3) the fitting error (σ_f) which depends on the coherence length r_o compared to the DM actuator density. The quadrature-added sum of these terms sets the Strehl ratio – a measure of the optical quality of the image – and the raw contrast vs. angular separation (e.g. *Tyson 1998*). At the angular separations relevant for most current planet searches ($\theta \sim 0''.2\text{--}1''.0$), wavefront measurement error and temporal bandwidth error set the contrast floor. Wavefront chromaticity and non-common path aberrations due to instrument optics can also limit contrast (*Guyon 2005*; *Currie et al. 2020a*).

Facility, conventional AO systems were used for the first direct imaging searches. They typically sample and correct the incoming wavefront at frequencies of 0.2–1 kHz and use DMs with a few hundred actuators: aberrations are measured by standard Shack-Hartmann wavefront sensors (e.g. see *Tyson 1998*). These systems yielded partial corrections, achieving modest Strehl ratios ($\text{SR} \sim 0.1\text{--}0.4$) at near-IR wavelengths focused on by most exoplanet imaging searches (e.g. *Lafrenière et al. 2007b*).

The past 5–10 years have seen the deployment of numerous extreme AO systems on 5–10m telescopes, which have wavefront control loop speeds of $\gtrsim 1 \text{ kHz}$ and DMs with $\gtrsim 1000$ actuators. Examples of extreme AO systems include the *Large Binocular Telescope Adaptive Optics* system (LBTAO), PALM-3000 on the Hale telescope at Palomar Observatory, the *Gemini Planet Imager* on Gemini-South, and the *Spectro-Polarimetric High-contrast Exoplanet REsearch* instrument (SPHERE) at the VLT, the *Subaru Coronagraphic Extreme Adaptive Optics* project (SCEAO) on the Subaru Telescope, and MagAO-X on the Clay telescope at the Magellan Observatory (*Esposito et al. 2011*; *Dekany et al. 2013*; *Macintosh et al. 2014*; *Beuzit et al. 2019*; *Jovanovic et al. 2015*; *Males et al. 2020*). These

systems obtain higher-quality AO corrections – Strehl ratios of 0.7–0.95 at $1.6 \mu\text{m}$ – and yield a factor of 10–100 deeper contrast at sub-arcsecond separations than conventional AO systems (e.g. [Macintosh et al. 2014](#)).

Extreme AO systems have relied on hardware developments in three key areas to operate high-performance AO correction: detectors, deformable mirrors, and computing hardware. Most extreme AO platforms utilize fast ultra-low noise detectors like *Electron-Multiplying Charge-Coupled Devices* (EMCCDs) to record stellar photons used for wavefront sensing with reduced measurement errors (e.g. [Jovanovic et al. 2015](#); [Beuzit et al. 2019](#); [Males et al. 2020](#)). High-actuator count DMs are now available. For example, the microelectromechanical-type DMs (MEMS) offer unprecedented actuator density (≈ 10 act per square mm), allowing for fairly compact extreme AO instruments (e.g. [Macintosh et al. 2014](#); [Jovanovic et al. 2015](#); [Males et al. 2020](#)). Other systems employ adaptive secondary mirrors (usually voice-coil DMs) whose low emissivity makes them especially well suited for exoplanet imaging in thermal IR ([Esposito et al. 2011](#)). High performance computing hardware with low latency can handle the demanding computation requirements of fast, high order extreme AO systems.

Extreme AO systems also differ from conventional AO systems in their optical design and system architecture. Wavefront sensors (WFS) optimized for speed, sensitivity, accuracy and precision such as the Pyramid wavefront sensor have been adopted by many leading extreme AO systems (top panel of Figure 4, [Esposito et al. 2011](#); [Jovanovic et al. 2015](#); [Males et al. 2020](#)), while the more established Shack-Hartmann WFS approach has been upgraded with spatial filtering to improve performance. Wavefront correction is often performed in two steps: a conventional coarse “woofer” correction is followed by a faster and more accurate “tweeter” correction (e.g. [Macintosh et al. 2014](#)). Extreme AO systems also include dedicated sensing and control of pointing for precise co-alignment of the star and coronagraph mask ([Singh et al. 2015](#); [Shi et al. 2017](#); [Huby et al. 2017](#)), which is essential to maintain high contrast, especially at the smallest angular separations.

Advances in wavefront control algorithms are also enabling significant improvements in high-contrast imaging performance. Recent advances include predictive control and sensor fusion. These and other new software/hardware advances are described in Section 7.1.

2.2.2. Optical Starlight Suppression

Starlight suppression is primarily performed by dedicated coronagraph optics: phase and amplitude masks deployed in the beam to remove starlight while preserving planet light. These optical elements include occulters in the image plane to directly block out on-axis starlight, as well as optical elements in the pupil plane to manage the telescope diffraction pattern. Many coronagraph designs and approaches are available (e.g. [Kuchner and Traub 2002](#); [Kasdin et al. 2003](#); [Sivaramakrishnan et al. 2005](#); [Guyon](#)

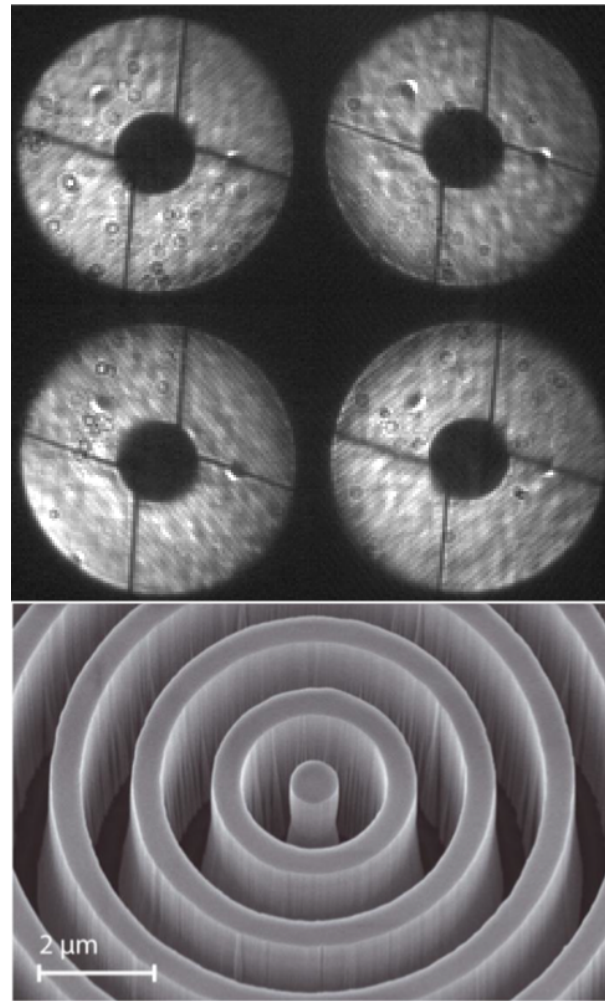


Fig. 4.— Some key high-contrast imaging hardware components. (top panel) Wavefront control with a Pyramid WFS and high-performance camera: images of the 4 pupils created by a pyramid optic and acquired by a photon counting, high speed, low-latency EMCCD ([Jovanovic et al. 2015](#)). (bottom panel) Advanced starlight suppression masks: electron scanning microscopic image of an annular groove phase mask (“vector vortex” coronagraph) ([Mawet et al. 2012](#); [Delacroix et al. 2013](#)).

[et al. 2006](#); [Kenworthy et al. 2007](#); [Mawet et al. 2010](#); [Ottén et al. 2017](#)), providing a wide range of performance characteristics. For example, the well-established conventional Lyot coronagraph combines an occulter in the image plane with a Lyot stop in the pupil plane to deliver robust performance at moderate contrast and large angular separations. Phase-mask coronagraphs or interferometric designs (e.g. the vector vortex coronagraph) can be highly optimized for deep contrast at small inner working angles (Figure 4, bottom panel). The highest-performing coronagraphs are also the most demanding in terms of wavefront quality and stability. Consequently, extreme AO systems first adopted Lyot coronagraphs, while more recent systems or upgrades deploy higher performance solutions as the corresponding wavefront quality improves.

Wavefront control is also becoming an important component of starlight suppression in the form of speckle con-

tol. In speckle control, a feedback loop from the post-coronagraph image to an upstream deformable mirror allows for residual speckles to be measured and canceled. This approach has been used in laboratory testbed to reach deep contrast levels (10^{-7} – 10^{-10}) in support of future space-based missions. Deployment on ground-based systems remains challenging due to the dynamic nature of atmospheric turbulence, but has been successful in removing a fraction of static and slow speckles (*Codona and Kenworthy 2013; Martinache et al. 2016; Gerard et al. 2018; Bos et al. 2021*). Sensing and compensation of non-common path aberrations can also be performed using a dedicated sensor, e.g. a Zernike phase-mask sensor (*Vigan et al. 2019*).

2.3. Observing, Post-Processing, and Spectral Extraction Methods

At sub-arcsecond separations, the raw (instrument-delivered) planet-to-star contrasts obtained by the first generation of facility and now extreme AO systems – 10^{-3} – $10^{-4.5}$ – are still too shallow to yield decisive detections of many young jovian exoplanets. Residual quasi-static speckle noise, due to nanometer-scale imperfections in telescope optics, thermal flexure, etc., limits instrumental contrasts and fails to simply average out over time like photon (“white”) noise (*Hinkley et al. 2007*). Speckle noise statistics follow a modified Rician distribution whose long positive tail can lead to many false positives (*Marois et al. 2008a; Soummer et al. 2007*). Therefore, novel observing techniques coupled with advanced post-processing methods are critical to optimizing our ability to image exoplanets by further suppressing stellar halo light by orders of magnitude and making residual noise more Gaussian (“whitening”).

Various forms of differential imaging techniques are utilized to remove speckle noise for direct imaging. Commonly used techniques include:

- **Angular Differential Imaging (ADI)** (*Marois et al. 2006*) – ADI exploits the quasi-static nature of residual speckle noise in AO corrected high-contrast images from the ground and diffraction-limited imaging from space. For ground-based AO imaging, quasi-static speckles evolve on a characteristic timescale of ~ 10 s of minutes to an hour or more (*Hinkley et al. 2007*). For space-based imaging, PSF breathing due to thermal variations and other small mechanical changes cause the quasi-static halo to evolve, but the halo for a given target can remain well correlated for months or years. By turning off the instrument rotator that keeps north fixed on the detector (on the ground) or obtaining observations at different roll angles (space), astrophysical objects off-axis from a star change position angle on the detector while the speckle halo remains fixed. Subtracting images obtained in an ADI sequence can then suppress speckle noise without fully suppressing planet signals.

ADI efficiently suppresses speckles on the ground

and in space (*Marois et al. 2006*). It is the most widely used observing method in direct imaging. ADI’s advantages are most limited at small angular separations where the displacement of the planet’s PSF is smallest for a given parallactic angle change or roll angle change. Typically, ADI induces signal loss, which must be corrected to achieve absolute spectrophotometric calibration for planets (see below).

- **Spectral Differential Imaging (SDI)** (*Marois et al. 2000; Sparks and Ford 2002; Biller et al. 2004*) – At raw contrasts shallower than the 10^{-7} levels needed to image self-luminous jovian exoplanets, achromatic phase errors dominate the wavefront errors responsible for the speckle halo (e.g. *Shaklan and Green 2006; Bailey et al. 2018*). For data obtained simultaneously at multiple wavelengths – e.g. dual-channel imaging or an integral field spectrograph (IFS) – the speckle halo as a function of wavelength, scaled in radius by the central passband wavelength, is extremely well correlated. Since the images at different wavelengths are obtained simultaneously with the target, they do not suffer from temporal decorrelation as with ADI (e.g. *Marois et al. 2014*). SDI then suppresses the speckle halo in a given passband by constructing a reference PSF drawn from (rescaled) images at other wavelengths.

Like ADI, SDI induces signal loss and is least effective at small angular separations, where bandpass rescaling yields small displacements of a (de)magnified planet PSF. SDI’s efficacy is also limited by non-common path errors, differential sampling of the point-source PSFs across wavelength channels, and the spectrum of the planet to be detected (e.g. *Gerard et al. 2019; Marois et al. 2014*). Extracting throughput-corrected spectra from data processed with SDI is also more challenging than with other differential imaging techniques (*Pueyo 2016*).

- **Reference Star Differential Imaging (RDI)** – RDI subtracts the PSF of a companion-less reference star from the target. It is widely used in the ultra-stable environment of space. While ADI and SDI may yield superior speckle suppression at moderate to wide separations, RDI may be advantageous at very small angular separations where other techniques suffer from self subtraction (*Xuan et al. 2018*). RDI requires a very stable PSF to efficiently operate. Using it on ground-based telescopes may require fast switching between the target and reference star(s) for maximum contrast gain (e.g. *Wahhaj et al. 2021*); in broad bandpasses, it also requires a reference star that is extremely well color matched (e.g. *Krist et al. 1998*).

These differential imaging techniques are used in combination with PSF subtraction algorithms. Many widely-used, advanced PSF subtraction methods are different forms of least-squares algorithms, which construct a reference PSF

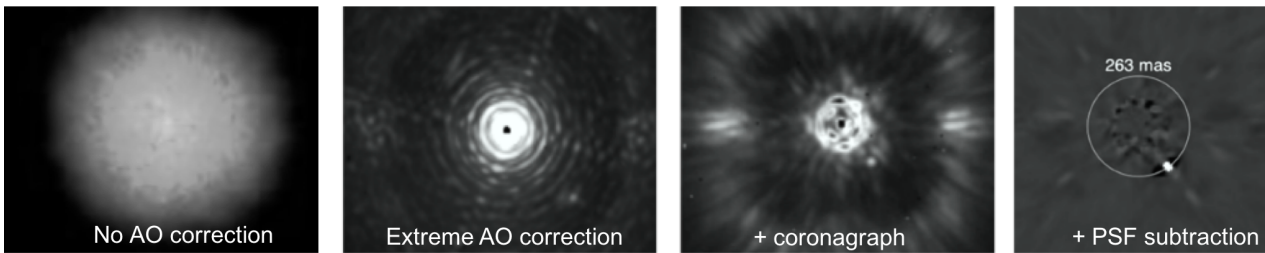


Fig. 5.— A demonstration of high-contrast imaging hardware and software with SPHERE. Seeing limited point-spread function (PSF) (left) sharpened by an extreme AO system (middle left) with scattered starlight further suppressed by a coronagraph (middle right) and advanced PSF subtraction methods (right).

that minimizes the variance when subtracted from a given target image. The *locally-optimized combination of images* (LOCI) algorithm constructs a reference PSF from a linear combination of reference images weighted by coefficients \mathbf{c} determined from the solution to the matrix equation $\mathbf{c} = \mathbf{A}^{-1}\mathbf{b}$ (Lafrenière et al. 2007a), where \mathbf{A} is the (square) covariance matrix for the reference library and \mathbf{b} is the column matrix populated by elements multiplying each reference image by the target image. Another approach exploits *principal component analysis* (PCA), computing the Karhunen-Loève transform of the reference image set and projects this set onto the target image to construct a combination of weighted eigenimages to subtract from the target (Karhunen-Loève Image Plane algorithm, henceforth KLIP, Soummer et al. 2012; Amara and Quanz 2012). Multiple successor algorithms such as TLOCI and A-LOCI draw from the lineage of LOCI and/or KLIP, employing advances such as correlation-based frame selection, pixel masking, various rank-truncations of the covariance matrix, free parameter optimization or exploiting high-performance computing to solve for the variance-minimizing coefficients directly (e.g. Marois et al. 2010a, 2014; Currie et al. 2012b, 2015; Thompson and Marois 2021). Separate approaches involve maximum-likelihood methods to model and remove the stellar PSF (e.g. Cantalloube et al. 2015) or statistically modeling non-stationary covariances in small regions of images to improve PSF subtraction (e.g. the PACO algorithm Flasseur et al. 2018).

The relative performances of these algorithms vary in the literature and may depend on their exact implementation and suitability for a particular data set, although some work suggests that the newer algorithms descended from LOCI and KLIP can offer significant improvements (e.g. Rameau et al. 2013b; Thompson and Marois 2021). In general, all of these algorithms enable significant contrast gains over simple, classical methods, especially at small angular separations (Lafrenière et al. 2007a; Currie et al. 2014a).

ADI, SDI, and RDI combined with PSF subtraction methods can attenuate and distort planet signals. The first methods to measure these biases and recover true planet flux measurements and astrometry injected synthetic planets into data at other locations or iteratively subtracted negative copies of planets at their apparent positions (e.g. Lafrenière et al. 2007a; Lagrange et al. 2010). Recently, several authors have developed efficient forward-modeling

methods to estimate photometric and astrometric biases at the planet’s location (e.g. Pueyo 2016). Planet forward-models in turn can be used as matched filters to improve planet detection capabilities themselves (Ruffio et al. 2017).

Analyses of images whose speckle noise is partially suppressed by advanced PSF subtraction techniques have revised notions of how to quantify detection significances and spectroscopic uncertainties. For instance, finite sample sizes impact our definitions for contrast limits drawn from images with noise whitened by KLIP, LOCI, and other algorithms, especially at small ($1-3 \lambda/D$) separations (Mawet et al. 2014; Pairet et al. 2019). In IFS data, residual speckle noise may be spatially and spectrally correlated. Considering the full spectral covariance has a substantial impact on deriving planet atmospheric parameters from model comparisons (Greco and Brandt 2016).

Figure 5 shows the combined effect of high-contrast imaging hardware and software on imaging exoplanets, stepping through the successive improvements found from using extreme AO, coronagraphy, and PSF subtraction.

3. Direct Imaging Detections

3.1. Taxonomy of Directly-Imaged Companions

Figure 1 shows the demographics of planetary mass companions to stars detected via various methods. Community consensus on the planethood of many imaged objects (e.g. HR 8799 bcde, β Pic bc, 51 Eri b, etc.) is clear. However, identifying the exact criteria needed to distinguish between planets and brown dwarfs is challenging.

Planets have often been identified as objects with masses below the deuterium-burning limit, nominally $13 M_J$ (e.g. the IAU Working Group Definition). However, this simple criterion is poorly motivated. In addition to being time and metallicity dependent (Spiegel et al. 2011), deuterium burning arguably does not identify a meaningful boundary for the evolution of low-mass objects (Chabrier et al. 2007; Luhman 2008), as some objects below the deuterium burning limit have been found in configurations which imply formation by cloud formation and other objects above the deuterium burning limit have been found in configurations which imply formation like a planet in a disk. For instance, recent imaging surveys have found objects that are members of quadruple systems, clearly formed by molecular cloud fragmentation, with inferred masses down to 5

M_J and free-floating objects with sub-deuterium burning masses as well (Todorov et al. 2010; Liu et al. 2013). In contrast, RV surveys have identified some systems – e.g. the $2.7 M_\odot$ star ν Oph – with companions at ~ 1 au with masses of 22 and $24 M_J$ that are nevertheless locked in a mean-motion resonance indicating formation in a disk (i.e. like a planet) (Quirrenbach et al. 2019). The physics of planet formation does not require that gas accretion shuts off once $13 M_J$ of material is accreted.

An alternate definition leverages formation processes: a planet is an object formed in a circumstellar disk around a young star. Demographic analyses of substellar objects can provide empirically-motivated criteria for separating planets from brown dwarfs. Studies of the substellar mass function from previous RV surveys and recent ones (i.e. the California Legacy Survey) show a local minimum at $m \sin(i) \sim 16\text{--}30 M_J$ (e.g. Sahlmann et al. 2011; Kiefer et al. 2019; Currie et al. 2022a). The minimum in the companion mass function may be proportional to the primary mass, indicating that companion mass ratio (q) could be a key discriminator (Grether and Lineweaver 2006). Theory also suggests that the semimajor axes (a_p) and mass ratios (q) of companions also help distinguish between bona fide planets and brown dwarfs (Kratter et al. 2010; Currie et al. 2011). Binary companions to more massive stars with $q \gtrsim 0.025$ are exceptionally rare (Kraus et al. 2008; Reggiani et al. 2016). Distributions of protoplanetary disk radii peak at ~ 200 au and fall to low frequencies by ~ 300 au (e.g. Andrews and Williams 2007): companions at wider separations are far less likely to have formed from a disk unless scattered to their current locations by unseen companions. Thus, we set the following limits for a planet vs. a brown dwarf: mass $< 25 M_J$, $q < 0.025$, and $a_p \lesssim 300$ au.

Our linked spreadsheet lists the current inventory of directly imaged exoplanets, protoplanets, higher mass-ratio/wider separation planet-mass companions, and controversial cases: <https://tinyurl.com/srb33b>. As of 19 October 2022, we identify 22 directly imaged exoplanets that fit our criteria, three of which are imaged protoplanets. We also list another 34 dozen companions that may instead be better considered as brown dwarfs instead of planets (including companions orbiting brown dwarfs), and 6 “controversial” cases. Some of these individual classifications will undoubtedly change pending new analysis as may the exact values used to separate planets from brown dwarfs. Objects in each category will certainly be added over the next few years.

Below, we describe general properties of fully-formed directly imaged planets within 300 au and discuss three well-studied, emblematic cases (HR 8799, β Pic, and 51 Eri). We also summarize our current knowledge of protoplanets and challenges with identifying imaged exoplanets.

3.2. Fully-formed Exoplanets

3.2.1. General Properties

Most directly imaged planets known thus far have near-IR contrasts ranging between 10^{-4} (e.g. κ And b) and 10^{-6} (51 Eri b). All of them are self-luminous, made visible by thermal radiation released as the planets cool and contract. On the sky, the planets generally lie at angular separations of $0''.2$ to $2''.0$ ($\sim 5\text{--}40 \lambda/D$ for an 8m telescope).

Stars hosting imaged exoplanets typically have ages of 10–100 Myr; many are found in young nearby stellar associations (often < 100 pc, with ages < 100 Myr) that share similar kinematics (proper motions, space motions) and formed in the same star-forming region, such as Sco-Cen or the β Pic Moving group (e.g. Zuckerman and Song 2004; Zuckerman et al. 2011; Song et al. 2003; Schlieder et al. 2012; Schneider et al. 2012; Shkolnik et al. 2012). (see Section 6.1 for more details on such associations as sites for exoplanet searches). Most stars with imaged planets to date are B, A, or F stars, at least 50% more massive than the Sun. Most systems with imaged planets – including systems with the first detections (HR 8799, β Pic) – also have Kuiper belt-like debris disks.

Planets detected to date share similar spectral types and temperatures with more massive field brown dwarfs, but often show evidence of low surface gravity in their spectra (Barman et al. 2011b,a). Brown dwarfs and exoplanets alike cool monotonically with age, beginning life as hot M-type objects, cooling to the L spectral type (with very red near-IR colors and silicate condensate clouds (Kirkpatrick 2005), the cooler T spectral type (with blue near-IR colors and strong methane absorption at $1.6 \mu\text{m}$ and $2.2 \mu\text{m}$, Kirkpatrick 2005) and eventually to the very cool Y spectral type (Cushing et al. 2011; Kirkpatrick et al. 2012). Thus, there is an age / mass / temperature degeneracy for these objects, rendering mass estimates based on models very sensitive to the age assumed for the system.

Most mass estimates for imaged planets depend on luminosity evolution models, challenges for which are described in Section 3.4. Some planets – e.g. HR 8799 bcde, β Pic b, 51 Eri b, and HD 206893 b – have dynamical mass measurements or limits. Masses inferred from luminosity evolution or derived from dynamics are typically $\sim 5\text{--}10 M_J$. Some planets have masses near the deuterium-burning limit (κ And b, HD 206893 b); 51 Eri b may have a far lower mass (as little as $\sim 2 M_J$). Mass ratios for most imaged planets are $q \sim 0.005\text{--}0.01$: 51 Eri b may have the lowest mass ratio ($q \sim 0.001$). Even leading extreme AO systems are typically not sufficiently sensitive to detect young Jupiter-mass planets, let alone Saturn-mass planets. However, future capabilities will close these gaps (See Section 7).

3.2.2. Emblematic Systems

While planetary mass companions to brown dwarfs had previously been detected as early as 2004 (most notably 2M1207b, Chauvin et al. 2004), the near simultaneous announcements of HR 8799bcd and β Pic b are widely

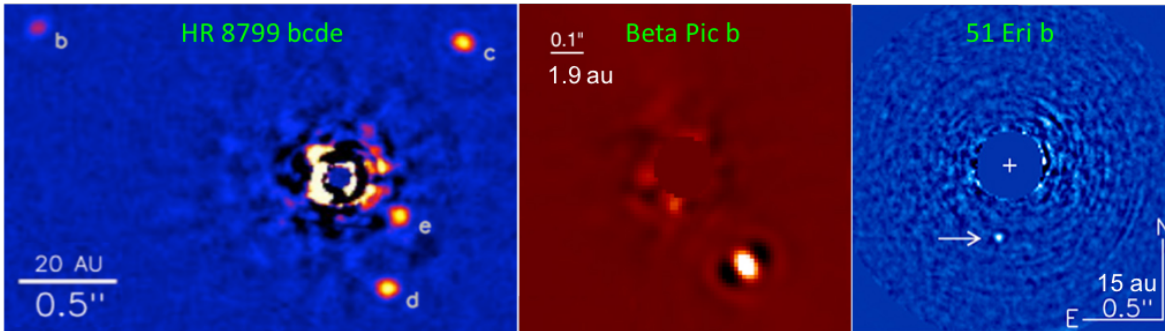


Fig. 6.— Well-studied directly-imaged exoplanetary systems: (left) HR 8799, (middle) β Pic, and (right) 51 Eri. Images draw from *Marois et al. (2010b)*, *Lagrange et al. (2019)*, and *Macintosh et al. (2015)*, respectively. Note that β Pic c is not visible in the middle panel: the HR 8799 and 51 Eri images show the full complement of known planets in each system.

regarded as the first bonafide directly-imaged exoplanet detections (*Marois et al. 2008b*; *Lagrange et al. 2009*). Planets in both systems were detected from ground-based facility AO systems in the near-to-mid IR in thermal emission, not scattered light. Just over 7 years later, *Macintosh et al. (2015)* announced the first exoplanet discovered with extreme AO: 51 Eri b.

HR 8799 – HR 8799 is a nearby (~ 40 pc) mid-A field star with an estimated age of ~ 40 Myr (*Baines et al. 2012*). The star hosts a massive, resolved Kuiper belt-like debris disk and a warm debris population interior to 10 au consistent with an asteroid belt (*Sadakane and Nishida 1986*; *Su et al. 2009*; *Matthews et al. 2014*; *Booth et al. 2016*): possible signposts of massive, perturbing planets.

In 2008, *Marois et al.* announced the direct imaging discovery of HR 8799 bcd followed by a fourth planet discovery in 2010 (HR 8799 e; *Marois et al. 2010b*), located at projected separations of 15–70 au (Figure 6, left panel). Soon after HR 8799 bcde’s announcements, other studies identified one or more planets in archival or separately-obtained data (*Lafrenière et al. 2009*; *Fukagawa et al. 2009*; *Metchev et al. 2009*; *Soummer et al. 2011*; *Currie et al. 2011, 2012a*). A decade of Keck Observatory monitoring showed that HR 8799 bcde orbit close to the 1:2:4:8 resonance (*Konopacky et al. 2016*). Current analyses suggest that the planet orbits are nearly coplanar with the disk, with a small inclination of $\sim 27^\circ$ (*Konopacky et al. 2016*). However, HR 8799 e may not orbit on a plane strictly coplanar with HR 8799 bcd (*Gravity Collaboration et al. 2019*).

Originally, masses inferred from the planets’ luminosities spanned a wide range of values (5–13 M_J) (*Marois et al. 2008a, 2010a*). However, dynamical stability modeling strongly favors masses below 10 M_J (7 M_J) for HR 8799 cde (HR 8799 b) (*Marois et al. 2010a*; *Currie et al. 2011*; *Sudol and Haghighipour 2012*). Using *Hipparcos* and *Gaia*, *Brandt et al. (2021b)* measured a dynamical mass for HR 8799 e of $9.6^{+1.9}_{-1.8} M_J$, consistent with these limits (see Section 3.5). Additional planets may explain the shape of the inner edge of HR 8799’s cold belt (*Booth et al. 2016*), especially if they are near or below Jupiter’s mass (*Goździewski and Migaszewski 2018*). Any planets interior to HR 8799 e must be below 3–4 M_J at 7–10 au and 5–6

M_J at 4–7 au (*Zurlo et al. 2016*; *Wahhaj et al. 2021*; *Brandt et al. 2021b*). The HR 8799 planetary system resembles a scaled-up version of our own outer solar system (*Marois et al. 2010a*).

HR 8799 bcde have been benchmark objects for understanding the atmospheres of young jovian planets. Their photometry and low-resolution spectra differ from those of older, field substellar objects thought to have similar temperatures, identifying features diagnostic of clouds, chemistry, and gravity (*Currie et al. 2011*; *Barman et al. 2011a*; *Galicher et al. 2011*; *Marley et al. 2012*; *Bonnefoy et al. 2014b*). Higher resolution spectra probe molecular abundances connected to formation mechanisms (*Konopacky et al. 2013*; *Barman et al. 2015*). Section 4 discusses HR 8799 bcde’s spectra and atmospheres in more detail.

β Pic – The A6V star β Pictoris is the eponymous member of a collection of kinematically-associated stars known as the β Pic Moving Group (age ~ 20 Myr). The star hosts an edge-on debris disk, imaged since the mid-eighties from the ground and space (e.g. *Smith and Terrile 1984*). The disk consists of a planetesimal ring at 70–100 au responsible for the bulk of the dust through collisions and an outer extension comprised of small dust grains blown out by radiation pressure (*Lagrange et al. 2000*).

Lagrange et al. (2009) first identified β Pic b from data obtained in 2003 with VLT/NaCo; follow-up data obtained one year later confirmed the planet (*Lagrange et al. 2010*). Thanks to β Pic b’s small semi-major axis (~ 9 au), over 75% of its orbit has been monitored (*Lagrange et al. 2020*; *Nowak et al. 2020*). More recently, a second planet (β Pic c) was identified from RV data and then recovered with high-contrast interferometric imaging with VLTI/GRAVITY (*Lagrange et al. 2019*; *Gravity Collaboration et al. 2020*).

β Pic b may partially explain the observed warp in the edge-on debris disk and the many evaporating exocomets identified over the past 30 years (*Lagrange et al. 2000*; *Kiefer et al. 2014*). Planets besides β Pic bc could explain why the inner 70 au is relatively devoid of debris dust; localized features in the disk also suggest additional planets could be present. From RV and astrometric data, *Brandt et al. (2021a)* estimate a mass of $9.3^{+2.5}_{-2.6} M_J$ and $8.3 \pm 1 M_J$ for β Pic b and c, respectively (see also *Snellen and*

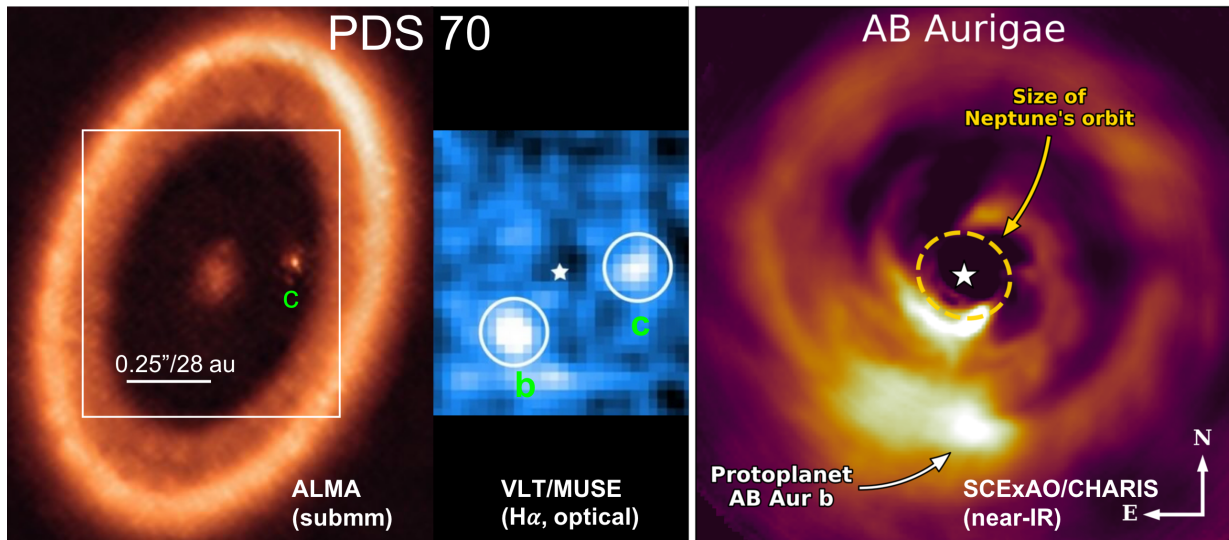


Fig. 7.— (left) ALMA image of PDS 70 showing a cleared protoplanetary disk cavity and a circumplanetary disk around PDS 70 c and H- α image showing the detection of PDS 70 b and c (Benisty et al. 2021; Haffert et al. 2019). (right) SCEXAO/CHARIS image (rescaled by stellocentric distance) of AB Aurigae showing a bright, concentrated emission source revealing the location of a protoplanet (Currie et al. 2022b).

Brown 2018; Nielsen et al. 2020, Section 3.5), although these values heavily depend on the assumed uncertainties on the RV data. RV and direct imaging data combined exclude additional planets more massive than $2.5 M_{Jup}$ from 0.1 au to hundreds of au (Lagrange et al. 2020). β Pic b is more luminous and hotter than the HR 8799 planets ($T_{\text{eff}} \sim 1700\text{--}1800$ K), just slightly redder than field early L-type dwarfs, and is likely cloudy/dusty with a low gravity (Bonney et al. 2013; Currie et al. 2013; Chilcote et al. 2017); β Pic c probably has a temperature intermediate between its sibling and the HR 8799 planets (Nowak et al. 2020).

51 Eri – 51 Eridani is a 29 pc-distant early F star, a member of the ~ 20 Myr-old β Pic Moving Group, and a member of a wide hierarchical triple system that includes an M-dwarf binary GJ 3305 (Feigelson et al. 2006). 51 Eri has a detected infrared excess, modeled with a cold dust belt located approximately between 5 and 80 au (Patel et al. 2014; Riviere-Marichalar et al. 2014).

The GPI campaign (GPIES) team discovered 51 Eri b, a faint planet at $r_{\text{proj}} \sim 13$ au (Figure 6, right panel; Macintosh et al. 2015). The planet is the first discovered using extreme AO and the first incontrovertible T dwarf planet, showing strong methane absorption in H band. The planet is likely more eccentric than either β Pic b or HR 8799 bcde (Maire et al. 2019; De Rosa et al. 2020, $e \sim 0.4\text{--}0.62$). If confirmed, an eccentric orbit could indicate the presence of an additional massive body or could be due to gravitational perturbations from GJ 3305AB. Assuming a hot-start luminosity evolution, current data rule out other planets more massive than $4 M_J$ beyond 5 au and more massive than $2 M_J$ beyond 9 au (Samland et al. 2017).

The mass of 51 Eri b is not well constrained: values derived from comparing 51 Eri b’s luminosity and age to evolutionary models favor $\sim 2 M_J$, while atmospheric model-

ing may favor larger values, up to $\sim 9 M_J$ (Macintosh et al. 2015; Samland et al. 2017). Different characterization studies also find slightly diverging atmosphere properties, illustrating the challenge associated with characterizing very faint exoplanets with direct imaging (Samland et al. 2017; Rajan et al. 2017). Analysis of *Gaia* and Hipparcos astrometry set an upper limit of $11 M_J$ for 51 Eri b (Dupuy et al. 2022). The planet likely has a temperature of ~ 700 K and either lacks clouds or is only partially covered by clouds (Rajan et al. 2017; Samland et al. 2017).

3.3. Protoplanets

Direct images of planets in active assembly (*protoplanets*) around stars that still retain gas and dust-rich protoplanetary disks clarify how and where planets form. The large distances to the nearest star-forming regions (~ 150 pc) mean that protoplanets orbiting their host stars at solar system scales are located at very small angular separations. However, protoplanets can be bright ($L \sim 10^{-2}\text{--}10^{-3} L_{\odot}$), especially if they are surrounded by their own circumplanetary disks (e.g. Zhu 2015).

The 5 Myr-old $0.87 M_{\odot}$ star PDS 70 hosts the first incontrovertible detections of jovian protoplanets: PDS 70 b and PDS 70 c (Keppler et al. 2018, 2019; Müller et al. 2018; Haffert et al. 2019) (Figure 7, left). Both protoplanets are located within the PDS 70 disk cavity, at angular separations of $\rho \sim 0''.18$ and $0''.24$ and estimated semimajor axes ~ 20 and 34 au (Wang et al. 2021). Dynamical arguments strongly favor masses less than $10 M_J$ for PDS 70 b, while PDS 70 c’s mass is more poorly constrained. Masses inferred from SED modeling range between 1 and a few jovian masses (Stolker et al. 2020). PDS 70 b is slightly eccentric ($e \sim 0.17 \pm 0.06$), while PDS 70 c’s orbit is consistent with being circular. The protoplanets’ IR data are best

fit by model atmospheres with substantial dust/extinction.

PDS 70 bc show H_α emission consistent with accretion at rates of $1\text{--}2 \times 10^{-8} M_\odot \text{ yr}^{-1}$, slightly less than the stellar accretion rate (Haffert et al. 2019), but lack evidence for Br- γ accretion (Wang et al. 2021). PDS 70 c shows direct evidence for a circumplanetary disk with an estimated mass of $0.007\text{--}0.03 M_\oplus$. Thermal IR data may suggest that PDS 70 b is surrounded by a circumplanetary disk (Stolker et al. 2020; Wang et al. 2021).

Recently, data from Subaru/SCEXAO and the Hubble Space Telescope over 13 years reveal evidence for a wide-separation (~ 93 au) embedded protoplanet around the 1–3 Myr-old, $2.4 M_\odot$ star AB Aurigae (Currie et al. 2022b). AB Aur b is consistent with a protoplanet responsible for the millimeter dust cavity and CO gas spirals both seen by ALMA (Tang et al. 2017). It appears spatially extended, plausibly due to light from the central source reprocessed by the star’s protoplanetary disk. The best-fit composite model explaining AB Aur b’s optical to near-IR emission includes a $2.75 R_J$, $9 M_J$ source with a surface gravity of $\log(g) = 3.5$, emitting at a much hotter temperature than PDS 70 bc ($\sim 2000\text{--}2500$ K), and accreting at a rate of $\dot{M} \sim 1.1 \times 10^{-6} M_J \text{ yr}^{-1}$. The source is detected in H_α although it is unclear whether this emission is due to accretion. Embedded in a massive disk with numerous spiral arms at over three times Neptune’s disk instead of in a fully cleared cavity like PDS 70 bc, the properties of AB Aur b may point to a planet formation mechanism by disk instability (see Section 6).

Prior to the discovery of PDS 70 bc, other studies claimed detections of protoplanets located within the gaps of or embedded in disks around young stars. The 2-solar mass, protoplanetary disk-hosting star HD 100546 has a protoplanet candidate at ~ 50 au and another at ~ 13 au, just interior to the gap in the protoplanetary disk (HD 100546 bc; Quanz et al. 2013; Currie et al. 2015). HD 100546 b has been detected in multiple data sets but evidence for orbital motion is not yet clear (Rameau et al. 2017; Sissa et al. 2018); HD 100546 c has been imaged in a single data set and inferred through spectroastrometry but not yet imaged in subsequent data (Currie et al. 2015; Brittain et al. 2014; Sissa et al. 2018). Interpreting both candidates – whether a planet or disk feature – is challenging (Currie et al. 2015, 2017; Rameau et al. 2017; Sissa et al. 2018). Both candidates require further study and confirmation.

Two studies presented detections of protoplanets around the young, Sun-like star LkCa 15 through a combination of sparse aperture masking interferometry (SAM) and H_α differential imaging (LkCa 15 bcd; Kraus and Ireland 2012; Sallum et al. 2015). However, later direct imaging observations showed that the SAM detections correspond to disk features (Currie et al. 2019): LkCa 15 b technically remains a candidate for now due to its single epoch H_α detection (though see Mendigutía et al. 2018). Other claimed protoplanet detections have been revealed to likely be misidentified disk signals instead of planets (e.g. Rich et al. 2019).

3.4. Challenges with Interpreting Detections

3.4.1. Confirming Companionship

Direct imaging observations reveal many point sources that are unrelated background stars instead of bound companions, especially for systems in the Galactic plane (e.g. Galicher et al. 2016). Confirming candidate planets as bound – i.e. sharing common proper motion with and orbiting their stars – often requires multi-year observations, depending on the star’s proper motion. In some pathological cases, background stars can have a non-zero proper motion and thus are more easily confused with bona fide planets (e.g. Nielsen et al. 2017). In the absence of full confirmation, an object’s near-IR spectrum can provide strong evidence that it is a directly-imaged exoplanet (e.g. for 51 Eri b; Macintosh et al. 2015).

3.4.2. Estimating Accurate Masses

Masses for imaged planets and planet candidates are typically not directly measured but are instead estimated using luminosity evolution models that map between an object’s brightness and mass as a function of age. Accurate mass estimates therefore are affected by uncertainties in these models and require precise system ages. *Hot start* models for planet luminosity evolution assume a high initial entropy, resulting in bright planets for the first 1–100 Myr (Baraffe et al. 2002; Burrows et al. 2001, 2003). *Cold start* models assume a low initial entropy, resulting in planets that are substantially fainter for the first 100 Myr (Marley et al. 2007). Originally, hot start models were used to describe planets formed by disk instability, while cold start models described planets formed by core accretion (Marley et al. 2007)¹. However, recent models show that core accretion-formed planets can be compatible with hot start-like luminosity evolutions, and jovian planets may form with a range of initial entropies (Mordasini et al. 2017; Berardo et al. 2017; Spiegel and Burrows 2012). Aside from 51 Eri b, all planets imaged thus far are only consistent with a hot-start luminosity evolution.

Precise ages can be exceptionally challenging to derive for isolated stars (e.g. Soderblom et al. 2014). Members of young moving groups or other nearby associations can be age-dated using a variety of methods: e.g. fitting group Hertzsprung-Russell (HR) diagram positions with stellar evolutionary models, Lithium abundances. Thus, moving group or association membership can yield a star’s age. However, even stars with a motion similar to bona fide moving group members could instead be interlopers, especially if they have dissimilar space positions. For isolated Sun-like stars, stellar rotation and activity can give age estimates, albeit with significant scatter (Barnes 2007; Delorme et al. 2011; Angus et al. 2019). For early-type stars, HR diagram positions have provided approximate ages: optical interferometry can now provide more precise estimates by

¹ See Section 6.4 for definitions of the core accretion and disk gravitational instability formation pathways

resolving the stars themselves (e.g. [Jones et al. 2016](#)).

Revisions in the stellar age often affects the interpretation of an imaged companion. For example, based on the primary’s claimed membership in the Columba association, κ And b was originally thought to be 12–13 M_J ([Carson et al. 2013](#)). In contrast, the primary’s HR diagram position resembles an older system (220 Myr), which would imply the companion is $\sim 50 M_J$ ([Hinkley et al. 2013](#)). However, through optical interferometry, [Jones et al. \(2016\)](#) showed that the star is likely (nearly) coeval with Columba even if it is not a member (~ 47 Myr), implying the object is a planet-mass companion. Later, near-IR spectra of κ And b were found to be consistent with a planet interpretation ([Currie et al. 2018](#)). In contrast, the imaged companion to GJ 504 was announced as a 3–8.5 M_J planet with an age of 100–510 Myr ([Kuzuhara et al. 2013](#)). Based on interferometric, RV, and high contrast imaging data, [Bonney et al. \(2018\)](#) derived a mass range of 1–23 M_J , while other analysis of the star suggested an age of about 2.5 Gyr and a mass well into the brown dwarf regime ([D’Orazi et al. 2017](#)).

3.4.3. Planet or disk feature?

Distinguishing between highly-structured disk signals and bona fide protoplanets is a steep, chronic challenge. Advanced algorithms needed to detect protoplanets can attenuate both disk and planet signals: forward-modeling is required to ensure that a claimed planet detection is not a partially subtracted piece of the disk ([Currie et al. 2017](#)). For systems with hot dust ($T \sim 1000$ – 2000 K) near the star that intercepts and reprocesses emission, the disk’s scattered light spectrum may strongly resemble spectra of bona fide protoplanets ([Mulders et al. 2013](#)). Orbital motion over multi-year timescales can better establish that a signal is an orbiting planet and not a static disk feature ([Keppler et al. 2018](#)). H_α emission can also pinpoint actively accreting protoplanets ([Haffert et al. 2019](#)); however, accretion onto protoplanets embedded in disks may be unidentifiable, since optical extinction likely renders H_α undetectable.

Fomalhaut b may represent the first of yet another class of objects with a challenging interpretation ([Kalas et al. 2008](#)). The object was initially identified as a directly imaged planet, made visible by both reflected light from a circumplanetary disk and thermal emission, and responsible for sculpting the star’s Kuiper belt-like debris disk. However, later analysis showed that Fomalhaut b’s spectrum is completely explained by scattered starlight and its orbit likely crosses the ring ([Janson et al. 2012](#); [Currie et al. 2012b](#); [Galicher et al. 2013](#); [Kalas et al. 2013](#)): the object is lower in mass and likely made visible purely by circumplanetary dust. Recently, from analyzing archival and unpublished data, [Gaspar and Rieke \(2020\)](#) proposed that Fomalhaut b may be fading and dispersing, consistent with a massive planetesimal collision. Other analyses find no clear evidence for these two trends ([Currie et al. 2012b](#)), although they were conducted only over a subset of available data. Future observations of Fomalhaut b and/or reanalyses

of recent data may clarify its true nature.

3.5. Synergies with Other Techniques

The limitations of direct imaging affect our ability to interpret data for individual objects and to draw conclusions from large-scale population studies. For individual objects, mass estimates depend on both the age of the planet and the chosen luminosity evolutionary model (see Section 3.4). At a population level, the angular resolution of the telescope and the achievable contrast of the instrument limit the range of detectable planetary masses and semi-major axes with direct imaging. Combining direct imaging with other planet detection techniques partially mitigates these limits.

Optical interferometry provides a means to directly detect bright, modest planets at small angular separations. As a prime example, GRAVITY interferometer coherently combines the light of all four VLT telescopes, yielding the equivalent angular resolution of a 130-m telescope ([GRAVITY Collaboration et al. 2017](#)). While the GRAVITY field-of-view is small (~ 50 mas), indirect detection techniques (e.g. RV) can help predict the position of an exoplanet candidate (e.g. [Nowak et al. 2020](#)). GRAVITY has yielded exceptionally high-SNR spectra and ultra-precise astrometry of known planets ([Gravity Collaboration et al. 2019](#)); the combination of GRAVITY and indirect techniques have now resulted in new planet discoveries ([Hinkley et al. 2022a](#)).

Relative astrometric measurements of a planet around its host star cannot alone be used to precisely measure the mass of the orbiting planet; the semi-major axis of the relative orbit encodes the system’s total mass, not the individual components’ masses. The system’s mass ratio, and thus the mass of the planet, can be measured if the semi-major axis of the orbit of the star around the system barycenter is known. This orbit can be measured either using absolute astrometric measurements from catalogues such as *Hipparcos* and *Gaia*, or spectroscopic observations to measure the Doppler shift of the star’s spectral lines over the course of the orbit. In some cases, high-resolution spectroscopy can measure the Doppler shift of the planet’s spectral lines ([Snellen et al. 2014](#); [Wang et al. 2021](#)), also yielding the mass ratio. Combining the star’s orbit around the barycenter with the relative astrometry between star and planet yields the mass ratio, and a dynamical mass for the planet. In multi-planet systems with high-precision astrometry, the the planets’ mutual gravitation can be detected by fitting for deviations from Keplerian motion, yielding their mass estimates ([Lacour et al. 2021](#)).

The β Pic system is the current benchmark example of combining planet detection techniques to measure model-independent masses. Relative astrometry of β Pic b and c combined with the star’s astrometric and RV measurements provides dynamical masses for the planets ([Snellen and Brown 2018](#); [Lagrange et al. 2019](#); [Dupuy et al. 2019](#)). Measurements of non-Keplerian motion due to the mutual gravity of β Pic b and c are also now possible given the

precision of recent interferometric monitoring campaigns (Nowak et al. 2020).

Combining astrometry and/or RV and direct imaging data can yield dynamical masses for other directly-imaged planets, as well as for numerous brown dwarf companions (Grandjean et al. 2019; Brandt et al. 2020, 2021b). The upcoming *Gaia* data releases for the full and extended mission will be used extensively in future detection and characterization studies of directly-imaged planets, yielding further dynamical masses for directly imaged companions. The extended mission will provide precision astrometric measurements of the host star over ≈ 10 years.

Combining direct imaging with other detection techniques can improve planet occurrence rate measurements and can better determine the planet frequency distribution over a range of masses, orbital periods, and host star properties. Long-term Doppler surveys are largely complete to giant planets within ~ 5 au, and partially complete to giant planets out to ~ 10 au, the current inner limit of sensitivity of direct imaging surveys. Thus, combining results from both techniques reveals giant planet demographics out to ~ 100 au (Section 6.3). RV studies of young stars (e.g. Lagrange et al. 2019; Grandjean et al. 2021) allow occurrence rates to be compared for stars of similar ages, tracing the extent of giant planet migration over system lifetimes and its effect on planet frequency. The final *Gaia* planet catalog (Perryman et al. 2014) will also help place demographic measurements of young, wide-separation giant planets into context, as astrometry will be better able to probe intermediate separation giant planets (~ 1 -10 au, $\gtrsim 1 M_{Jup}$) around younger, higher-mass stars compared to RV. These target stars more closely match the hosts of imaged planets. A *Gaia*-selected survey of accelerating stars has now led to the first joint direct imaging and astrometry discovery of an exoplanet (Currie et al. 2022a). Combining *Gaia* observations of younger, higher-mass stars with direct imaging will illuminate trends in occurrence rate as a function of stellar mass and age.

Direct imaging also shares an important overlap with planet detection by microlensing. Both techniques are sensitive to planets beyond the snow line, with microlensing probing lower planet-star mass ratios (e.g. Suzuki et al. 2016), while the host mass of imaged planets can be directly determined, and the planet mass inferred from models. In addition, singly lensed short-period microlensing events can represent either a free-floating planet or a wide-separation bound planet (Sumi et al. 2011). Constraints on the wide-separation giant planet population can be determined from imaging, thus more definitively constraining the free-floating planet occurrence rate.

4. Atmospheric Characterization of Directly Imaged Exoplanets

Direct imaging enables characterization of young (age < 200 Myr) jovian exoplanets at wider separations with negligible irradiation compared to most transiting planets. In

this section, we first summarize from an empirical standpoint what we have learned about the atmospheres of the current cohort of young directly imaged giant planets from their photometry and spectroscopy. We then consider the theoretical side of the picture, in particular, the state-of-the-art in how we model these complex, cool atmospheres.

4.1. Empirical Constraints from Time-Averaged Observations

4.1.1. Photometry

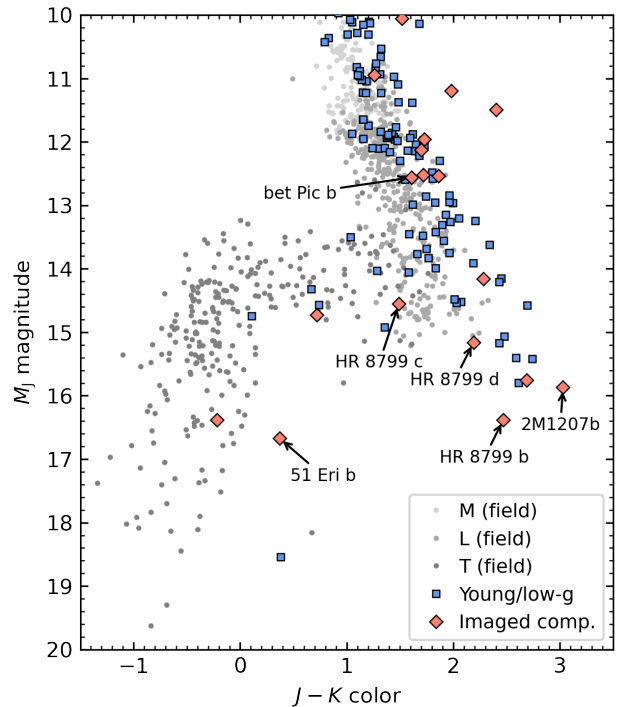


Fig. 8.— Near-infrared color-magnitude diagram of field M, L and T-dwarfs (gray circles), isolated objects exhibiting evidence of youth or possessing low surface gravity (blue squares), and directly imaged substellar/planetary-mass companions to stars and brown dwarfs (red diamonds). We annotate selected imaged exoplanets/planet-mass companions. Young, low-gravity objects form a sequence displaced redward from that of older, higher-gravity field objects. Data obtained from the UltracoolSheet.

Photometry in the major near-to-mid IR passbands – J , H , K , L_p , M_s – covers the bulk of emission for young superjovian planets and provided the first empirical diagnostic of young, directly-imaged planet atmospheric properties. Figure 8 displays a typical near-IR color-magnitude diagram for selected directly-imaged planets and other planet-mass companions compared to older, more massive field brown dwarfs and younger brown dwarfs whose ages and masses partially overlap with those of most imaged planets. Imaged planets and planet-mass companions span the full luminosity range characteristic of mature late-M, L, and T field brown dwarfs (vertical axis). However, young brown dwarfs, planets, and planet-mass companions typically have redder colors than field objects.

The most pronounced differences between planet and

field brown dwarf photometry occur near the transition from methane-poor L-type dwarfs to methane-absorbing T-type dwarfs. The first imaged planet-mass companion – 2M 1207 B – and some of the first imaged exoplanets (e.g. HR 8799 b) are particularly discrepant, appearing to populate a previously empty part of these diagrams consistent with a reddened extension of the L dwarf sequence to lower luminosities (Chauvin et al. 2004; Marois et al. 2008a; Currie et al. 2011; Barman et al. 2011a). Over the full 1–5 μm spectral range, photometry for these objects appears redder and more blackbody-like (Figure 10, top-left). More recent studies show that a number of other young imaged planets/planet-mass companions – e.g. HD 95086 b, TYC 8998-760-1 c, HD 206893 b, 2M 2236+4751 B – also populate this region (e.g. Rameau et al. 2013b; Bohn et al. 2021; Delorme et al. 2017a; Bowler et al. 2017).

Differences between field and young objects with T spectral types are less clear. Few young, T-type planet-mass companions have been identified in the last decade: e.g. 51 Eri b (Macintosh et al. 2015), GU Psc B (Naud et al. 2014). While GU Psc B follows the sequence of field brown dwarfs in near-IR color-magnitude diagrams, the exoplanet 51 Eri b is redder than field brown dwarfs. Four additional companions orbiting primary stars with intermediate ages (≤ 1 Gyr; HN Peg B, ROSS458C, BD204-39B, Coconuts-2b, Luhman et al. 2007; Goldman et al. 2010; Zhang et al. 2021c) show similar but less pronounced deviations with respect to field dwarfs in the same luminosity range. Some directly-imaged L/T transition planets and planet-mass companions have color-magnitude diagram positions discrepant from field objects in thermal IR passbands probing methane absorption (3.3 μm , M_s) but have positions similar to field objects in other passbands (e.g. L_p , 4.05 μm) (Skemer et al. 2012, 2014a; Currie et al. 2014a).

4.1.2. Spectroscopy

Over the past decade, IFS instruments, especially those used in combination with extreme AO systems (P1640, SPHERE, GPI, SCEXAO-CHARIS) have provided critical low-resolution ($R \sim 20$ to 80) near-IR (1–2.5 μm) spectra of most directly-imaged exoplanets, a representative sample of which is displayed in Figure 9. Near-IR spectra provide key diagnostics of brown dwarf and planet atmospheres. Spectral indices derived from low-resolution data like H_2O yield coarse estimates of spectral types (Allers and Liu 2013). The H -band continuum index and (possibly) the H_2 -K index is a diagnostic of surface gravity (Allers and Liu 2013; Canty et al. 2013).

Following trends from photometry, the spectra of young directly-imaged planets and other planet-mass companions show significant differences with the spectra of field brown dwarfs. Among the most notable are the following:

- **Chemistry** – The L/T transition traces the onset of methane absorption. However, spectra of some L/T transition exoplanets and planet-mass companions – e.g. the HR 8799 planets, 2M 1207 B – show a

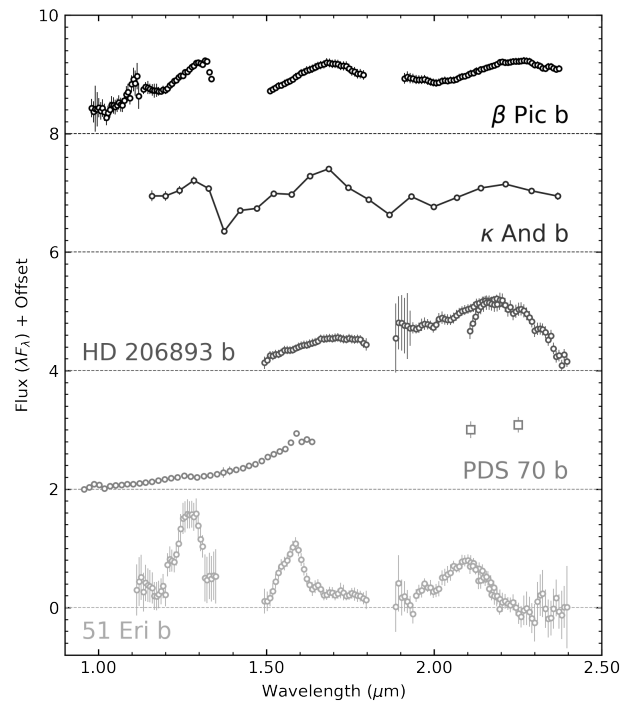


Fig. 9.— Near-infrared spectra of imaged exoplanets obtained using low-resolution integral-field spectroscopy: from top-to-bottom, β Pic b (Chilcote et al. 2017), κ And b from Subaru/CHARIS taken in a lower-resolution single-shot mode (Currie et al. 2018), HD 206893 b (Ward-Duong et al. 2021), PDS 70b from VLT/SPHERE (Mesa et al. 2019), and 51 Eri b (Rajan et al. 2017) from Gemini/GPI. The spectra are normalized by the flux between 2.05–2.15 μm (1.6 μm for 51 Eri b for clarity). Dashed lines indicate the offset applied to each spectrum.

lack of methane absorption compared to field dwarfs with similar temperatures and CMD positions (Barman et al. 2011a,b; Bonnefoy et al. 2016; Greenbaum et al. 2018). Thermal IR spectra confirm that the HR 8799 planets also have weaker absorption in the 3.3 μm methane filter (Doelman et al. 2022).

- **Gravity** – The H -band spectra for L dwarf and L/T transition directly imaged exoplanets / planetary-mass objects such as HR 8799 b, κ And b, ROXs 42Bb show highly peaked H -band spectra and/or red K -band spectra compared to field dwarfs (Lucas et al. 2001; Barman et al. 2011a; Currie et al. 2018, 2014b; Bowler et al. 2014; Allers and Liu 2013; Liu et al. 2013; Gauza et al. 2015). The H and K -band shapes probe collisionally-induced absorption (CIA) of hydrogen; lower gravities result in weaker CIA and thus peaked H -band peaks and redder K -band slopes.
- **Dust** – At least some of the HR 8799 planets have spectral properties and molecular absorptions that are well matched by those of young free-floating objects at the L-T transition (see also Section 4.3). However, no object yet reproduces the available 1–2.5 μm spectra of HR8799b, which may be due to the lack

of identified young free-floating T-type objects. A handful of early-T-type objects such as the AB Doradus member 2MASS J13243553+6358281 (*Gagné et al. 2018a*) (see Section 4.1.1) can reproduce the spectral bands of HR 8799 b provided that an extra layer of extinction by sub-micron dust particles is applied to these empirical template spectra to match the spectral slope of the planet (*Bonnefoy et al. 2016*). HD 206893 b presents an even more extreme example, with an even flatter, more blackbody-like spectrum yielding an extremely red spectrum from 1 to 2.5 μm , likely due to substantial atmospheric dust (*Milli et al. 2017*; *Delorme et al. 2017b*; *Ward-Duong et al. 2021*).

Spectra of the coolest and lowest mass imaged exoplanet known to date (51 Eri b) display a clear and so-far unique detection of a methane absorption at 1.6 μm in the spectrum of an imaged exoplanet (*Macintosh et al. 2015*; *Rajan et al. 2017*), coincident with an enhancement in the K-band flux. Similar K-band flux enhancements have already been noted in young mid- to late-T dwarfs but the enhancement is particularly extreme in the case of 51 Eri b and is due to the reduced collision induced absorption of H₂ (*Borysow et al. 1997*) in 51 Eri b’s lower-pressure atmosphere.

Protoplanets display far more featureless, blackbody-like spectra. PDS 70 bc’s spectra reveal an extremely red spectral continuum devoid of the strong water-band feature (1.3-1.4 μm) expected given the observed luminosity of the planets (*Müller et al. 2018*; *Mesa et al. 2019*). Higher-resolution K-band spectra show a lack of molecular absorption in PDS 70 b’s spectrum (*Cugno et al. 2021*). The circumplanetary disks and/or cocoon surrounding each planets (see Fig 7 and *Christiaens et al. 2019*; *Benisty et al. 2021*) produce significant foreground extinction (e.g., *Hashimoto et al. 2020*) and may produce spectroscopic properties similar to what is seen in the near-infrared spectra of enshrouded class I protostars (e.g. *Connelley and Greene 2010*). The near-IR spectrum of AB Aur b is reproduced by a 2000-2500 K blackbody but likewise lacks clear evidence for molecular absorption common in fully-formed substellar objects with similar temperatures (*Currie et al. 2022b*).

Aside from a few isolated cases (e.g. HR 8799 bcde), the spectroscopic properties of imaged exoplanets are more poorly constrained at wavelengths longward of 2.5 μm . The 3-5 μm range is particularly interesting since it contains both methane and ¹²CO absorption features diagnostic of carbon chemistry (CO-CH₄) and cloud structures (e.g. *Miles et al. 2018, 2020*). The L_p-band spectra of hotter young M7 to L3 companions presented in *Stone et al. (2016)* show no significant difference with those of field dwarf counterparts. The L_p spectrum of κ And b is well matched with that of young, nearby free-floating brown dwarfs (*Stone et al. 2020*). A few free-floating planet analogues have high-quality 3-14.5 μm IRTF, AKARI, and Spitzer spectra (*Cushing et al. 2008*; *Sorahana and Yamamura 2012*). Analysis of these data would benefit from an

improved knowledge of the age and nature of these objects.

While most spectra for directly imaged planets to date has been at resolution $R < 100$, higher-resolution spectra are yielding promising results. Near-IR IFS instruments at medium resolving powers ($R=2000-6000$) fed by standard adaptive-optics modules are available on multiple 8-m class telescopes (e.g. Gemini/NIFS, VLT/MUSE and SINFONI, Keck/OSIRIS). Medium-resolution IFS data enables innovative strategies for evaluating and subtracting the stellar halo with the spatial diversity (e.g., *Thatte et al. 2007*; *Seifahrt et al. 2007*; *Wilcomb et al. 2020*). Most current medium resolution spectroscopic results are for young late-M and early-L young companions straddling the deuterium-burning boundary at $\rho > 0.5$ ” (e.g., *McElwain et al. 2007*; *Schmidt et al. 2008*; *Patience et al. 2010*; *Bowler et al. 2011*; *Bonnefoy et al. 2014a*; *Daemgen et al. 2017*; *Wilcomb et al. 2020*). However, ADI observations on these instruments (*Lavigne et al. 2009*; *Barman et al. 2011a*; *Meshkat et al. 2015*) and improved data reduction strategies have recently allowed the extraction of high quality medium-resolution spectra of emblematic exoplanets HR8799 bc and HIP65426 b (*Konopacky et al. 2013*; *Barman et al. 2015*; *Petrus et al. 2021*) deeply buried in the speckle noise. The planets’ spectra show fainter and narrower molecular bands (FeH, CO) and atomic lines (Na I, K I), sensitive to the surface gravity and primordial composition of the objects (C/O ratio, metallicity). They also reveal emission lines ($H_{\alpha}/0.656\mu\text{m}$, $P_{\alpha\beta}/1.282\mu\text{m}$, $Br_{\gamma}/2.166\mu\text{m}$) that trace active accretion (e.g., *Haffert et al. 2019*; *Bonnefoy et al. 2014a*; *Zhang et al. 2021a*) and that can be used both for characterizing the accretion processes (e.g., *Aoyama and Ikoma 2019*; *Thanathibodee et al. 2019*) and detecting new planets (*Uyama et al. 2017*; *Haffert et al. 2019*).

Novel data processing techniques such as “molecular mapping”, in combination with medium-resolution spectra, can also partly deblend the many ro-vibrational lines contained in planet spectra, which form the broad absorption bands observed at lower resolution (GPI, SPHERE). These molecular patterns can be extricated by cross-correlating a template spectrum to the planet spectrum in order to reveal faint molecular signatures (*Konopacky et al. 2013*; *Zhang et al. 2021a*). “Molecular mapping”, applied to each individual spaxel of an IFS datacube can simultaneously (i) detect exoplanets whose continuum emission would have been blurred by the speckle noise and residual stray light introduced by the instrument optics, (ii) characterize unambiguously their molecular content, and (iii) measure their Keplerian velocity (*Hoeijmakers et al. 2018*; *Petit dit de la Roche et al. 2018*; *Petrus et al. 2020*; *Cugno et al. 2021*). This method, as well as other supervised and non-supervised data processing techniques (*Ruffio et al. 2019*; *Rameau et al. 2021*) applied on such IFS data will critically boost the detection and characterization capabilities on the next generation of IFS operating on the 8-m class telescopes (GTC-FRIDA, VLT/ERIS, VLT/SPHERE+ and GPI 2.0) and the ELTs (e.g., *Houllé et al. 2021*).

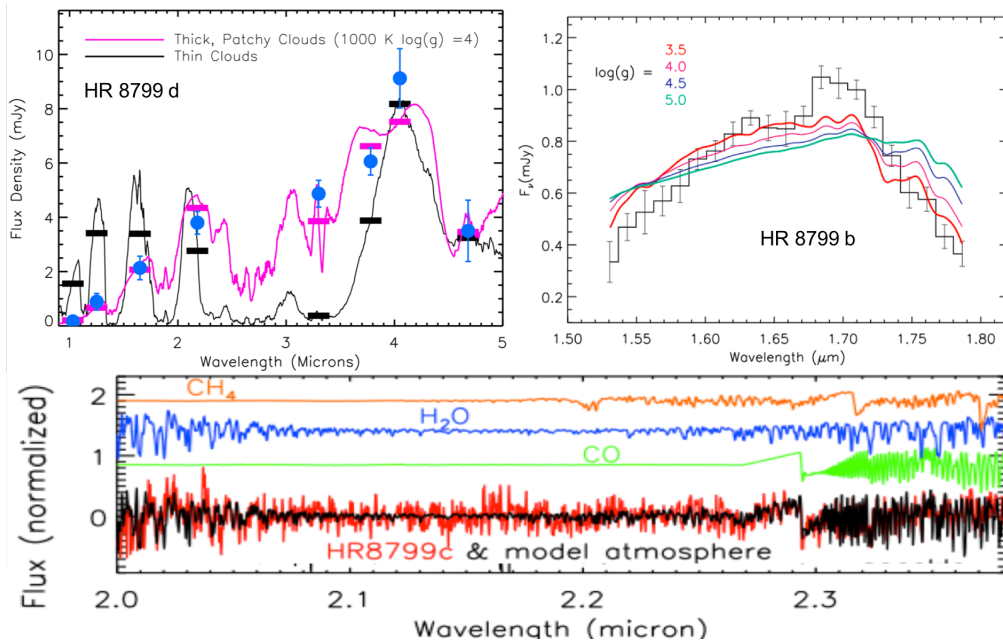


Fig. 10.— Demonstration of key properties inferred from direct imaging observations. (top-left) Fit to HR 8799 d 1–5 μm photometry showing that models with thick clouds better reproduce the planet data (adapted from [Currie et al. 2011](#)). (top-right) Keck/OSIRIS low-resolution H-band spectrum for HR 8799 b: a sharply-peaked H band spectrum is a signpost of low surface gravity ([Barman et al. 2011a](#)). (bottom) Keck/OSIRIS medium-resolution HR 8799 c spectrum, revealing lines of CO and H_2O ([Konopacky et al. 2013](#)).

High-resolution echelle spectroscopy ($R \geq 20,000$) will go further to resolve individual molecular lines and atomic line profiles and provide a measurement of the objects’ rotational broadening ($v \sin(i)$). High SNR spectra have been collected on a few young late-M and early-L companions ([McLean et al. 2007](#); [Rice et al. 2010](#)) and free-floating analogues, but these observations usually require significant telescope time. Cross-correlating lower SNR companion spectra or spectral residuals with templates can access the companion’s Keplerian and rotational velocities, check for specific molecular signatures, and disentangle companions from the dominant speckle noise produced by the host star. This technique is being used on a steadily increasing number of companions ([Snellen et al. 2014](#); [Schwarz et al. 2016](#); [Wang et al. 2018](#); [Bryan et al. 2020a](#); [Xuan et al. 2020](#); [Wang et al. 2021](#)) and is a promising method for identifying closer-in and fainter exoplanets (Section 7).

4.2. Inferred Theoretical Properties from Time-Averaged Observations

The empirical comparisons described in the previous two sections, combined with atmospheric models spanning a wide parameter space in temperature, gravity, clouds, and chemistry, provide novel constraints on the atmospheric properties of directly-imaged exoplanets.

Figure 10 summarizes our current understanding of the key atmospheric properties of young, directly imaged giant planets. Young exoplanets likely are dustier and have thicker clouds than field brown dwarfs of the same effective temperatures (top-left panel) ([Currie et al. 2011](#); [Barman et al. 2011a](#); [Bonnefoy et al. 2016](#)). For a fixed observed effective temperature, thicker clouds translate into

hotter temperature profiles, meaning that the temperature is higher at a given atmospheric pressure. The $\tau = 1$ surface is more uniform with wavelength, resulting in a flatter, more blackbody-like spectrum (magenta line) compared to models with thinner clouds (black line). This effect is most pronounced at the L/T transition – e.g. for planets like HR 8799 bcde. The redder colors of many L-type exoplanets are likely explained by clouds (e.g. [Currie et al. 2013](#)); the redder color of 51 Eri b may also be due to at least partial cloudiness ([Rajan et al. 2017](#)). Planets and planet-mass companions at the L/T transition also show evidence for non-equilibrium carbon chemistry, producing a lack of methane absorption in K band, flat spectra at 3–4 μm and weak emission at 5 μm ([Galicher et al. 2011](#); [Konopacky et al. 2013](#); [Skemer et al. 2014a](#)).

Both clouds and chemistry are strongly influenced by surface gravity ([Marley et al. 2012](#)). Lower gravities yield pressure-temperature profiles more characteristic of hotter dwarfs and move the depth at which carbon-based chemical reactions are quenched deep in the atmosphere, leading to an elevated abundance of CO ([Barman et al. 2011a](#); [Marley et al. 2012](#)). In the coming years, more directly-imaged planet detections spanning a wider range of mass, age, and temperature will better clarify how the clouds, chemistry, and gravity of young jovian planets evolve (see Section 7).

4.3. Time-Resolved Atmospheric Properties: Rotation Measurements and Variability

The photometric and spectroscopic observations described in the previous two sections are time-averages – observations either capturing short, 1-2 hour snapshots or averaging over multiple observations covering different

rotational phases. However, directly imaged exoplanets, like their higher-mass brown dwarf cousins, are dynamic, rapidly rotating objects. Measuring spectral line broadening ($v \sin(i)$) for field brown dwarfs and monitoring their photometric variability reveals rotation periods of ~ 3 -20 hours (Zapatero Osorio et al. 2006). Recently, Tannock et al. (2021) have even found 3 brown dwarfs with rotation periods as short as ~ 1 hour! Rotation measurements are scarcer for directly imaged exoplanets and their analogues, but current measurements suggest that directly imaged exoplanets are also fast rotators. Spectral-line broadening measurements of β Pic b indicate a rotation period of 7-9 hours, Snellen et al. (2014). Rotational periods derived for 27 planetary mass objects (both as companions and free-floating) from the compilation of Bryan et al. (2020a) range from 4 to 22 hours.

If an object is a rapid rotator and also has asymmetric top-of-atmosphere structure (e.g. patchy thin and thick clouds), it will display significant variability, appearing considerably brighter at some rotational phases than others. Large variability surveys of brown dwarfs find variability is common (Radigan et al. 2014; Wilson et al. 2014; Radigan 2014; Metchev et al. 2015). Variability amplitudes extend up to $\sim 20\%$ in the near-IR. Young directly imaged giant planets are likely to be even more variable. From a survey of 30 young, low-surface gravity brown dwarfs with estimated masses $< 25 M_J$ (e.g., free-floating analogues to directly imaged exoplanets), Vos et al. (2019) find that 30% of low surface-gravity L0-L7.5 dwarfs are variable, compared to 3% of field L dwarfs. Exoplanet analogues with L6-L7 spectral types appear to be particularly variable, with peak-to-trough amplitudes $> 5\%$ in a number of notable cases (Biller et al. 2015; Lew et al. 2016; Vos et al. 2018; Biller et al. 2018; Bowler et al. 2020b; Zhou et al. 2020, 2022). These objects have spectra that are nearly identical to those of the archetypical HR 8799 planets (Bonnetfoy et al. 2016); thus, their variability properties are likely similar to those of these bonafide exoplanet companions. Young, planetary mass T dwarfs are likely more variable than their old, field counterparts as well. Two out of the three highest amplitude T dwarf variables known, specifically SIMP 0136 and 2M2139, have recently been confirmed as planetary-mass members of the Carina Near association (Gagné et al. 2017; Zhang et al. 2021b).

Variability studies, especially spectroscopic variability studies, are valuable probes of the top-of-atmosphere structure (TOA) of brown dwarfs and directly imaged exoplanets. A unique map cannot be obtained from lightcurve monitoring. However, indicative maps can be generated from the spectral mapping technique, which uses Markov-Chain Monte Carlo techniques to fit elliptical spots (Kostov and Apai 2013; Karalidi et al. 2015, 2016) and/or planetary-scale waves (a sinusoidal bright-dark pattern confined to a single latitudinal band, Apai et al. 2017) to multi-wavelength lightcurves. Quickly changing features on several field brown dwarfs may indicate that the beating between multiple planetary-scale waves better describes the

lightcurves observed for field brown dwarfs than elliptical, starspot-like spots (Apai et al. 2017, 2021).

Different wavelengths also probe different depths in brown dwarf and giant exoplanet atmospheres. Mid-IR data probe higher-up, cooler cloudtops; the near-IR probes deeper into cloud decks (e.g. Manjavacas et al. 2021). Notably, TOA structure appears to vary in between this level, seen as phase shifts between the near-IR and mid-IR in the substellar object lightcurves, where successive maxima / minima in near-IR are offset in time relative to their mid-IR counterparts. Such phase shifts have been observed in several brown dwarfs (Yang et al. 2016) and in at least one free-floating planetary mass object (Biller et al. 2018).

The studies described in the preceding paragraph have mostly targeted higher mass field brown dwarfs. Next generation telescopes and instruments such as JWST will enable similar studies for free-floating planetary mass objects and bright exoplanet companions such as β Pic b and HR 8799 bcde. Giant exoplanet companions are likely to be equally variable compared to highly variable free-floating planetary mass objects, but are much more difficult targets for variability studies, given the technical challenges of obtaining high-fidelity, highly-stable spectrophotometry for close companions. Two studies have attempted variability monitoring for the HR 8799 planets using VLT-SPHERE (Apai et al. 2016; Biller et al. 2021), reaching sensitivity to variability with amplitudes down to 5% for periods < 10 hours, but not yielding any detections to date.

4.4. State-of-the-Art Modeling of Imaged Exoplanets

4.4.1. Recent developments of 1D models

Atmospheric models for directly imaged exoplanets and brown dwarfs share a heritage with models for very low mass stars (Chabrier et al. 2000; Baraffe et al. 2002; Burrows et al. 2003; Allard et al. 2012; Baraffe et al. 2015) and solar system planets, building a self-consistent, one-dimensional atmospheric structure connecting a fully convective interior with a radiative atmosphere (“radiative-convective” model, see review by Marley and Robinson 2015). However, the cooler temperatures and lack of core H fusion for brown dwarf and exoplanet atmospheres require a number of different “ingredients” compared to stars, most specifically, a treatment of clouds and hazes in these atmospheres and the ability to handle disequilibrium chemistry and vertical mixing.

The very red colors observed for young planet-mass objects cannot be described by simple 1D models without additional cloud or convection prescriptions (Marley et al. 2012). The most common parameterization used in modeling brown dwarf and giant exoplanet clouds utilizes a sedimentation efficiency parameter f_{sed} , which tunes cloud particle sizes necessary to balance vertical transport of condensable gases (e.g. the Eddysed grid presented in Ackerman and Marley 2001). The Sonora model grid is an update to the original Eddysed grid models, reaching cooler effective temperatures and a wider range of C/O values than the

earlier grids. To date, only the cloudless model grid is available (Marley et al. 2021), but grids incorporating a similar f_{sed} cloud parameterization should be available soon. The ATMO 2020 models (Phillips et al. 2020) also provide a key update to earlier grids, in particular, the COND and DUSTY models of Baraffe et al. (2002), incorporating a new H-He equation of state, updated molecular opacity, and an improved treatment of the collisionally broadened potassium resonance doublet. Finally, models like Exo-REM introduce a self-consistent cloud model, with cloudy and clear columns, a similar f_{sed} method of cloud parameterization (Charnay et al. 2018), and grids that consider non-solar compositions (Nowak et al. 2020).

Canonical models utilize silicate dust clouds to describe young exoplanet atmospheres, especially at the L/T transition. However, other work explores alternatives. For example, Tremblin et al. (2016) propose that a thermo-chemical instability producing an extra source of diabatic convection can alter an atmosphere’s temperature-pressure profile, providing another path to produce the observed red colors without clouds (see also: Tremblin et al. 2017, 2019, 2020).

4.4.2. Inversion techniques: achievements and challenges

The models discussed in Section 4.4.1 are full self-consistent radiative-convective equilibrium models: forward models where the full 1D structure of the modeled atmosphere is solved iteratively (similarly as with stellar models). These models produce grids of synthetic planet spectra exploring the impact of a limited set of model free-parameters. The comparison of these models to observed spectra is known as “forward modelling”.

Bayesian inference methods such as the Markov-Chain Monte-Carlo method or the Nested sampling algorithm can be coupled to precomputed grids of forward models to interpret spectra. The method can account for correlated and uncorrelated noise in the data and can estimate posterior probability distributions on the model parameters and evidence degeneracies between those parameters, thus identifying the sub-families of models that best represent the data (Rice et al. 2010; Samland et al. 2017; Stolker et al. 2020; Zhang et al. 2021d). Recently proposed random forest algorithms are a more computationally rapid alternative to the Bayesian framework and can provide information regarding the degree in which datapoints at given wavelengths constrain a specific free-parameter of the model (e.g., Oreshenko et al. 2020).

Modern self-consistent forward models track both the effect of cloud condensates on the sequestration of atomic species in the gas phase and the consequences of non-equilibrium carbon chemistry, if present. If not properly treated, the presence of clouds and non-equilibrium chemistry can lead to biased determination of bulk atmospheric compositions. Nonetheless, for self-consistent models that carefully take into account these processes, “forward modelling” can provide accurate fits to medium-resolution spectra of companions consisting of several thou-

sands of datapoints (see Figure 11). It however requires re-interpolating the grids of models and relies on a number of pre-determined sets of physical ingredients in the models.

The complementary “retrieval” approach starts from the spectra and works backwards. In this case, a parameterized pressure-temperature profile is adopted and other fundamental parameters (mass, effective temperature, cloud properties, abundances, etc.) are then retrieved given the observed spectrum by using Bayesian or random forest techniques (Madhusudhan and Seager 2009). Retrievals have been used extensively to interpret transiting exoplanet spectra (see Madhusudhan 2018, for a recent review). In the last few years, retrievals have also been applied to direct spectroscopy of brown dwarfs (Line et al. 2017; Burningham et al. 2017, 2021) and extrasolar giant planets (Lavie et al. 2017; Mollière et al. 2020). However, retrieval approaches lose clear physical interpretations of the spectra. This approach is still in its infancy and will gradually benefit from improvements made to forward models.

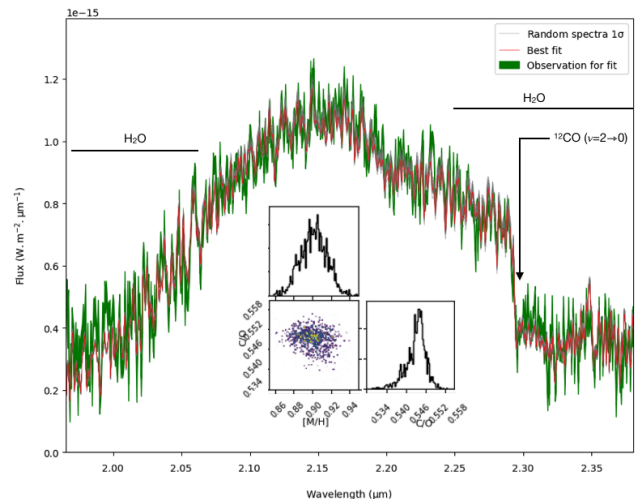


Fig. 11.— Keck/OSIRIS medium-resolution ($R \sim 4000$) K-band spectrum of HR8799 b from Barman et al. (2015) fitted with the Bayesian forward modeling code FORMoSA (Petrucci et al. 2020, 2021) and the most recent self-consistent 1D models Exo-REM (Charnay et al. 2018; Blain et al. 2021), exploring different abundance values (C/O, M/H). The fit provides a consistent representation of the spectral continuum and ^{12}CO absorption, confirms the solar C/O ratio of the planet inferred in Barman et al. (2015) from the same data, and matches well the C/O value measured for the primary star (Wang et al. 2020).

4.4.3. The need for 3D models

The majority of modeling approaches for directly imaged exoplanet atmospheres are one-dimensional. However, high-amplitude, quasi-periodic variability detected in both brown dwarfs and free-floating planetary mass objects indicate significant asymmetric top-of-atmosphere structure, often attributed to patchy thin and thick cloud cover (Apai et al. 2013). (See Section 4.3 for additional details on these observations.) Coupled with their relatively rapid rotation rates which likely drive significant winds, these are

dynamic and quickly varying atmospheres – and certainly not one-dimensional. Full 3D general circulation modeling (GCM) including a treatment of radiative transport is still on the horizon for brown dwarfs and directly imaged giant exoplanets, but a number of groups have implemented modeling approaches that take into account the significantly asymmetric top-of-atmosphere structure and strong atmospheric circulation of these objects. *Freitag et al. (2010)* use the CO5BOLD code to perform local, 2D radiation hydrodynamics simulations, incorporating dust clouds in the atmospheres of late M stars and brown dwarfs and finding that convectively excited gravity waves are an essential mixing process in these atmospheres. For very cool T and Y dwarf atmospheres with patchy salt and sulfide clouds, *Morley et al. (2014)* introduce both clear and cloudy columns in their models along with a cloud-covering fraction for each model atmosphere. *Showman and Kaspi (2013)* present three-dimensional, global, numerical simulations of convection in the interior of brown dwarfs and directly imaged giant planets. These authors consider how the temperature perturbations driven by this convection could drive top-of-atmosphere asymmetry, in particular, allowing patchy clouds to form near the photosphere of L-T transition brown dwarfs. *Zhang and Showman (2014)* use a shallow water model to model the atmospheric circulation driven by the rapid rotation of brown dwarfs and directly imaged giant planets. Depending on the strength of the heat flux and radiative dissipation, they find two circulation regimes: 1) with strong internal heat flux and weak radiative dissipation, banded east-west jets will spontaneously form and 2) with weak internal heat flux and/or strong radiative dissipation, vortices will instead form, potentially producing some of the “spotted” features found on brown dwarfs. To constrain the effect of latent heating due to condensation on both cloud growth and top-of-atmosphere asymmetric structure, *Tan and Showman (2017)* applied a idealized general circulation model (GCM) including a condensation cycle for silicate vapor. They found that simulations with conditions appropriate for T dwarfs developed both localized storms and east-west jets and that circulation driven by the latent heating due to the condensation of silicate clouds can generate large-scale cloud patchiness. In a series of recent papers, Tan and Showman have investigated a second possible driver of short-time evolution of clouds and thermal structures in brown dwarf, specifically, radiative cloud feedback, first within a 1D model (*Tan and Showman 2019*), then extending to a local 3D model (*Tan and Showman 2021a*), and finally extending to a full global geometry model (*Tan and Showman 2021b*).

4.5. Connecting atmospheric chemical abundances to exoplanet formation and migration histories

As seen in Sections 4.1.2 and 4.4.2, medium and high-resolution spectroscopy, coupled with state-of-the-art forward- and retrieval modeling approaches can measure atmospheric chemical abundances for exoplanets, in partic-

ular, key tracer ratios such as C/O and $^{12}\text{CO} / ^{13}\text{CO}$. The composition of a given planet-forming disk will vary as a function of radius, as various molecules (water, CO, CO₂) condense out into ices and form snow lines at progressively greater distances in the disk. Thus, an exoplanet atmosphere’s chemical composition will carry the imprint of where in the circumstellar disk it first formed and through which parts of the disk it migrated before reaching its final orbital configuration (e.g. *Öberg et al. 2011; Öberg and Wordsworth 2019; Madhusudhan 2019*). The nature of this imprint is challenging to describe end-to-end, from the protostellar cloud to the final observed exoplanet atmosphere. This requires a detailed understanding of the balance of which species remain in gas phase vs. which condense into solids, as well as the assumption that the final atmospheric gas composition of the planet will reflect the disk gas composition.

Öberg et al. (2011) made the first prediction for the atmospheric chemical signatures for different formation histories. For the canonical core accretion model, in which a several Earth-mass rocky core is built up by the accumulation of dust-to-boulder sized planetesimals and then accretes disk gas and residual planetesimals², jovian planets should have enhanced C/O~1 if they accrete most of their atmospheres from gas in the disk outside of the water snowline. Using high-resolution Keck-OSIRIS spectroscopy, *Konopacky et al. (2013)* measured a super-stellar C/O ratio for HR 8799 c, consistent with the *Öberg et al.* predictions for the core accretion scenario. Since this first measurement, C/O ratios have now been published for all four HR 8799 planets, β Pic b, HIP 65426 b, and κ And b (*Lavie et al. 2017; Mollière et al. 2020; Wilcomb et al. 2020; Wang et al. 2020; Gravity Collaboration et al. 2020; Petrus et al. 2021; Ruffio et al. 2021*). Discrepancies in values between early measurements and more recent measurements (e.g. between *Lavie et al. 2017; Wang et al. 2020*) likely occur because higher spectral resolution measurements yield more accurate C/O ratio measurements.

Interpreting C/O ratio measurements requires a careful comparison to disk/formation model predictions relative to different snowlines. To fully interpret C/O ratio measurements, several of the observational studies considered above also incorporate significant disk modeling in their analysis (cf. *Mollière et al. 2020; Gravity Collaboration et al. 2020; Petrus et al. 2021*). See *Madhusudhan (2019)* for a more detailed discussion.

A number of other elemental or isotopic ratios may yield insight into the formation mechanisms / locations of young, giant exoplanets. *Öberg and Wordsworth (2019)* suggest that the abundances of nitrogen-bearing species may also trace the formation location of a given planet in the disk (*Öberg and Wordsworth 2019*). The $^{12}\text{CO} / ^{13}\text{CO}$ ratio may also distinguish between “brown-dwarf” like and “planet-like” formation scenarios (*Zhang et al. 2021a,c*).

²Planet formation models are discussed extensively in Section 6.4.

5. Architectures of Directly Imaged Planetary Systems

5.1. Orbits and Dynamics

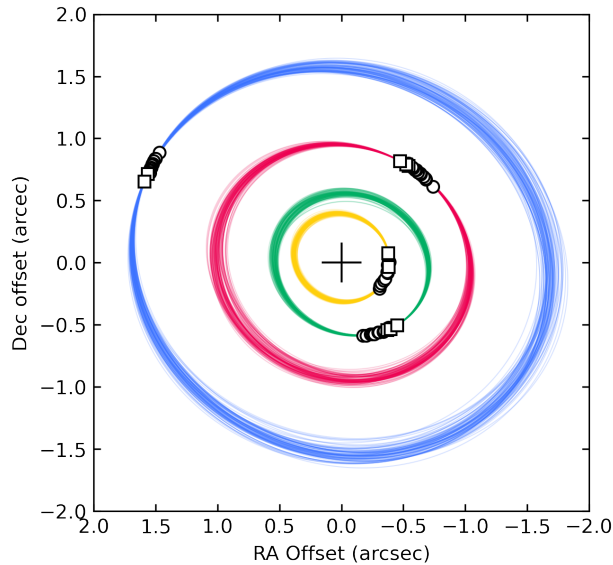


Fig. 12.— Visual orbits of the four planets in the HR 8799 system consistent with the astrometric measurements and assuming a dynamically stable co-planar configuration (Wang et al. 2018). These orbits are a small subset of all visual orbits, stable or otherwise, that are consistent with the data.

Given their long orbital periods, directly imaged planets are not currently amenable to rapid orbital characterization. At least one years’ worth of astrometric measurements are typically required in order to place initial constraints on the parameters of the visual orbits of planets that have been detected thus far (e.g., Pearce et al. 2015; Blunt et al. 2017). In fact, no planet yet discovered via direct imaging has a “closed” orbit, i.e. with relative astrometric measurements covering the full phase of the orbit. Despite the challenges associated with the analyses of these incomplete datasets, a great deal of information can still be learned regarding the orbits of imaged exoplanets, and the architectures of the planetary systems in which they reside.

The HR 8799 system is probably the best-studied system in terms of simulations of its dynamical configuration and long-term stability (Fabrycky and Murray-Clay 2010; Currie et al. 2011; Sudol and Haghighipour 2012; Goździewski and Migaszewski 2014; Göteborg et al. 2016; Goździewski and Migaszewski 2018; Wang et al. 2018; Zurlo et al. 2022). The four planets’ astrometric measurements are consistent with a co-planar configuration in, or close to, a 1:2:4:8 period ratio (Figure 12; Goździewski and Migaszewski 2018; Wang et al. 2018). Integrating the system forward (or backward) demonstrates that such a configuration is dynamically stable, at least for many multiples of the current age of the system (Goździewski and Migaszewski 2018). While a resonance between the four planets is not necessary for long-term stability, resonances between pairs of the inner planets are required if their masses are $\gtrsim 6M_{\text{Jup}}$ (Wang et al. 2018). In addition to testing the dynamical stability of the system, these simulations have also been used to investigate

the parameter space in which additional planets could exist in a stable configuration (Goździewski and Migaszewski 2018), either interior to the innermost known planet or in a wide orbit dynamically sculpting the outer debris disk (Booth et al. 2016; Read et al. 2018).

The dynamical stability of the other known multi-planet systems (β Pic, PDS 70, and TYC 8998) have not yet been studied at the same level of detail. Their astrometric measurements are consistent with a dynamically stable configuration given the masses derived from either evolutionary models (Wang et al. 2021; Bohn et al. 2020b), or from combined astrometric and radial velocity measurements (Lagrange et al. 2020; Brandt et al. 2021b). Continued monitoring of these systems is warranted to investigate not only their dynamical stability given revisions to their orbits and estimated masses, but also the influence of the planets on the structure of any resolved circumstellar material in each system (see Section 5.2).

Early astrometry of β Pic b quickly revealed a near-edge on orbit for the planet configuration (Lagrange et al. 2010), consistent with an edge-on inclination of the resolved debris disk (Smith and Terrile 1984). While geometrical arguments show that a long-period planet like β Pic b will likely not transit, a photometric event measured in 1981 showed a significant variation in the star’s brightness (Lecavelier Des Etangs et al. 1997), consistent with an eclipse of the star by the planet or its Hill sphere based on the ephemeris available at the time (Chauvin et al. 2012). Continued astrometric monitoring ruled out a planetary transit but demonstrated that the Hill sphere would transit the star in mid-to-late 2017 (Wang et al. 2016). An extensive photometric and spectroscopic campaign ensued to measure, or place stringent limits on, circumplanetary material as the Hill sphere transited. No significant event was detected: the 1981 event was probably not linked to the transit of an extended circumplanetary disk (Mol Lous et al. 2018; van Sluijs et al. 2019; Kenworthy et al. 2021). Despite this null detection, exo-cometary material not within the β Pic b Hill sphere has been detected transiting the star with TESS (Zieba et al. 2019, Lecavelier et al 2022 in press), suggesting that the earlier photometric variability could also be due to material not associated with the planet.

Monitoring efforts are also ongoing for the the orbits of planets within single-planet systems (e.g., Maire et al. 2019; Kammerer et al. 2021). In addition to providing constraints on the basic orbit geometry, these monitoring efforts offer the potential for future dynamical mass measurements when combined with absolute astrometry or radial velocity measurements of the host star or planet (see Section 3.5). The orbit geometries of imaged planets within single-planet systems have been used to infer the presence of additional companions. Rameau et al. (2016) compared the predicted range of periastron and apastron distances of HD 95086 b to the radial extent of the two circumstellar debris disks in this system between which the planet resides (Moór et al. 2013; Su et al. 2015). Their analysis suggested that HD 95086 b does not have a sufficiently large eccentricity to be

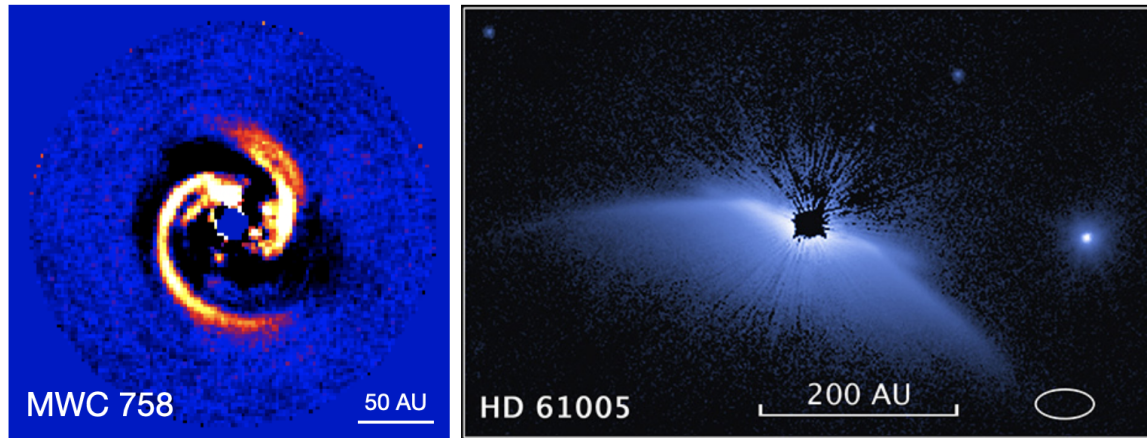


Fig. 13.— The protoplanetary disk around MWC 758 (left; SCEXAO team, unpublished) and the debris disk around HD 61005 (right; NASA/ESA/G. Schneider) both have morphologies that can be explained by the gravitational influence of an orbiting planet. The spiral arms around MWC 758 can be generated by an external orbiting companion (e.g., [Dong et al. 2015b](#), c.f. [Wagner et al. 2018](#)), while the swept-back morphology of the HD 61005 debris disk can be explained by an inner eccentric planet ([Esposito et al. 2016](#)).

responsible for truncating the outer edge of the inner debris disk. Instead, an additional massive planet is required on a shorter orbital period, one that lies below the current sensitivity limits for this star. In other systems, a significant non-zero eccentricity may provide evidence for interior massive companions due to their effect on the relative astrometry between the star and the outer imaged planet (e.g., [Maire et al. 2019](#)). Continued astrometric monitoring will differentiate between a true non-zero eccentricity and a spurious detection caused by the perturbation of an inner companion.

Comparing the orbital geometry of planets to those of brown dwarfs and stars may probe of the formation mechanisms. For individual objects, [Bryan et al. \(2020b\)](#) has used the measured misalignment between the planet’s orbit, rotation and stellar spin axes as an empirical test of various formation mechanisms and dynamical processes. Differences between planet and brown dwarf eccentricity distributions may also probe formation mechanisms (see Section 6.4; [Bowler et al. 2020a](#)).

5.2. Planet-Disk Interactions

The many main sequence stars with IR excess found in the 1980s to 2000s by the IRAS, ISO, and Spitzer missions along with early resolved images of disks provided evidence for numerous, nearby optically thin, Kuiper belt-like debris disks that may be nascent planetary systems (e.g. [Backman and Paresce 1993](#); [Smith and Terrile 1984](#)). Pluto-sized objects in these exo-Kuiper belts stir collisions between planetesimals to produce copious debris; stirring may also be driven by massive jovian planets ([Kenyon and Bromley 2004, 2008](#); [Kennedy and Wyatt 2010](#)). These same missions showed evidence for numerous *transitional* protoplanetary disks whose spectral energy distributions (SEDs) suggested cleared cavities or gaps (e.g. [Españolat et al. 2007](#); [Luhman and Mamajek 2012](#), see Sect. 3.2).

Resolved images of debris and transitional disks reveal tell-tale signposts of planets (Figure 13). Images of transitional disks resolve cavities inferred from SEDs and/or

show spiral density waves plausibly due to massive jovian companions. For example, the disk around MWC 758 shows a complex two-armed spiral structure extending from ~ 25 au to over 100 au ([Benisty et al. 2015](#)); AB Aur’s disk shows significant spiral structure on both tens of au and 100 au scales, some of which may be driven by AB Aur b ([Hashimoto et al. 2012](#); [Tang et al. 2017](#); [Currie et al. 2022b](#)). The PDS 70 disk has a cavity likely cleared by the system’s two protoplanets (e.g. [Keppler et al. 2018](#); [Haffert et al. 2019](#)). Recent work suggests that actively-forming planets could be responsible for gaps, rings, and spirals seen in transitional disks (e.g. [Dong et al. 2015a,b](#)), although some structure (e.g. spirals) could instead be due to gravitational instabilities.

Imaged debris disks may show sharp edges and pericenter offsets caused by the dynamical perturbations from a jovian planet located interior ([Kalas et al. 2005](#)). Modeling the sharp edges of disks may help constrain the masses of planets (e.g. [Kalas et al. 2008](#)). Warps in debris disks are also likely planetary signposts: modeling the warps in some cases can constrain planet masses ([Lagrange et al. 2009](#)).

Finally, mm imaging of highly structured transitional disks may reveal indirect kinematic detection of planets or circumplanetary material. [Benisty et al. \(2021\)](#) image a circumplanetary disk around PDS 70 c. ALMA data for HD 163296 and HD 97048 may show an indirect kinematic detection of protoplanets that currently elude direct detection via local deviations from Keplerian rotation (kinks) ([Pinte et al. 2018](#); [Teague et al. 2018](#); [Pinte et al. 2019](#)).

6. Direct Imaging Surveys and Population Statistics

Most of the known directly imaged exoplanets were discovered as part of large AO surveys. New planet detections and characterization of existing planets via photometry and spectroscopy is only one part of the yield of such surveys; current surveys cover samples of 500-600 stars down to excellent contrasts and yield precise information as to where

giant exoplanets reside in planetary systems. While the new detection yield of these surveys has been relatively small, the deep contrasts probed enable robust studies of the frequency of wide (>20 au) young giant planets.

6.1. Survey Target Selection

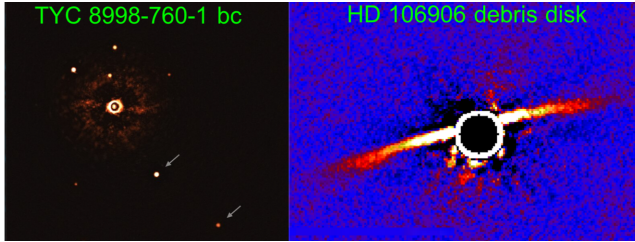


Fig. 14.— Selected high-contrast imaging results for systems in the Sco-Cen Association: (top) The directly-imaged wide separation companions TYC 8998-760-1 bc (~ 160 and 320 au; denoted by arrows), and (bottom) the HD 106906 debris disk (Bohn et al. 2021; Lagrange et al. 2016). HD 106906 also has a much wider-separation planet-mass companion (Bailey et al. 2014).

Direct imaging exoplanet surveys to date have focused primarily on stars drawn from the following samples: **1) Young Moving Groups (MG):** as discussed in Section 3, these groups of stars share similar kinematics and originated in the same star-forming region. The ongoing Gaia mission is helping fill in the low mass stellar members of these groups (e.g. Gagné et al. 2018b, 2021). Some notable moving groups that have been surveyed in depth by direct imaging surveys include: the β Pic MG, the AB Dor MG, the Tucana-Horologium MG, and the Sco-Cen association.

2) Young Star-forming regions (SFR): these are regions with active ongoing star-formation and probe the earliest stages of planet formation (<10 Myr) (see Reipurth 2008a,b). Notable SFRs targeted for direct imaging include Taurus, Ophiuchus, Chamaleon, Perseus, and Serpens. SFRs are excellent regions to search for protoplanets. They have generally been less surveyed than MGs due to their greater distances and confusion between exoplanet and disk signals. There is also some overlap between SFR and MG designations, with boundary cases such as TW Hya and Upper Scorpius within the larger Sco-Cen association (Song et al. 2012; Pecaute et al. 2012).

3) The Sco-Cen niche: Direct imaging programs focusing on the 14 ± 3 Myr (Pecaute et al. 2012) Scorpius-Centaurus association have proven particularly fruitful, yielding a much higher rate of exoplanet detections compared to other young moving group surveys. At a distance of ~ 100 – 150 pc, Sco-Cen is the closest OB association (massive star-forming region) to the Sun and contains over one thousand young stars, well over 100 of which show some indirect evidence for active planet formation (Luhman and Mamajek 2012). It is intermediate in properties between 10-100 Myr-old moving groups and <10 Myr-old embedded young star-forming regions.

Figure 14 shows some direct imaging results from this region. Sco-Cen includes multiple directly imaged planets

and protoplanets orbiting less than ~ 300 au from Sco-Cen host stars: HD 95086 b (Rameau et al. 2013b), HIP 65426 b (Chauvin et al. 2017), PDS 70 bc (Keppler et al. 2018; Haffert et al. 2019), and YSES 2b (Bohn et al. 2021). The region also includes a large number of other wide-separation planet-mass companions or objects with masses near the deuterium burning limit and mass ratios well below $q \sim 0.1$ (e.g. Bohn et al. 2020b; Bailey et al. 2014, TYC 8998-760-1 bc and HD 106906 b). Follow-up observations of many Sco-Cen members stars with ground-based extreme AO and ALMA spatially resolve numerous debris disks and transitional disks (e.g. Lagrange et al. 2016; Garufi et al. 2016; Draper et al. 2016). The disks often show structures (spirals, gaps, arc) that can indicate the presence of formed or forming planets (see Sect. 5.2).

4) Debris disk-bearing stars: debris disks may be signposts of imageable giant planets (see Section 5). The first two directly-imaged planetary systems – HR 8799 and β Pic – both have luminous debris disks. Debris disk-selected surveys like Rameau et al. (2013a); Meshkat et al. (2017) target young, nearby stars whose debris disks have a high fractional luminosity (e.g. 10^{-4} – 10^{-3}). While (Meshkat et al. 2017) find evidence of a correlation between imaged planets and debris disks, debris disks may not correlate with planets detected by RV (Yelverton et al. 2020).

5) A and B stars: these massive stars have short lifetimes, so any companion to them must by definition be young (<200 Myr). Statistical results from several surveys show that substellar and exoplanet companions to A and B stars are indeed more common than similar companions to lower mass FGKM stars (e.g. Nielsen et al. 2019, see also 6.3).

6) Accelerating Stars: unlike the categories of stars discussed above which are selected primarily due to signs of youth, this category of stars show indirect evidence for the dynamical pull from an unseen companion. While such targeted surveys cannot provide unbiased demographic investigations of exoplanets, they can produce significantly higher yields than blind surveys (e.g. Crepp et al. 2016). Some surveys, specifically TRENDS, focused on stars with long-term RV trends indicating the presence of an unseen companion (e.g. Crepp et al. 2012, 2018), discovering a number of brown dwarfs, low-mass stars, and white dwarf companions. A key challenge with this approach is that stars with sufficiently low chromospheric activity to yield good RV precision tend to be old and thus poorer direct imaging targets.

More recently, several groups have begun using astrometric data to select direct imaging targets. This method is immune from the age selection bias that plagues RV-selected target lists. For an isolated star, the proper motion values measured by Hipparcos and Gaia should be identical. However, the tug of an unseen faint companion will cause the position of the primary to diverge slightly from what would be expected for an isolated star (modulated by the orbital period of the companion). Differences in proper motions measured between the Hipparcos and Gaia missions

thus reveal accelerations plausibly caused by unseen planetary companions (Kervella et al. 2019; Brandt 2018, 2021; Fontanive et al. 2019). While in its infancy, this approach is promising, already revealing brown dwarf companions and a handful of white dwarfs (Currie et al. 2020b; Bonavita et al. 2020, 2022; Bowler et al. 2021; Kuzuhara et al. 2022). It is capable of identifying hidden planetary companions: HR 8799, β Pic, and HD 206893 all have proper motion anomalies caused by known planetary companions (Brandt et al. 2021b; Nielsen et al. 2019; Grandjean et al. 2021). Recently, the first discovery of an exoplanet has been gained from this approach (Currie et al. 2022a). The modest astrometric precision of Hipparcos limits the current inventory of stars with detectable accelerations likely caused by planets. However, future *Gaia* data releases should significantly expand the list of known stars whose accelerations may be caused by imageable planets.

6.2. Summary of Surveys

Since the advent of ground-based AO-enabled imaging and space-based imaging with HST, there have been several generations of direct-imaging exoplanet surveys:

1. **Generation 1:** AO-enabled and HST efforts, 2000-2005 (i.e. the state-of-the-art at Protostars and Planets V, the last Protostar and Planets conference with a direct imaging chapter). Typical sample size: < 50 stars. Typical contrast: $\Delta(mag) \sim 8$ at $0.5''$. Examples: Masciadri et al. (2005) (VLT), Chauvin et al. (2003) (ESO 3.6 m, Tuc/Hor moving group), Lowrance et al. (2005) (HST).
2. **Generation 2:** 8-m class telescope + AO + speckle suppression techniques (but no coronagraphy). Typical sample size: 50-100 stars. Typical contrast: $\Delta(mag) \sim 10$ at $0.5''$. Examples: Biller et al. (2007) (VLT and MMT), Lafrenière et al. (2007b) (Gemini), Chauvin et al. (2010) (VLT).
3. **Generation 3:** 8-m class telescope + AO + speckle suppression techniques + coronagraphy. Typical sample size: 100-300 stars. Typical contrast: $\Delta(mag) \sim 11 - 12$ at $0.5''$. Examples: NaCo Large Programme: Desidera et al. (2015); Chauvin et al. (2015); Vigan et al. (2017), NICI Science Campaign: Biller et al. (2013); Wahhaj et al. (2013); Nielsen et al. (2013), International Deep Planet Search (IDPS): Vigan et al. (2012); Galicher et al. (2016), SEEDS: Tamura (2016); Brandt et al. (2014); Janson et al. (2013), PALMS: Bowler et al. (2012a,b, 2015), LEECH: Skemer et al. (2014b); Maire et al. (2015); Stone et al. (2018).
4. **Generation 4:** 8-m class telescope + extreme AO + sophisticated speckle suppression techniques + coronagraphy. Typical sample size: 500-600 stars. Typical contrast: $\Delta(mag) \sim 13 - 14$ at $0.5''$, using

custom-built extreme-AO coronagraphs with spectroscopic capability (due to their IFS detectors). Examples: Gemini-GPIES (Nielsen et al. 2019) and SPHERE-SHINE (Vigan et al. 2021; Desidera et al. 2021; Langlois et al. 2021). Several smaller, targeted surveys are ongoing alongside the large Generation 4 surveys – such as the Search for Planets Orbiting Two Stars SPOTS (Thalmann et al. 2014; Bonavita et al. 2016; Asensio-Torres et al. 2018), the B-star Exoplanet Abundance Study (BEAST) (Janson et al. 2019, 2021), the Young Suns Exoplanet Survey (YSES) (Bohn et al. 2020a,b, 2021), the SCExAO/CHARIS HGCA survey (Currie et al. 2020b), and the Imaging Survey for Planets around Young stars (ISPY) (Launhardt et al. 2020).

In aggregate, these surveys typically detect ~ 1 sub-stellar or exoplanet companion per 100 stars (e.g. meta-analyses by Bowler 2016; Bowler and Nielsen 2018), although targeted surveys (e.g. focused on accelerating stars) may produce higher yields.

Most of the direct imaging surveys described above have focused on planet detection in the near-IR, especially near H band. However, some surveys – e.g. LEECH and ISPY (Heinze et al. 2010; Skemer et al. 2014b; Launhardt et al. 2020) – have searched in the thermal IR, in particular the L_p passband ($3.78 \mu m$). For a given residual wavefront error, the Strehl ratio is significantly higher in the thermal IR than in the near IR. As shown in Figure 3, contrasts are more advantageous in the thermal IR for both young and (especially) intermediate-aged jovian planets. The planets β Pic b and HR 8799 e were chiefly discovered from thermal IR data; discovery papers for other planets (e.g. PDS 70 b) also included thermal IR imaging (Lagrange et al. 2009; Marois et al. 2010a; Keppler et al. 2018). The thermal IR has lower background star contamination compared to the near-IR. Extreme AO systems can detect planets 100 times fainter than conventional AO counterparts in the near-IR (Macintosh et al. 2014). However, thus far, extreme AO in the near IR has a smaller (factor of \sim a few) advantage over a conventional AO system operating in the thermal IR (e.g. see GPI/H band vs. Keck/thermal IR detections of 51 Eri b; Macintosh et al. 2015).

6.3. Occurrence Rates and Demographics

The planet occurrence rate (number of planets per star) – and how that occurrence rate varies as a function of stellar or planetary properties (e.g. host mass, planet mass, orbital semi-major axis, host star metallicity) – strongly constrains models of planet formation and evolution, particularly as we build up larger sample sizes. Early demographics studies focused on RV survey results, showing correlations in giant exoplanet occurrence with stellar metallicity (Fischer and Valenti 2005) and host star mass (Johnson et al. 2007), and constraining occurrence rates as a function of planet mass and semi-major axis (Cumming et al. 2008). In particular, Cumming et al. (2008) found a power-law dependence

of planet period that corresponded to a rising occurrence rate of giant planets as a function of log semi-major axis out to ~ 2.5 au.

Given the low yield of exoplanets from early direct imaging surveys, detailed occurrence rate measurements proved difficult. Instead, Generation 1 and 2 survey analyses focused on constraining occurrence rates with assumed mass and semi-major axis distributions, or setting upper limits on the largest semi-major axis for which the *Cumming et al. (2008)* power law could be consistent with direct imaging yields (e.g. *Masciadri et al. 2005*; *Lafrenière et al. 2007b*; *Nielsen and Close 2010*). These early results showed that the occurrence rate of giant planets ($\gtrsim 1 M_J$) in wide orbits ($\gtrsim 10$ au) was relatively low ($\lesssim 10\%$), and that the rising power law of *Cumming et al. (2008)* cannot extend beyond tens of au and still be consistent with the lower occurrence rates found by direct imaging surveys.

Starting with the first imaged planet discoveries in 2008 (*Marois et al. 2008b*; *Lagrange et al. 2009*), it became possible for surveys to directly measure occurrence rates, rather than simply placing upper limits. A planet of a given mass and separation should be easier to image around a low luminosity, low-mass star than a higher luminosity, high-mass star. However, hosts (e.g. HR 8799, β Pic) of directly-imaged wide-separation giant planets were typically more massive than the Sun ($\sim 1.5\text{--}2 M_\odot$).

As Generation 3 surveys reached higher contrasts than their predecessors, giant planets with masses down to $\sim 2 M_{Jup}$ became detectable at separations above ~ 50 au (beyond $\sim 1''$) for nearby moving group stars. Yields from these surveys remained low, however, typically 0-2 planets per survey. Given the limited number of nearby young stars, the same planet was often detected by multiple surveys (e.g. β Pictoris b, κ And b). Occurrence rate analysis confirmed the relatively low upper limits implied by Generation 1 and 2 surveys, with $\lesssim 10\%$ of nearby, young stars hosting a wide-separation giant planet. Analysis of occurrence rate as a function of stellar mass from these Generation 3 surveys confirmed that wide-separation giant planets do not follow an extrapolation of the *Cumming et al. (2008)* power laws. Wide-separation jovian planets were also found to be more common around higher-mass stars (e.g. *Lannier et al. 2016*). Wide-separation giant planet occurrence rates may also be higher for stars with Kuiper belt-like debris disks than diskless stars (*Meshkat et al. 2017*).

Generation 4 surveys have significantly higher sensitivity to giant planets between $\sim 10\text{--}50$ au compared to previous generations of surveys, due to improved coronagraphs and AO. These surveys had larger survey sizes, and detected planets at separations and contrasts not reachable with previous instrumentation (e.g. 51 Eridani b at $\sim 2 M_J$ and ~ 13 au). Higher yields of substellar companions meant more detailed demographic studies became possible, with the first analysis of GPIES data detecting 3 brown dwarfs and 6 giant planets, and the first SHINE demographic analysis finding 8 giant planets and 7 brown dwarfs (Figure 15). These surveys confirmed at $\sim 3\sigma$ that wide-separation giant

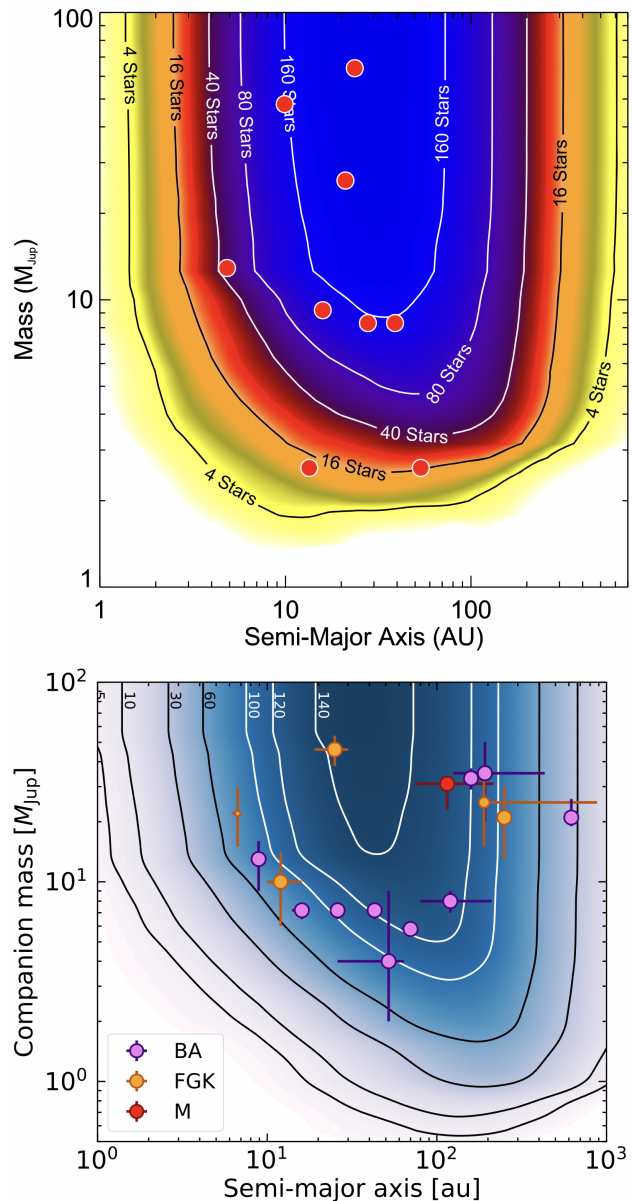


Fig. 15.— Tongue plots (also called depth of search plots, *Lunine et al. 2008*) showing detections and sensitivities to substellar companions for the GPIES (top) and SHINE (bottom) surveys. Unlike previous generations of surveys, these surveys could detect giant planets as close as ~ 10 au from their parent star (Figure 4 of *Nielsen et al. 2019*, Figure 1 of *Vigan et al. 2021*).

planets ($2\text{--}13 M_J$ at $10\text{--}100$ au) had higher occurrence rates around higher-mass ($\gtrsim 1.5 M_\odot$) stars compared to Solar-type stars (*Vigan et al. 2021*; *Nielsen et al. 2019*).

These higher planet yields also allowed constraints the occurrence rate of wide-separation giant planets as a function of semi-major axis, planet mass, and stellar host mass. Power law fits to the occurrence rates of wide-separation giant planets as a function of these parameters show that the giant planet occurrence rate at $10\text{--}100$ au rises with increasing stellar mass, decreasing planet mass, and decreasing semi-major axis (*Nielsen et al. 2019*). Comparing the power-law fits for giant planets brown dwarfs suggests that

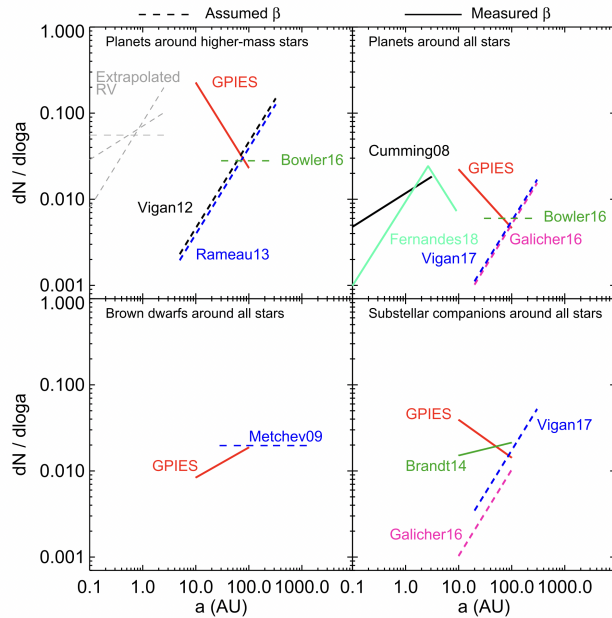


Fig. 16.— Occurrence rate of giant planets ($5\text{--}13 M_{\text{Jup}}$), brown dwarfs ($13\text{--}80 M_{\text{Jup}}$), and substellar companions ($5\text{--}80 M_{\text{Jup}}$) from multiple direct imaging and radial velocity surveys. Giant planets around higher-mass stars (top left panel) and around all stellar types (top right panel) are consistent with a peak in the distribution near the snow line ($\sim 3\text{--}10$ au), with falling occurrence rates toward larger and smaller separations. Current demographics results provide robust evidence that giant planets are more common around higher-mass stars, and weaker evidence that giant planets and brown dwarfs follow different underlying distributions. (Figure 8 of [Nielsen et al. \(2019\)](#))

planets and brown dwarfs are not drawn from the same population at wider separations, consistent with separate formation mechanisms ([Nielsen et al. 2019](#)). When combined with results from RV surveys at smaller separations, the distribution of giant planets as a function of semi-major axis also appears (Figure 16) consistent with a peak at 3–10 au, near the snow line, with falling occurrence rates at smaller and larger separations.

RV population studies like [Fernandes et al. \(2019\)](#) and [Fulton et al. \(2021\)](#) are now sensitive to giant planets beyond the snow line. Both studies find a peak in the giant planet occurrence rate near the snow line. The frequency of planets with masses of $5\text{--}14 M_{\text{J}}$ between 10–100 au extrapolated from the [Fulton et al. \(2021\)](#) RV study is in excellent agreement with the same measurement (in the same mass and separation bins) from the Gemini-GPIES survey ([Nielsen et al. 2019](#)). Taken together, results from imaging and RV imply a giant planet occurrence rate (across all separations) of $\sim 20\%$ ([Fulton et al. 2021](#)) for Sun-like stars, and potentially significantly higher for giant planets around higher-mass stars ([Nielsen et al. 2019](#)).

6.4. Testing Formation Mechanisms with Direct Imaging Exoplanet Demographics

The demographics of directly-imaged planets can provide powerful constraints on their likely formation mechanism. There are two main pathways by which giant planets may form:

1. *Core Accretion* – a rocky core accretes first from planetesimals, followed by a gas envelope (cf. [Mizuno 1980](#); [Pollack et al. 1996](#); [Alibert et al. 2004](#); [Ida et al. 2013](#)). The proto-planet’s position within the disk will eventually determine its final mass; for instance, Jupiter, closer to the peak density of the Sun’s protoplanetary disk, managed to accrete a considerably larger gas envelope than Neptune. Pebble accretion can enhance the protoplanetary accretion rate, enabling the formation of massive planets far from their star ([Johansen and Lambrechts 2017](#)).
2. *Gravitational Instability within a Disk* – If a disk is sufficiently massive to experience self-gravity, parts of the disk can undergo fragmentation and quickly form giant planets (cf. [Kuiper 1951](#); [Boss 1998](#); [Vorobyov et al. 2013](#); [Forgan and Rice 2013](#); [Forgan et al. 2015](#)). [Kratter et al. \(2010\)](#) note that in most cases, these fragment-formed companions will grow further into substellar or low mass stellar companions – only the lowest mass members of this cohort remain planetary.

For very low mass primaries (e.g. brown dwarfs), binary-like formation can also produce planetary mass companions ([Offner et al. 2010](#)). This is the probable formation mechanism for the brown dwarf - planetary mass binary 2M1207 B ([Chauvin et al. 2004](#)), for instance.

Giant planets observed at wide separations experience significant migration or scattering either during their formation or immediately afterwards ([Morbidelli et al. 2009](#); [Johansen and Lambrechts 2017](#); [Forgan et al. 2018](#); [Emsenhuber et al. 2021](#)). Exoplanet demographics from large surveys provide critical tests as to which of these formation and migration mechanisms are dominant, as different formation mechanisms place planets in very different parts of their stellar system. Gravitational instability predicts giant planets generally at wider separations, with more higher-mass planets than lower-mass ones, and no strong dependence on stellar mass. Core accretion, on the other hand, predicts more giant planets closer to the star and more lower-mass planets than higher-mass ones. Figure 17 shows a comparison of simulated planet populations formed via core accretion ([Ida et al. 2013](#)) against a population formed via disk instability ([Forgan et al. 2015](#)). Both of these studies simulate multiple planetary embryos per system; after an initial formation phase, both model populations undergo an evolution phase where they can scatter or be scattered by other objects in their system. Obviously this is comparing just two simulation codes and a wide variety of similar popula-

tions exist in the literature³. However, while the exact population simulated by each team and model considered will vary, the hallmarks of each formation mechanism remain.

In the last decade, a number of large direct imaging surveys have used results from these types of population synthesis codes to inform their statistical analyses. Informed by theoretical results, *Janson et al. (2011, 2012)*; *Rameau et al. (2013a)* define regions in mass-semi-major axis space where gravitational instability formation would be possible. Given non-detections in these mass - semi-major axis regions in their surveys, they were then able to set upper limits on the frequency of giant planets formed via gravitational instability. *Vigan et al. (2017)* found that the disk instability population could describe the companions detected in their survey, but only if formation by disk instability was relatively rare. Comparisons of core accretion population synthesis models to direct imaging surveys before the advent of Gemini-GPI and SPHERE-SHINE (e.g. *Nielsen and Close 2010*; *Chauvin et al. 2015*; *Vigan et al. 2017*) did not yield meaningful constraints as most of the predicted core-accretion planets were undetectable for these surveys.

Statistical results from the Gemini- GPIES and SPHERE-SHINE surveys (*Nielsen et al. 2019*; *Vigan et al. 2021*) suggest that core accretion is the dominant mechanism forming directly imaged giant planets. *Nielsen et al. (2019)* compared the power-law fit to 10-100 au giant planets detected in the GPIES survey to predictions of both gravitational instability and core accretion. While the brown dwarf companion population was well-described by gravitational instability, *Nielsen et al. (2019)* found giant planets closer to their star in comparison to the brown dwarf companions, with more lower-mass planets than higher-mass planets, and with a higher frequency of planets around higher mass stars in the samples – all hallmarks of core accretion. Fitting both disk instability and core accretion populations (*Forgan et al. 2018*; *Mordasini et al. 2017*) simultaneously to the detected companions and contrast limits of a sample of FGK stars observed as part of the SPHERE-SHINE F150 sample, *Vigan et al. (2021)* qualitatively found that the contribution of the core accretion simulated population is larger than the contribution of the gravitational instability simulated population, suggesting that core accretion is the dominant formation mechanism for this sample as well.

Directly imaged giant exoplanets are numerous enough to study the demographics of companions themselves, rather than only from detection statistics across a survey. For instance, *Bowler et al. (2020a)* considered eccentricities of 27 long-period giant planets and brown dwarf companions between 5 and 100 au, derived from their own orbital fits to literature and additional Keck astrometry. They tentatively found ($\sim 2\text{-}\sigma$) that their population dominated by giant planets ($2\text{-}15 M_J$) had somewhat lower orbital eccentricities than a brown dwarf-dominated population ($15\text{-}75 M_J$), which displayed a broad distribution

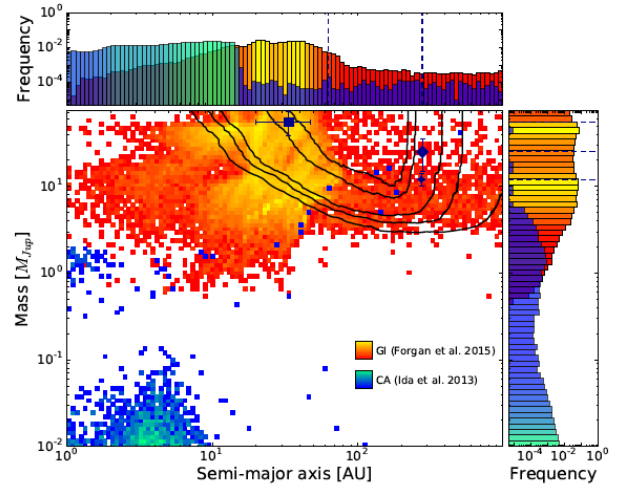


Fig. 17.— Plot reproduced from *Vigan et al. (2017)* comparing simulated population of companions formed via core accretion (blue/green *Ida et al. 2013*) and gravitational instability (red/yellow *Forgan et al. 2015*). Lighter colors represents higher occurrence rates. Histograms of the distributions for each model population in semi-major axis (au) and mass (M_J) are shown on the top and side respectively. Mean detection probabilities and the detected companions from the *Vigan et al. (2017)* sample are overplotted as black contours and points respectively. Both of these simulated populations include multiple planetary embryos per system; both model populations undergo an evolution phase where they can scatter or be scattered by other objects in their system. Disk instability predominantly forms massive companions ($1\text{-}100 M_J$) far from the star, whereas core accretion dominates within 10 au and predominantly produces lower mass companions.

of eccentricities with a peak in eccentricity between 0.6 and 0.9. These population-wide differences in eccentricity may suggest different formation mechanisms for the two populations: formation within a disk for directly-imaged exoplanets vs. cloud fragmentation (binary-like formation) for brown dwarf companions.

7. The Future of Direct Imaging

Over the next 5 years, new technology applied to exoplanet imaging instruments from the ground will close the gap between the planets we can image and those we have detected indirectly, while JWST will enable the detection of planets undetectable from the ground. By 2030, new facilities should provide the first reflected-light detections and spectral characterizations of mature planets. Finally, by the 2040s, we should be able to directly detect rocky, habitable zone planets around the nearest M stars and Sun-like stars using ELTs and NASA/ESA flagship missions.

In this section, we project the near, medium, and long-term development of direct imaging through technological innovation. We describe as well new facilities applying these innovations and the science questions we will begin to answer via these new capabilities.

³See Chapter 20 from this volume, "Planet Formation Theory in the Era of ALMA and Kepler: From Pebbles to Exoplanets".

7.1. New Tools

The hardware enabling current high contrast imaging capabilities described in §2.2.1 – detectors, deformable mirrors, high performance computing – will continue to advance and provide deeper contrast levels. Improved coronagraph designs will also open access to planets at separations near the telescope diffraction limit. For ground-based extreme AO these incremental gains are being implemented in instruments on current large telescopes, either as part of a continuous development process (SCEXAO, MagAO-X, KPIC [Guyon et al. 2020](#); [Close et al. 2018](#); [Males et al. 2020](#); [Echeverri et al. 2019](#); [Mawet 2021](#)), or major upgrades to existing facility instruments (GPI-2.0, SPHERE+ [Chilcote et al. 2020](#); [Boccaletti et al. 2020](#)). The same hardware technologies are at the core of future ground and space instrument designs, and will provide science capability improvements beyond the already significant gains expected from re-deploying current instruments on larger telescopes.

Advances in low-noise detectors and optical fiber technologies will enable exoplanet spectroscopy at high spectral resolution. Early on-sky demonstration (KPIC, REACH, [Mawet 2021](#); [Kotani et al. 2020](#)) are paving the way for more capable future systems (MODHIS, [Dumas 2020](#)). Polarization differential imaging systems optimized for high contrast imaging (ZIMPOL, VAMPIRES, [Schmid et al. 2018](#); [Norris et al. 2020](#)), when deployed on largest telescopes, will be able to reveal partially polarized starlight reflected by exoplanet atmospheres.

Upcoming transformative advances in wavefront control, calibration, and starlight suppression will yield order-of-magnitude level improvement in contrast, or enable new measurement capabilities. These include:

- **Sensor fusion and predictive control** will optimize how real-time wavefront sensing telemetry is used to estimate wavefront errors. In predictive control, current and past measurements are combined to extrapolate future optimal AO commands, reducing time lag errors and improving sensitivity ([Males and Guyon 2018](#)). By combining information from multiple sensors operating at separate wavelengths or in different optical configurations, the precision and accuracy of wavefront estimates should also be further improved ([Guyon et al. 2020](#)).
- **PSF calibration from real-time telemetry** holds the potential to numerically subtract starlight from science images at the photon noise level ([Gilles et al. 2011](#); [Guyon et al. 2020](#)).
- **Coherent modulation** can provide a real-time estimate of starlight, which can then be numerically removed from science images. The modulation can be performed spatially in a self-coherent camera ([Baudoz et al. 2006](#)), or temporally with coherent differential imaging.
- **Photonic technologies** provide new ways to filter,

transport and combine light ([Gatkine et al. 2019](#)). Applications include fiber-fed spectroscopy, wavefront sensing, and nulling interferometry ([Jovanovic et al. 2020](#); [Norris et al. 2020](#); [Martinod et al. 2021](#)).

- **Laser beacons** can improve wavefront control performance beyond the fundamental limits imposed by starlight photon noise. The approach has been successfully used for non-extreme AO ground-based observations, and is now being considered for both ground-based and space based ([Douglas et al. 2019](#)) high contrast imaging applications.
- **Starshades** can provide high contrast imaging without requiring exquisite optical stability. They are particularly well-suited for long exposure wide spectral coverage spectroscopy of exoplanets with space-based telescopes ([Gaudi et al. 2020](#)).

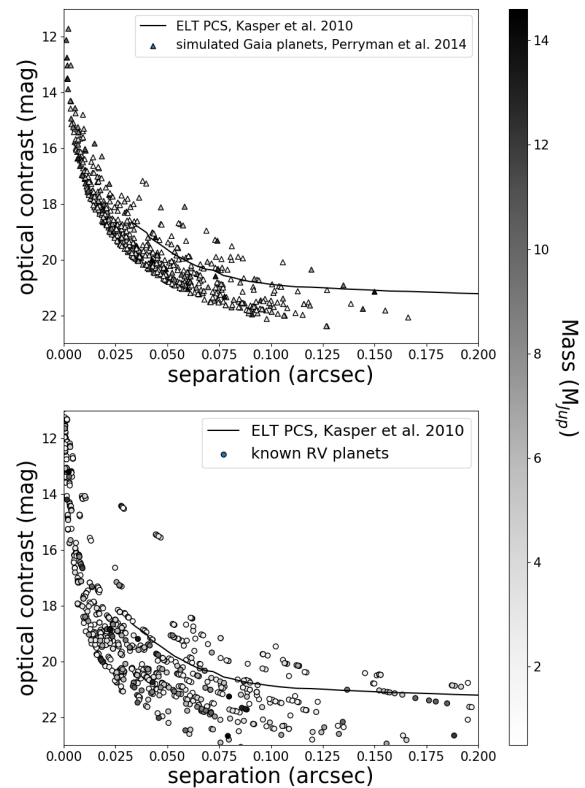


Fig. 18.— Detectability of mature giant planets in optical reflected light using an extreme AO planet-finding camera at an ELT. *Top*: simulated Gaia detected planets (drawn from the distribution in [Perryman et al. 2014](#)), *Bottom*: known RV planets. The contrast curve shown is a prediction for the ELT PCS planet-finder ([Kasper et al. 2010](#)), but is representative of the performance expected for similar instruments on ELTs. Known RV planet properties draw from the NASA Exoplanet Archive. Contrasts are computed at the planets’ brightest phases.

7.2. New Instruments and Facilities

James Webb Space Telescope (2022) – Launched in December 2021, the cryogenic, IR-optimized *JWST* may significantly expand the diversity of imaged exoplanets and

will break new ground with exoplanet characterization. The 6.5m JWST will have poorer resolution and performance at the smallest angular separations than most leading exoplanet-imaging platforms. However, JWST will have unrivaled sensitivity in the thermal/mid IR (3–20 μm) compared to ground-based instruments, which must contend with bright sky emission: JWST can discover cold sub-Jupiter mass planets at wide separations around the nearest stars (Beichman et al. 2010; Carter et al. 2021; Hinkley et al. 2022). JWST Early Release Science data of the young exoplanet system HIP 65426b suggests that JWST is exceeding its nominal predicted performance by a factor of up to 10 (Carter et al. 2022), enabling the detection of planets down to masses of 0.3 M_J beyond 100 au. Thermal IR IFS data will be free of telluric contamination.

Next-generation extreme AO on 6-10m telescopes (2022-2026) – Over the next few years, upgraded systems should improve planet-to-star contrasts by a factor of 10–100 \times at small separations, reaching contrast floors nearing 10^{-7} , and improving performance for optically fainter stars. SCEXAO on Subaru will undergo major hardware and software upgrades, improving upon its current implementation of advances such as predictive control incorporating ones like real-time telemetry calibration, coherent modulation, and photonics technology (Guyon et al. 2020; Currie et al. 2020a). MagAO-X (Males et al. 2020) will leverage recent hardware and algorithm advances to push high contrast performance in the optical. Upgrades to GPI and SPHERE will likewise feature improved wavefront sensing capabilities (e.g. Chilcote et al. 2020; Boccaletti et al. 2020).

Roman-CGI (2026) – The Coronagraphic Instrument on the Roman Space Telescope will provide the first test of focal-plane wavefront control and advanced coronagraphy in a space-borne environment (Spergel et al. 2013). CGI’s benchmark performance is $\sim 10^{-7}$: comparable to the best contrasts expected from ground-based extreme AO on 8-10m telescopes in the next 5 years. However, laboratory tests simulating a space environment suggest that CGI could reach contrasts as deep as $\sim 10^{-9}$: sufficient to image true Jupiter analogues in reflected light (Shi et al. 2017; Spergel et al. 2013). The potential success of CGI’s technological demonstration may justify a follow-on science program focused on detection and spectral characterization of reflected-light gas giant planets.

Planet imaging with Extremely Large Telescopes (2030s) – The large apertures and excellent sky conditions at the sites of the upcoming *European Extremely Large Telescope* (E-ELT; 39m; Cerro Armazones), *Thirty Meter Telescope* (TMT; 30m; preferred site is Maunakea), and the *Giant Magellan Telescope* (GMT; 24.5m; Las Campanas) make exoplanet imaging with ELTs a critical science case. All three telescopes have approved or planned high-contrast imaging instruments covering the red optical to the mid-IR.

Mid-IR instruments – e.g. TMT/MICHI (Packham et al. 2018), E-ELT/METIS (Brandl et al. 2021) – use a single high-order AO correction plus a coronagraph to achieve expected contrasts of $\sim 10^{-7}$ at 3–10 μm capable of imaging

warm Neptune or larger-sized planets around many nearby stars and exo-Earths around a dozen or so solar-type stars (Lopez-Morales et al. 2019). Those operating in the red optical to near-IR – e.g. TMT/PSI (Jensen-Clem et al. 2021) and E-ELT/PCS (Kasper et al. 2021) – benefit from a second AO correction in series to achieve expected contrasts of $\leq 10^{-8}$, sufficient to image rocky, habitable zone planets around nearby M dwarfs.

Space-borne high-contrast imaging flagship missions (2040s+) – The Astro 2020 Decadal Survey ranked a large-aperture, direct imaging flagship mission – similar to the proposed HabEx and LUVOIR concepts (Gaudi et al. 2020; The LUVOIR Team 2019) – as a top space-based priority. The mission will employ advanced wavefront control and coronagraphy, building upon technical developments from Roman-CGI and the ground and yielding 10^{-10} contrasts. In some designs, it would fly with a starshade capable of delivering even deeper contrasts and higher SNR detections of exo-Earths identified from coronagraphy. The European Space Agency is considering a mission – LIFE – to detect and spectrally characterize exo-Earths through high-contrast interferometry (Quanz et al. 2021).

7.3. Future Science Focuses

The next 5 years: young giant exoplanet atmospheres at $\lambda > 5 \mu\text{m}$ with JWST – JWST is already enabling the first exploration of directly imaged exoplanet atmospheres at $\lambda > 5 \mu\text{m}$. Especially past 10 μm , directly imaged exoplanet as well as brown dwarf atmospheres are almost completely unexplored. Pre-JWST, the only existing $>10 \mu\text{m}$ spectra for any substellar object are for a handful of L and T field brown dwarfs from the Spitzer cryogenic mission (Cushing et al. 2006; Suarez et al. 2022).

The recently-presented JWST/NIRSPEC spectrum for L7, planet-mass companion VHS 1256 b demonstrates JWST’s promise for atmospheric characterization (Miles et al. 2022). The spectrum reveals numerous molecules – H₂O, CH₄, CO, CO₂, and K – at a wide range of wavelengths, including those poorly accessible from the ground. The $\sim 10 \mu\text{m}$ spectral region is particularly diagnostic of atmospheric properties. The presence of silicate emission at 10 μm directly confirms silicate clouds in VHS 1256 b’s atmosphere (Luna and Morley 2021; Miles et al. 2022), the existence of which has previously been inferred by modeling, but not directly detected. Future observations with JWST will confirm whether this feature (and hence direct evidence for clouds) is commonly found in other directly imaged exoplanet spectra. Longer wavelengths may also better distinguish between different theoretical models (e.g. Skemer et al. 2012, 2014a). JWST may also detect thermal emission from sub-Jupiter mass planets >30 au from their host stars and sub-Saturn mass planets beyond >50 au (Beichman et al. 2010; Carter et al. 2021).

The next 5 years: ground-based advances – Next-generation extreme AO systems will achieve contrasts capable of detecting young Jupiters and intermediate-

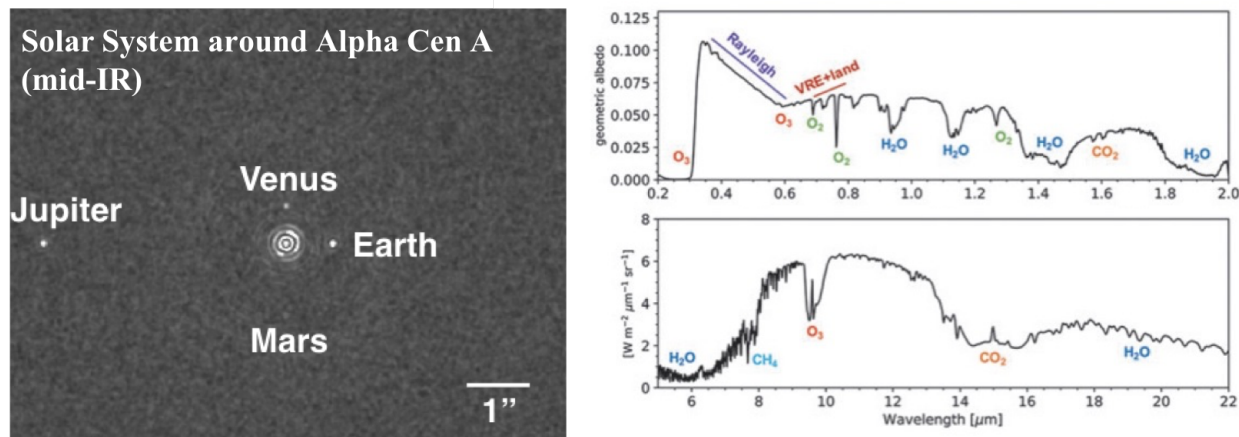


Fig. 19.— Detecting and characterizing exo-Earths with future facilities (from [Lopez-Morales et al. 2019](#)). (left) Simulated image of solar system around α Cen A imaged at $10\ \mu\text{m}$ with an instrument like TMT/MICHI. In several hours, an Earth and Jupiter are visible: in 100 hours, 4 planets are visible. (right) Biosignatures in the optical and mid IR probed by a space coronagraphic mission like HabEx/LUVOIR and from the ground with ELTs, respectively ([Schwieterman et al. 2018](#)).

aged superjovian-mass planets at Jupiter-like separations. Should contrasts at or slightly below 10^{-7} be reached, these new instruments might be capable of providing the first images of planets in reflected light.

Direct imaging detections of significant numbers of super-Earth or Earth mass planets will have to wait for the advent of ELTs and new space telescopes. However, imaging the known habitable zone planet Proxima Centauri b ([Anglada-Escudé et al. 2016](#)) might be possible with 8-m class telescopes and substantial dedicated observing time. For example, [Lovis et al. \(2017\)](#) propose targeting this planet by combining VLT/SPHERE with the ESPRESSO high resolution spectrograph. They estimate that 20-40 nights of observations would yield a $5\text{-}\sigma$ detection of the planet and that 60 nights of observations would yield a $3.6\text{-}\sigma$ detection of the biosignature gas O_2 .

The next 10 years: Imaging and characterizing mature giant planets – With the advent of ELTs on the ground and dedicated space-based missions such as CGI, direct imaging of exoplanets will expand from detecting young planets via thermal emission in the infrared to detecting mature planets via reflected light in the optical. Indirect methods like astrometry and RV will provide a sample of solar-system age giant planets which can then be imaged via their reflected optical light using exoplanet imaging cameras on ELTs such as PCS on the E-ELT ([Kasper et al. 2021](#)) and PSI on the TMT ([Guyon et al. 2018](#)). For example, Figure 18 compares a predicted ELT planetfinder reflected light contrast curve ([Kasper et al. 2010](#)) with a simulated population of Gaia-detected giant planets from [Perryman et al. \(2014\)](#) and known RV planets. Extreme AO planet-finding cameras on ELTs will directly image and spectrally characterize dozens of solar-system age giant planets.

These new facilities and instruments will also enable deeper characterization of the current cohort of young, directly imaged exoplanets. In particular, these instruments will incorporate high resolution spectroscopic capability

alongside extreme adaptive optics and state-of-the-art coronagraphs ([Kasper et al. 2021](#)). This will enable high-precision spectroscopic and rotational studies, including the possibility of directly reconstructing top-of-atmosphere (TOA) cloud structure for a handful of young giant exoplanets ([Snellen et al. 2014](#); [Crossfield 2014](#)). A particularly exciting future opportunity will be direct mapping of giant planet atmospheric structure via the Doppler imaging technique, which uses time-resolved, high-resolution spectroscopy ($R > 40000$) to produce a high SNR composite line profile, then uses maximum entropy methods to reconstruct TOA structure from that line profile ([Vogt et al. 1987](#)). To date, only one extremely bright brown dwarf, Luhman 16B, has been Doppler-mapped ([Crossfield et al. 2014](#)) and only 2-3 others are sufficiently bright for this technique with 8-m class telescopes ([Crossfield 2014](#)). Extremely large telescopes will enable Doppler imaging of dozens of brown dwarfs and a few directly imaged planets ([Crossfield 2014](#)).

The next 20 years: Imaging and characterizing exo-Earth twins – ELTs will play an important role in imaging and characterizing habitable zone rocky exoplanets around a range of primary star masses. Instruments like E-ELT/PCS and TMT/PSI will image and spectrally characterize a few dozen habitable zone exoplanets around M stars in red optical to near-IR reflected light at wavelengths probing key biomarkers (e.g. O_2 at $1.27\ \mu\text{m}$; [Lopez-Morales et al. 2019](#)). Very deep mid-IR data for the nearest $\sim 10\text{--}15$ Sun-like stars can detect thermal emission bracketing the $\sim 10\ \mu\text{m}$ ozone feature (Figure 19, left panel).

Using a combination of advanced wavefront control, coronagraphy, and/or a starshade, space-based missions like HabEx, LUVOIR, and LIFE should be capable of imaging and spectrally characterizing exo-Earths around several tens of Sun-like stars. The NASA missions will split their exo-Earth finding science program into a shallow coronagraphic search and a deep, focused follow-up of candidate habitable zone planets conducted with coronagraphy (LU-

VOIR) and/or a starshade (HabEx). Survey designs are still in development and strongly depend on the adopted value of η_{Earth} – the frequency of Earth-like planets around Sunlike stars. Currently, values for η_{Earth} are extrapolated from the Kepler transiting planet mission (*Dressing and Charbonneau 2015; Kopparapu et al. 2018*), although these η_{Earth} values describe only the frequency of small, rocky planets, not necessarily habitable planets.

These missions will provide not just detections but spectra to identify biosignature gases (and hence life) in the atmospheres of these planets (Figure 19, right panel). No one biosignature gas by itself can clearly indicate the presence of life, as many biosignature gases, such as O_2 , can have abiotic sources (*Meadows et al. 2018*). Thus, confirming the presence of life on a planet requires detecting a combination of gases that do not appear together in equilibrium state – disequilibria in this case is driven by the presence of life (*Meadows et al. 2018*). To ensure coverage of a wide range of biosignature gases, these missions will deliver spectra over a broad wavelength coverage: e.g. from near-ultraviolet to near-IR for LUVOIR.

The study of exoplanets has yielded many surprising results, such as the existence of hot Jupiters, the ubiquity of super-Earths, and the extremely red colors of young giant exoplanets, thus, caution is merited both in our predictions of what we may find with future instruments as well as in our interpretation of the data yielded by such instruments. Considering this, it will likely require detections of key biosignature gases in a statistically significant sample of Earth-like exoplanets to be firmly convinced that we have truly detected life outside our own solar system.

The detection of habitable zone planets around Sun-like stars through M stars through direct imaging will be necessary to provide our first steps towards truly providing a context for our own Earth. M star planets encounter a very different radiation environment than planets around FGK stars and are predicted to be tidally locked, which may pose significant obstacles to true habitability (*Shields et al. 2019*). To understand the frequency of life, it is then key to detect and characterize both M star habitable zone planets and planets more like our own – the only planet we know to date to truly be inhabited. However, detection and characterization of true exo-Earth twins (defined here as planets with similar mass as the Earth in the habitable zone of Sunlike stars) pose a challenge for transit and RV techniques. If viewed as an exoplanet, the Earth would only appear to transit once a year, thus requiring observations over many years or even decades to reach sufficient S/N in transit spectra to search for biosignatures. While the sensitivity of current RV instruments such as ESPRESSO and HARPS is sufficient to detect the RV signal of an exo-Earth twin around a Sunlike star, that signal will generally be drowned out by noise from the stellar activity of the host star (*Haywood et al. 2020; Langellier et al. 2021*). Thus, while many M star habitable-zone exoplanets will be discovered first via transit or RV, then characterized with direct imaging, direct imaging is more naturally suited for both

the discovery and characterization of true Earth twins.

This review thus concludes where it began, with the prospects for identifying, confirming, and characterizing a true Earth twin around a nearby Sun-like star via direct imaging. The first direct images of exoplanets were published less than 15 years ago. Since then, exoplanet direct imaging has advanced rapidly, constraining the orbits, masses, atmospheres, population demographics and formation mechanisms of young giant planets. We forecast the rapid technical and scientific progress driven by the many and varied exciting new telescopes and instruments coming online in the next 20 years.

With these new capabilities, direct imaging and spectroscopy are highly likely to yield the first detections of true Earth twins and following that, the first detection of life outside the solar system – possibly the first substantive steps towards knowing whether or not we are alone in the universe.

Acknowledgments. This work has benefitted from The UltracoolSheet, maintained by Will Best, Trent Dupuy, Michael Liu, Rob Siverd, and Zhoujian Zhang, and developed from compilations by *Dupuy and Liu (2012)*, *Dupuy and Kraus (2013)*, *Best et al. (2021)*, etc. Discoveries and key insights into the nature of directly imaged extrasolar planets were made from many astronomical sites throughout the world, including Maunakea in Hawai‘i, Cerro Paranal, Cerro Pachon, and Las Campanas in Chile, and Mt. Graham in Arizona. We acknowledge the importance that these sites hold for many in nearby communities from a cultural and/or personal standpoint and support responsible stewardship of the land on which these and other observatories are located.

REFERENCES

- Ackerman A. S. and Marley M. S., 2001 *ApJ*, 556, 2, 872.
 Alibert Y. et al., 2004 *A&A*, 417, L25.
 Allard F. et al., 2012 *Philosophical Transactions of the Royal Society of London Series A*, 370, 1968, 2765.
 Allers K. N. and Liu M. C., 2013 *ApJ*, 772, 2, 79.
 Amara A. and Quanz S. P., 2012 *MNRAS*, 427, 2, 948.
 Andrews S. M. and Williams J. P., 2007 *ApJ*, 659, 1, 705.
 Anglada-Escudé G. et al., 2016 *Nature*, 536, 7617, 437.
 Angus R. et al., 2019 *AJ*, 158, 5, 173.
 Aoyama Y. and Ikoma M., 2019 *ApJL*, 885, 2, L29.
 Apai D. et al., 2013 *ApJ*, 768, 2, 121.
 Apai D. et al., 2016 *ApJ*, 820, 1, 40.
 Apai D. et al., 2017 *Science*, 357, 6352, 683.
 Apai D. et al., 2021 *ApJ*, 906, 1, 64.
 Asensio-Torres R. et al., 2018 *A&A*, 619, A43.
 Backman D. E. and Paresce F., 1993 *Protostars and Planets III* (E. H. Levy and J. I. Lunine), p. 1253.
 Bailey V. et al., 2014 *ApJL*, 780, 1, L4.
 Bailey V. P. et al., 2018 *Proc. SPIE*, vol. 10698, p. 106986P.
 Baines E. K. et al., 2012 *ApJ*, 761, 1, 57.
 Baraffe I. et al., 2002 *A&A*, 382, 563.
 Baraffe I. et al., 2015 *A&A*, 577, A42.
 Barman T. S. et al., 2011a *ApJ*, 733, 1, 65.

- Barman T. S. et al., 2011b *ApJL*, 735, 2, L39.
- Barman T. S. et al., 2015 *ApJ*, 804, 1, 61.
- Barnes S. A., 2007 *ApJ*, 669, 2, 1167.
- Baudoz P. et al., 2006 *IAU Colloq. 200: Direct Imaging of Exoplanets: Science & Techniques* (C. Aime and F. Vakili), pp. 553–558.
- Beichman C. A. et al., 2010 *PASP*, 122, 888, 162.
- Benisty M. et al., 2015 *A&A*, 578, L6.
- Benisty M. et al., 2021 *ApJL*, 916, 1, L2.
- Berardo D. et al., 2017 *ApJ*, 834, 2, 149.
- Best W. M. J. et al., 2021 *AJ*, 161, 1, 42.
- Beuzit J. L. et al., 2007 *Protostars and Planets V* (B. Reipurth, D. Jewitt, and K. Keil), p. 717.
- Beuzit J. L. et al., 2019 *A&A*, 631, A155.
- Biller B. A. et al., 2004 *Proc. SPIE*, vol. 5490, pp. 389–397.
- Biller B. A. et al., 2007 *ApJS*, 173, 1, 143.
- Biller B. A. et al., 2013 *ApJ*, 777, 2, 160.
- Biller B. A. et al., 2015 *ApJL*, 813, 2, L23.
- Biller B. A. et al., 2018 *AJ*, 155, 2, 95.
- Biller B. A. et al., 2021 *MNRAS*, 503, 1, 743.
- Blain D. et al., 2021 *A&A*, 646, A15.
- Blunt S. et al., 2017 *AJ*, 153, 5, 229.
- Boccaletti A. et al., 2020 *arXiv e-prints*, arXiv:2003.05714.
- Bohn A. J. et al., 2020a *MNRAS*, 492, 1, 431.
- Bohn A. J. et al., 2020b *ApJL*, 898, 1, L16.
- Bohn A. J. et al., 2021 *A&A*, 648, A73.
- Bonavita M. et al., 2016 *A&A*, 593, A38.
- Bonavita M. et al., 2020 *MNRAS*, 494, 3, 3481.
- Bonavita M. et al., 2022 *MNRAS*, 513, 4, 5588.
- Bonnefoy M. et al., 2013 *A&A*, 555, A107.
- Bonnefoy M. et al., 2014a *A&A*, 562, A127.
- Bonnefoy M. et al., 2014b *A&A*, 567, L9.
- Bonnefoy M. et al., 2016 *A&A*, 587, A58.
- Bonnefoy M. et al., 2018 *A&A*, 618, A63.
- Booth M. et al., 2016 *MNRAS*, 460, 1, L10.
- Borysow A. et al., 1997 *A&A*, 324, 185.
- Bos S. P. et al., 2021 *arXiv e-prints*, arXiv:2106.06286.
- Boss A. P., 1998 *ApJ*, 503, 2, 923.
- Bowler B. P., 2016 *PASP*, 128, 968, 102001.
- Bowler B. P. and Nielsen E. L., 2018 *Occurrence Rates from Direct Imaging Surveys*, p. 155.
- Bowler B. P. et al., 2011 *ApJ*, 743, 2, 148.
- Bowler B. P. et al., 2012a *ApJ*, 753, 2, 142.
- Bowler B. P. et al., 2012b *ApJ*, 756, 1, 69.
- Bowler B. P. et al., 2014 *ApJ*, 784, 1, 65.
- Bowler B. P. et al., 2015 *ApJS*, 216, 1, 7.
- Bowler B. P. et al., 2017 *AJ*, 154, 4, 165.
- Bowler B. P. et al., 2020a *AJ*, 159, 2, 63.
- Bowler B. P. et al., 2020b *ApJL*, 893, 2, L30.
- Bowler B. P. et al., 2021 *ApJL*, 913, 2, L26.
- Brandl B. et al., 2021 *The Messenger*, 182, 22.
- Brandt G. M. et al., 2021a *AJ*, 161, 4, 179.
- Brandt G. M. et al., 2021b *ApJL*, 915, 1, L16.
- Brandt T. D., 2018 *ApJS*, 239, 2, 31.
- Brandt T. D., 2021 *ApJS*, 254, 2, 42.
- Brandt T. D. et al., 2014 *ApJ*, 794, 2, 159.
- Brandt T. D. et al., 2020 *AJ*, 160, 4, 196.
- Brittain S. D. et al., 2014 *ApJ*, 791, 2, 136.
- Bryan M. L. et al., 2020a *ApJ*, 905, 1, 37.
- Bryan M. L. et al., 2020b *AJ*, 159, 4, 181.
- Burningham B. et al., 2017 *MNRAS*, 470, 1, 1177.
- Burningham B. et al., 2021 *MNRAS*, 506, 2, 1944.
- Burrows A. et al., 2001 *Reviews of Modern Physics*, 73, 3, 719.
- Burrows A. et al., 2003 *ApJ*, 596, 1, 587.
- Cantalloube F. et al., 2015 *A&A*, 582, A89.
- Canty J. I. et al., 2013 *MNRAS*, 435, 3, 2650.
- Carson J. et al., 2013 *ApJL*, 763, 2, L32.
- Carter A. L. et al., 2021 *MNRAS*, 501, 2, 1999.
- Carter A. L. et al., 2022 *arXiv e-prints*, arXiv:2208.14990.
- Chabrier G. et al., 2000 *ApJ*, 542, 1, 464.
- Chabrier G. et al., 2007 *Protostars and Planets V* (B. Reipurth, D. Jewitt, and K. Keil), p. 623.
- Charnay B. et al., 2018 *ApJ*, 854, 2, 172.
- Chauvin G. et al., 2003 *A&A*, 404, 157.
- Chauvin G. et al., 2004 *A&A*, 425, L29.
- Chauvin G. et al., 2010 *A&A*, 509, A52.
- Chauvin G. et al., 2012 *A&A*, 542, A41.
- Chauvin G. et al., 2015 *A&A*, 573, A127.
- Chauvin G. et al., 2017 *A&A*, 605, L9.
- Chilcote J. et al., 2017 *AJ*, 153, 4, 182.
- Chilcote J. et al., 2020 *Proc. SPIE*, vol. 11447, p. 114471S.
- Christiaens V. et al., 2019 *ApJL*, 877, 2, L33.
- Close L. M. et al., 2018 *Proc. SPIE*, vol. 10703, p. 107034Y.
- Codona J. L. and Kenworthy M., 2013 *ApJ*, 767, 2, 100.
- Connelley M. S. and Greene T. P., 2010 *AJ*, 140, 5, 1214.
- Crepp J. R. et al., 2012 *ApJ*, 761, 1, 39.
- Crepp J. R. et al., 2016 *ApJ*, 831, 2, 136.
- Crepp J. R. et al., 2018 *ApJ*, 864, 1, 42.
- Crossfield I. J. M., 2014 *A&A*, 566, A130.
- Crossfield I. J. M. et al., 2014 *Nature*, 505, 7485, 654.
- Cugno G. et al., 2021 *arXiv e-prints*, arXiv:2106.03615.
- Cumming A. et al., 2008 *PASP*, 120, 531.
- Currie T. et al., 2011 *ApJ*, 729, 2, 128.
- Currie T. et al., 2012a *ApJL*, 755, 2, L34.
- Currie T. et al., 2012b *ApJL*, 760, 2, L32.
- Currie T. et al., 2013 *ApJ*, 776, 1, 15.
- Currie T. et al., 2014a *ApJ*, 795, 2, 133.
- Currie T. et al., 2014b *ApJL*, 780, 2, L30.
- Currie T. et al., 2015 *ApJL*, 814, 2, L27.
- Currie T. et al., 2017 *Research Notes of the American Astronomical Society*, 1, 1, 40.
- Currie T. et al., 2018 *AJ*, 156, 6, 291.
- Currie T. et al., 2019 *ApJL*, 877, 1, L3.
- Currie T. et al., 2020a *Proc. SPIE*, vol. 11448, p. 114487H.
- Currie T. et al., 2020b *ApJL*, 904, 2, L25.
- Currie T. et al., 2022a *Science, passed external peer review, arXiv e-prints*, arXiv:2212.00034.
- Currie T. et al., 2022b *Nature Astronomy*, 6, 751.
- Cushing M. C. et al., 2006 *ApJ*, 648, 1, 614.
- Cushing M. C. et al., 2008 *ApJ*, 678, 2, 1372.
- Cushing M. C. et al., 2011 *ApJ*, 743, 1, 50.
- Daemgen S. et al., 2017 *A&A*, 608, A71.
- De Rosa R. J. et al., 2020 *AJ*, 159, 1, 1.
- Dekany R. et al., 2013 *ApJ*, 776, 2, 130.
- Delacroix C. et al., 2013 *A&A*, 553, A98.
- Delorme P. et al., 2011 *MNRAS*, 413, 3, 2218.
- Delorme P. et al., 2017a *A&A*, 608, A79.
- Delorme P. et al., 2017b *A&A*, 608, A79.
- Desidera S. et al., 2015 *A&A*, 573, A126.
- Desidera S. et al., 2021 *A&A*, 651, A70.
- Doelman D. S. et al., 2022 *arXiv e-prints*, arXiv:2203.08165.
- Dong R. et al., 2015a *ApJ*, 809, 1, 93.
- Dong R. et al., 2015b *ApJL*, 809, 1, L5.
- D’Orazi V. et al., 2017 *A&A*, 598, A19.

- Douglas E. S. et al., 2019 *The Astronomical Journal*, 157, 1, 36.
- Draper Z. H. et al., 2016 *ApJ*, 826, 2, 147.
- Dressing C. D. and Charbonneau D., 2015 *ApJ*, 807, 1, 45.
- Dumas C., 2020 *Planets 2020, Ground and Space Observatories: a Joint Venture to Planetary Science*, p. 5.
- Dupuy T. J. and Kraus A. L., 2013 *Science*, 341, 6153, 1492.
- Dupuy T. J. and Liu M. C., 2012 *ApJS*, 201, 2, 19.
- Dupuy T. J. et al., 2019 *ApJL*, 871, 1, L4.
- Dupuy T. J. et al., 2022 *MNRAS*, 509, 3, 4411.
- Echeverri D. et al., 2019 *Proc. SPIE*, vol. 11117, p. 111170V.
- Emsenhuber A. et al., 2021 *A&A*, 656, A69.
- Espallat C. et al., 2007 *ApJL*, 670, 2, L135.
- Esposito S. et al., 2011 *Proc. SPIE*, vol. 8149, p. 814902.
- Esposito T. M. et al., 2016 *AJ*, 152, 4, 85.
- Fabrycky D. C. and Murray-Clay R. A., 2010 *ApJ*, 710, 2, 1408.
- Feigelson E. D. et al., 2006 *AJ*, 131, 3, 1730.
- Fernandes R. B. et al., 2019 *ApJ*, 874, 1, 81.
- Fischer D. A. and Valenti J., 2005 *ApJ*, 622, 1102.
- Flasseur O. et al., 2018 *A&A*, 618, A138.
- Fontanive C. et al., 2019 *MNRAS*, 490, 1, 1120.
- Forgan D. and Rice K., 2013 *MNRAS*, 432, 4, 3168.
- Forgan D. et al., 2015 *MNRAS*, 447, 1, 836.
- Forgan D. H. et al., 2018 *MNRAS*, 474, 4, 5036.
- Freytag B. et al., 2010 *A&A*, 513, A19.
- Fukagawa M. et al., 2009 *ApJL*, 696, 1, L1.
- Fulton B. J. et al., 2021 *ApJS*, 255, 1, 14.
- Gagné J. et al., 2017 *ApJL*, 841, 1, L1.
- Gagné J. et al., 2018a *ApJL*, 854, 2, L27.
- Gagné J. et al., 2018b *ApJ*, 860, 1, 43.
- Gagné J. et al., 2021 *ApJL*, 915, 2, L29.
- Galicher R. et al., 2011 *ApJL*, 739, 2, L41.
- Galicher R. et al., 2013 *ApJ*, 769, 1, 42.
- Galicher R. et al., 2016 *A&A*, 594, A63.
- Garufi A. et al., 2016 *A&A*, 588, A8.
- Gaspar A. and Rieke G., 2020 *Proceedings of the National Academy of Science*, 117, 18, 9712.
- Gatkine P. et al., 2019 *Bulletin of the American Astronomical Society*, vol. 51, p. 285.
- Gaudi B. S. et al., 2020 *arXiv e-prints*, arXiv:2001.06683.
- Gauza B. et al., 2015 *ApJ*, 804, 2, 96.
- Gerard B. L. et al., 2018 *AJ*, 156, 3, 106.
- Gerard B. L. et al., 2019 *AJ*, 158, 1, 36.
- Gilles L. et al., 2011 *Second International Conference on Adaptive Optics for Extremely Large Telescopes.*, p. 73.
- Goldman B. et al., 2010 *MNRAS*, 405, 2, 1140.
- Götberg Y. et al., 2016 *A&A*, 592, A147.
- Goździewski K. and Migaszewski C., 2014 *MNRAS*, 440, 4, 3140.
- Goździewski K. and Migaszewski C., 2018 *ApJS*, 238, 1, 6.
- Grandjean A. et al., 2019 *A&A*, 627, L9.
- Grandjean A. et al., 2021 *A&A*, 650, A39.
- GRAVITY Collaboration et al., 2017 *A&A*, 602, A94.
- Gravity Collaboration et al., 2019 *A&A*, 623, L11.
- Gravity Collaboration et al., 2020 *A&A*, 633, A110.
- Greco J. P. and Brandt T. D., 2016 *ApJ*, 833, 2, 134.
- Greco J. P. and Burrows A., 2015 *ApJ*, 808, 2, 172.
- Greenbaum A. Z. et al., 2018 *AJ*, 155, 6, 226.
- Grether D. and Lineweaver C. H., 2006 *ApJ*, 640, 2, 1051.
- Guyon O., 2005 *ApJ*, 629, 1, 592.
- Guyon O. et al., 2006 *The Astrophysical Journal Supplement Series*, 167, 1, 81.
- Guyon O. et al., 2018 *Proc. SPIE*, vol. 107030, p. 107030Z.
- Guyon O. et al., 2020 *Proc. SPIE*, vol. 11448, p. 114481Z.
- Haffert S. Y. et al., 2019 *Nature Astronomy*, 3, 749.
- Hashimoto J. et al., 2012 *ApJL*, 758, 1, L19.
- Hashimoto J. et al., 2020 *AJ*, 159, 5, 222.
- Haywood R. D. et al., 2020 *arXiv e-prints*, arXiv:2005.13386.
- Heinze A. N. et al., 2010 *ApJ*, 714, 2, 1551.
- Hinkley S. et al., 2007 *ApJ*, 654, 1, 633.
- Hinkley S. et al., 2013 *ApJ*, 779, 2, 153.
- Hinkley S. et al., 2022 *PASP*, 134, 1039, 95003.
- Hinkley S. et al., 2022a *arXiv e-prints*, arXiv:2208.04867.
- Hoeijmakers H. J. et al., 2018 *A&A*, 617, A144.
- Houllé M. et al., 2021 *A&A*, 652, A67.
- Huby E. et al., 2017 *A&A*, 600, A46.
- Ida S. et al., 2013 *ApJ*, 775, 1, 42.
- Janson M. et al., 2011 *ApJ*, 736, 2, 89.
- Janson M. et al., 2012 *ApJ*, 745, 1, 4.
- Janson M. et al., 2013 *ApJ*, 773, 1, 73.
- Janson M. et al., 2019 *A&A*, 626, A99.
- Janson M. et al., 2021 *A&A*, 646, A164.
- Jensen-Clem R. et al., 2021 *Proc. SPIE*, vol. 11823, p. 1182309.
- Johansen A. and Lambrechts M., 2017 *Annual Review of Earth and Planetary Sciences*, 45, 1, 359.
- Johnson J. A. et al., 2007 *ApJ*, 670, 833.
- Jones J. et al., 2016 *ApJL*, 822, 1, L3.
- Jovanovic N. et al., 2015 *PASP*, 127, 955, 890.
- Jovanovic N. et al., 2020 *IEEE Journal of Selected Topics in Quantum Electronics*, 26, 4, 2975636.
- Kalas P. et al., 2005 *Nature*, 435, 7045, 1067.
- Kalas P. et al., 2008 *Science*, 322, 5906, 1345.
- Kalas P. et al., 2013 *ApJ*, 775, 1, 56.
- Kammerer J. et al., 2021 *A&A*, 652, A57.
- Karalidi T. et al., 2015 *ApJ*, 814, 1, 65.
- Karalidi T. et al., 2016 *ApJ*, 825, 2, 90.
- Kasdin N. J. et al., 2003 *ApJ*, 582, 2, 1147.
- Kasper M. et al., 2010 *Proc. SPIE*, vol. 7735, p. 77352E.
- Kasper M. et al., 2021 *The Messenger*, 182, 38.
- Kennedy G. M. and Wyatt M. C., 2010 *MNRAS*, 405, 2, 1253.
- Kenworthy M. A. et al., 2007 *ApJ*, 660, 1, 762.
- Kenworthy M. A. et al., 2021 *A&A*, 648, A15.
- Kenyon S. J. and Bromley B. C., 2004 *AJ*, 127, 1, 513.
- Kenyon S. J. and Bromley B. C., 2008 *ApJS*, 179, 2, 451.
- Keppler M. et al., 2018 *A&A*, 617, A44.
- Keppler M. et al., 2019 *A&A*, 625, A118.
- Kervella P. et al., 2019 *A&A*, 623, A72.
- Kiefer F. et al., 2014 *Nature*, 514, 462.
- Kiefer F. et al., 2019 *A&A*, 631, A125.
- Kirkpatrick J. D., 2005 *ARA&A*, 43, 1, 195.
- Kirkpatrick J. D. et al., 2012 *ApJ*, 753, 2, 156.
- Konopacky Q. M. et al., 2013 *Science*, 339, 6126, 1398.
- Konopacky Q. M. et al., 2016 *AJ*, 152, 2, 28.
- Kopparapu R. K. et al., 2018 *ApJ*, 856, 2, 122.
- Kostov V. and Apai D., 2013 *ApJ*, 762, 1, 47.
- Kotani T. et al., 2020 *Proc. SPIE*, vol. 11448, p. 1144878.
- Kratter K. M. et al., 2010 *ApJ*, 710, 2, 1375.
- Kraus A. L. and Ireland M. J., 2012 *ApJ*, 745, 1, 5.
- Kraus A. L. et al., 2008 *ApJ*, 679, 1, 762.
- Krist J. E. et al., 1998 *PASP*, 110, 751, 1046.
- Kuchner M. J. and Traub W. A., 2002 *ApJ*, 570, 2, 900.
- Kuiper G. P., 1951 *Proceedings of the National Academy of Science*, 37, 1, 1.
- Kuzuhara M. et al., 2013 *ApJ*, 774, 1, 11.
- Kuzuhara M. et al., 2022 *ApJL*, 934, 2, L18.
- Lacour S. et al., 2021 *A&A*, 654, L2.

- Lafrenière D. et al., 2007a *ApJ*, 660, 1, 770.
 Lafrenière D. et al., 2007b *ApJ*, 670, 2, 1367.
 Lafrenière D. et al., 2009 *ApJL*, 694, 2, L148.
 Lagrange A.-M. et al., 2000 *Protostars and Planets IV*, p. 639.
 Lagrange A. M. et al., 2009 *A&A*, 493, 2, L21.
 Lagrange A. M. et al., 2010 *Science*, 329, 5987, 57.
 Lagrange A. M. et al., 2016 *A&A*, 586, L8.
 Lagrange A. M. et al., 2019 *Nature Astronomy*, 3, 1135.
 Lagrange A. M. et al., 2020 *A&A*, 642, A18.
 Langellier N. et al., 2021 *AJ*, 161, 6, 287.
 Langlois M. et al., 2021 *A&A*, 651, A71.
 Lannier J. et al., 2016 *A&A*, 596, A83.
 Launhardt R. et al., 2020 *A&A*, 635, A162.
 Lavie B. et al., 2017 *AJ*, 154, 3, 91.
 Lavigne J.-F. et al., 2009 *ApJ*, 704, 2, 1098.
 Lecavelier Des Etangs A. et al., 1997 *A&A*, 328, 311.
 Lew B. W. P. et al., 2016 *ApJL*, 829, 2, L32.
 Line M. R. et al., 2017 *ApJ*, 848, 2, 83.
 Liu M. C. et al., 2013 *ApJL*, 777, 2, L20.
 Lopez-Morales M. et al., 2019 *BAAS*, 51, 3, 162.
 Lovis C. et al., 2017 *A&A*, 599, A16.
 Lowrance P. J. et al., 2005 *AJ*, 130, 4, 1845.
 Lucas P. W. et al., 2001 *MNRAS*, 326, 2, 695.
 Luhman K. L., 2008 *Extreme Solar Systems*, vol. 398 of *Astronomical Society of the Pacific Conference Series* (D. Fischer, F. A. Rasio, S. E. Thorsett, and A. Wolszczan), p. 357.
 Luhman K. L. and Mamajek E. E., 2012 *ApJ*, 758, 1, 31.
 Luhman K. L. et al., 2007 *ApJ*, 654, 1, 570.
 Luna J. L. and Morley C. V., 2021 *ApJ*, 920, 2, 146.
 Lunine J. I. et al., 2008 *arXiv e-prints*, arXiv:0808.2754.
 Macintosh B. et al., 2014 *Proceedings of the National Academy of Science*, 111, 35, 12661.
 Macintosh B. et al., 2015 *Science*, 350, 6256, 64.
 Madhusudhan N., 2018 *Atmospheric Retrieval of Exoplanets*, p. 104.
 Madhusudhan N., 2019 *ARA&A*, 57, 617.
 Madhusudhan N. and Burrows A., 2012 *ApJ*, 747, 1, 25.
 Madhusudhan N. and Seager S., 2009 *ApJ*, 707, 1, 24.
 Madhusudhan N. et al., 2011 *ApJ*, 737, 1, 34.
 Maire A. L. et al., 2015 *A&A*, 579, C2.
 Maire A. L. et al., 2019 *A&A*, 624, A118.
 Males J. R. and Guyon O., 2018 *Journal of Astronomical Telescopes, Instruments, and Systems*, 4, 1, 1.
 Males J. R. et al., 2020 *Proc. SPIE*, vol. 11448, p. 114484L.
 Manjavacas E. et al., 2021 *AJ*, 162, 5, 179.
 Marley M. S. and Robinson T. D., 2015 *ARA&A*, 53, 279.
 Marley M. S. et al., 2007 *ApJ*, 655, 1, 541.
 Marley M. S. et al., 2012 *ApJ*, 754, 2, 135.
 Marley M. S. et al., 2021 *arXiv e-prints*, arXiv:2107.07434.
 Marois C. et al., 2000 *PASP*, 112, 767, 91.
 Marois C. et al., 2006 *ApJ*, 641, 1, 556.
 Marois C. et al., 2008a *ApJ*, 673, 1, 647.
 Marois C. et al., 2008b *Science*, 322, 5906, 1348.
 Marois C. et al., 2010a *Proc. SPIE*, vol. 7736, p. 77361J.
 Marois C. et al., 2010b *Nature*, 468, 7327, 1080.
 Marois C. et al., 2014 *Proc. SPIE*, vol. 9148, p. 91480U.
 Martinache F. et al., 2016 *A&A*, 593, A33.
 Martinod M.-A. et al., 2021 *Nature Communications*, 12, 2465.
 Masciadri E. et al., 2005 *ApJ*, 625, 2, 1004.
 Matthews B. et al., 2014 *ApJ*, 780, 1, 97.
 Mawet D., 2021 *Nature Astronomy*, 5, 723.
 Mawet D. et al., 2010 *ApJ*, 709, 1, 53.
 Mawet D. et al., 2012 *Proc. SPIE*, vol. 8442, p. 844204.
 Mawet D. et al., 2014 *ApJ*, 792, 2, 97.
 McElwain M. W. et al., 2007 *ApJ*, 656, 1, 505.
 McLean I. S. et al., 2007 *ApJ*, 658, 2, 1217.
 Meadows V. S. et al., 2018 *Astrobio*, 18, 6, 630.
 Mendigutía I. et al., 2018 *A&A*, 618, L9.
 Mesa D. et al., 2019 *A&A*, 632, A25.
 Meshkat T. et al., 2015 *MNRAS*, 453, 3, 2378.
 Meshkat T. et al., 2017 *AJ*, 154, 6, 245.
 Metchev S. et al., 2009 *ApJL*, 705, 2, L204.
 Metchev S. A. et al., 2015 *ApJ*, 799, 2, 154.
 Miles B. E. et al., 2018 *ApJ*, 869, 1, 18.
 Miles B. E. et al., 2020 *AJ*, 160, 2, 63.
 Miles B. E. et al., 2022 *arXiv e-prints*, arXiv:2209.00620.
 Milli J. et al., 2017 *A&A*, 597, L2.
 Mizuno H., 1980 *Progress of Theoretical Physics*, 64, 2, 544.
 Mol Lous M. et al., 2018 *A&A*, 615, A145.
 Mollière P. et al., 2020 *A&A*, 640, A131.
 Moór A. et al., 2013 *ApJL*, 775, 2, L51.
 Morbidelli A. et al., 2009 *A&A*, 507, 2, 1041.
 Mordasini C. et al., 2017 *A&A*, 608, A72.
 Morley C. V. et al., 2014 *ApJL*, 789, 1, L14.
 Mulders G. D. et al., 2013 *A&A*, 549, A112.
 Müller A. et al., 2018 *A&A*, 617, L2.
 Naud M.-E. et al., 2014 *ApJ*, 787, 1, 5.
 Nielsen E. L. and Close L. M., 2010 *ApJ*, 717, 2, 878.
 Nielsen E. L. et al., 2013 *ApJ*, 776, 1, 4.
 Nielsen E. L. et al., 2017 *AJ*, 154, 6, 218.
 Nielsen E. L. et al., 2019 *AJ*, 158, 1, 13.
 Nielsen E. L. et al., 2020 *AJ*, 159, 2, 71.
 Norris B. R. M. et al., 2020 *Nature Communications*, 11, 5335.
 Nowak M. et al., 2020 *A&A*, 642, L2.
 Öberg K. I. and Wordsworth R., 2019 *AJ*, 158, 5, 194.
 Öberg K. I. et al., 2011 *ApJL*, 743, 1, L16.
 Offner S. S. R. et al., 2010 *ApJ*, 725, 2, 1485.
 Oreshenko M. et al., 2020 *AJ*, 159, 1, 6.
 Otten G. P. P. L. et al., 2017 *ApJ*, 834, 2, 175.
 Packham C. et al., 2018 *Proc. SPIE*, vol. 10702, p. 10702A0.
 Pairet B. et al., 2019 *MNRAS*, 487, 2, 2262.
 Patel R. I. et al., 2014 *ApJS*, 212, 1, 10.
 Patience J. et al., 2010 *A&A*, 517, A76.
 Pearce T. D. et al., 2015 *MNRAS*, 448, 4, 3679.
 Pecaute M. J. et al., 2012 *ApJ*, 746, 154.
 Perryman M. et al., 2014 *ApJ*, 797, 1, 14.
 Petit dit de la Roche D. J. M. et al., 2018 *A&A*, 616, A146.
 Petrus S. et al., 2020 *A&A*, 633, A124.
 Petrus S. et al., 2021 *A&A*, 648, A59.
 Phillips M. W. et al., 2020 *A&A*, 637, A38.
 Pinte C. et al., 2018 *ApJL*, 860, 1, L13.
 Pinte C. et al., 2019 *Nature Astronomy*, 3, 1109.
 Pollack J. B. et al., 1996 *Icarus*, 124, 1, 62.
 Pueyo L., 2016 *ApJ*, 824, 2, 117.
 Quanz S. P. et al., 2013 *ApJL*, 766, 1, L1.
 Quanz S. P. et al., 2021 *arXiv e-prints*, arXiv:2101.07500.
 Quirrenbach A. et al., 2019 *A&A*, 624, A18.
 Radigan J., 2014 *ApJ*, 797, 2, 120.
 Radigan J. et al., 2014 *ApJ*, 793, 2, 75.
 Rajan A. et al., 2017 *AJ*, 154, 1, 10.
 Rameau J. et al., 2013a *A&A*, 553, A60.
 Rameau J. et al., 2013b *ApJL*, 779, 2, L26.
 Rameau J. et al., 2016 *Astrophys. J.*, 822, 2, L29.
 Rameau J. et al., 2017 *AJ*, 153, 6, 244.

- Rameau J. et al., 2021 *A&A*, 649, A143.
- Read M. J. et al., 2018 *MNRAS*, 475, 4, 4953.
- Reggiani M. et al., 2016 *A&A*, 586, A147.
- Reipurth B., 2008a *Handbook of Star Forming Regions, Volume I: The Northern Sky*, vol. 4.
- Reipurth B., 2008b *Handbook of Star Forming Regions, Volume II: The Southern Sky*, vol. 5.
- Rice E. L. et al., 2010 *ApJS*, 186, 1, 63.
- Rich E. A. et al., 2019 *ApJ*, 875, 1, 38.
- Riviere-Marichalar P. et al., 2014 *A&A*, 565, A68.
- Ruffio J.-B. et al., 2017 *ApJ*, 842, 1, 14.
- Ruffio J.-B. et al., 2019 *AJ*, 158, 5, 200.
- Ruffio J.-B. et al., 2021 *AJ*, 162, 6, 290.
- Sadakane K. and Nishida M., 1986 *PASP*, 98, 685.
- Sahlmann J. et al., 2011 *The Astrophysics of Planetary Systems: Formation, Structure, and Dynamical Evolution*, vol. 276 (A. Sozzetti, M. G. Lattanzi, and A. P. Boss), pp. 117–120.
- Sallum S. et al., 2015 *Nature*, 527, 7578, 342.
- Samland M. et al., 2017 *A&A*, 603, A57.
- Schlieder J. E. et al., 2012 *AJ*, 143, 4, 80.
- Schmid H. M. et al., 2018 *A&A*, 619, A9.
- Schmidt T. O. B. et al., 2008 *A&A*, 491, 1, 311.
- Schneider A. et al., 2012 *ApJ*, 754, 1, 39.
- Schwarz H. et al., 2016 *A&A*, 593, A74.
- Schwieterman E. W. et al., 2018 *Astrobiology*, 18, 6, 663.
- Seifahrt A. et al., 2007 *A&A*, 463, 1, 309.
- Shaklan S. B. and Green J. J., 2006 *ApOpt*, 45, 21, 5143.
- Shi F. et al., 2017 *Proc. SPIE*, vol. 10400, pp. 74 – 90, SPIE.
- Shields A. L. et al., 2019 *ApJL*, 884, 1, L2.
- Shkolnik E. L. et al., 2012 *ApJ*, 758, 1, 56.
- Showman A. P. and Kaspi Y., 2013 *ApJ*, 776, 2, 85.
- Singh G. et al., 2015 *PASP*, 127, 955, 857.
- Sissa E. et al., 2018 *A&A*, 619, A160.
- Sivaramakrishnan A. et al., 2005 *ApJ*, 634, 2, 1416.
- Skemer A. J. et al., 2012 *ApJ*, 753, 1, 14.
- Skemer A. J. et al., 2014a *ApJ*, 792, 1, 17.
- Skemer A. J. et al., 2014b *Proc. SPIE*, vol. 9148, p. 91480L.
- Smith B. A. and Terrile R. J., 1984 *Science*, 226, 4681, 1421.
- Snellen I. A. G. and Brown A. G. A., 2018 *Nature Astronomy*, 2, 883.
- Snellen I. A. G. et al., 2014 *Nature*, 509, 7498, 63.
- Soderblom D. R. et al., 2014 *Protostars and Planets VI* (H. Beuther, R. S. Klessen, C. P. Dullemond, and T. Henning), p. 219.
- Song I. et al., 2003 *ApJ*, 599, 1, 342.
- Song I. et al., 2012 *AJ*, 144, 1, 8.
- Sorahana S. and Yamamura I., 2012 *ApJ*, 760, 2, 151.
- Soummer R. et al., 2007 *ApJ*, 669, 1, 642.
- Soummer R. et al., 2011 *ApJ*, 741, 1, 55.
- Soummer R. et al., 2012 *ApJL*, 755, L28.
- Sparks W. B. and Ford H. C., 2002 *ApJ*, 578, 1, 543.
- Spergel D. et al., 2013 *arXiv e-prints*, arXiv:1305.5422.
- Spiegel D. S. and Burrows A., 2012 *ApJ*, 745, 2, 174.
- Spiegel D. S. et al., 2011 *ApJ*, 727, 1, 57.
- Stolker T. et al., 2020 *A&A*, 644, A13.
- Stone J. M. et al., 2016 *ApJ*, 829, 1, 39.
- Stone J. M. et al., 2018 *AJ*, 156, 6, 286.
- Stone J. M. et al., 2020 *AJ*, 160, 6, 262.
- Su K. Y. L. et al., 2009 *ApJ*, 705, 314.
- Su K. Y. L. et al., 2015 *ApJ*, 799, 2, 146.
- Suarez G. et al., 2022 *MNRAS*, 513, 4, 5701.
- Sudol J. J. and Haghhighipour N., 2012 *ApJ*, 755, 1, 38.
- Sumi T. et al., 2011 *Nature*, 473, 7347, 349.
- Suzuki D. et al., 2016 *ApJ*, 833, 2, 145.
- Tamura M., 2016 *Proceedings of the Japan Academy, Series B*, 92, 45.
- Tan X. and Showman A. P., 2017 *ApJ*, 835, 2, 186.
- Tan X. and Showman A. P., 2019 *ApJ*, 874, 2, 111.
- Tan X. and Showman A. P., 2021a *MNRAS*, 502, 1, 678.
- Tan X. and Showman A. P., 2021b *MNRAS*, 502, 2, 2198.
- Tang Y.-W. et al., 2017 *ApJ*, 840, 1, 32.
- Tannock M. E. et al., 2021 *AJ*, 161, 5, 224.
- Teague R. et al., 2018 *ApJL*, 860, 1, L12.
- Thalmann C. et al., 2014 *A&A*, 572, A91.
- Thanathibodee T. et al., 2019 *ApJ*, 885, 1, 94.
- Thatte N. et al., 2007 *MNRAS*, 378, 4, 1229.
- The LUVOIR Team, 2019 *arXiv e-prints*, arXiv:1912.06219.
- Thompson W. and Marois C., 2021 *AJ*, 161, 5, 236.
- Todorov K. et al., 2010 *ApJL*, 714, 1, L84.
- Traub W. A. and Oppenheimer B. R., 2010 *Direct Imaging of Exoplanets*, pp. 111–156.
- Tremblin P. et al., 2016 *ApJL*, 817, 2, L19.
- Tremblin P. et al., 2017 *ApJ*, 850, 1, 46.
- Tremblin P. et al., 2019 *ApJ*, 876, 2, 144.
- Tremblin P. et al., 2020 *A&A*, 643, A23.
- Tyson R. K., 1998 *Principles of adaptive optics*.
- Uyama T. et al., 2017 *AJ*, 154, 3, 90.
- van Sluijs L. et al., 2019 *A&A*, 626, A97.
- Vigan A. et al., 2012 *A&A*, 544, A9.
- Vigan A. et al., 2017 *A&A*, 603, A3.
- Vigan A. et al., 2019 *A&A*, 629, A11.
- Vigan A. et al., 2021 *A&A*, 651, A72.
- Vogt S. S. et al., 1987 *ApJ*, 321, 496.
- Vorobyov E. I. et al., 2013 *MNRAS*, 433, 4, 3256.
- Vos J. M. et al., 2018 *MNRAS*, 474, 1, 1041.
- Vos J. M. et al., 2019 *MNRAS*, 483, 1, 480.
- Wagner K. et al., 2018 *ApJ*, 854, 2, 130.
- Wahhaj Z. et al., 2013 *ApJ*, 773, 2, 179.
- Wahhaj Z. et al., 2021 *A&A*, 648, A26.
- Wang J. et al., 2018 *AJ*, 156, 6, 272.
- Wang J. et al., 2020 *AJ*, 160, 3, 150.
- Wang J. J. et al., 2016 *AJ*, 152, 4, 97.
- Wang J. J. et al., 2018 *AJ*, 156, 5, 192.
- Wang J. J. et al., 2021 *AJ*, 162, 4, 148.
- Ward-Duong K. et al., 2021 *AJ*, 161, 1, 5.
- Wilcomb K. K. et al., 2020 *AJ*, 160, 5, 207.
- Wilson P. A. et al., 2014 *A&A*, 566, A111.
- Xuan J. W. et al., 2020 *AJ*, 159, 3, 97.
- Xuan W. J. et al., 2018 *AJ*, 156, 4, 156.
- Yang H. et al., 2016 *ApJ*, 826, 1, 8.
- Yelverton B. et al., 2020 *MNRAS*, 495, 2, 1943.
- Zapatero Osorio M. R. et al., 2006 *ApJ*, 647, 2, 1405.
- Zhang X. and Showman A. P., 2014 *ApJL*, 788, 1, L6.
- Zhang Y. et al., 2021a *Nature*, 595, 7867, 370.
- Zhang Z. et al., 2021b *ApJ*, 911, 1, 7.
- Zhang Z. et al., 2021c *ApJL*, 916, 2, L11.
- Zhang Z. et al., 2021d *ApJ*, 916, 1, 53.
- Zhou Y. et al., 2020 *AJ*, 160, 2, 77.
- Zhou Y. et al., 2022 *arXiv e-prints*, arXiv:2210.02464.
- Zhu Z., 2015 *ApJ*, 799, 1, 16.
- Zieba S. et al., 2019 *A&A*, 625, L13.
- Zuckerman B. and Song I., 2004 *ARA&A*, 42, 1, 685.
- Zuckerman B. et al., 2011 *ApJ*, 732, 2, 61.
- Zurlo A. et al., 2016 *A&A*, 587, A57.

Zurlo A. et al., 2022 *A&A*, 666, A133.